Fabrication of TiB_2–Reinforced Fe Base Composites by Spark Sintering, and their Improvement in Thermal Conductivity and Hardness

（TiB_2 強化鉄系複合材料の放電焼結による作製とそれらの熱伝導率及び硬度向上）

KE YUJIAO

March 2020

CONTENTS

Chapter1 Background and objectives

List of figures

List of tables

Chapter 1

Background and objectives

1.1 Introduction

"Environmentally friendly" or "eco-friendly" has been an issue of urgent concern for decades. A vast amount of greenhouse gases has been emitted to the atmosphere since the beginning of the Industrial Revolution (around 1750), mainly through the combustion of fossil fuels. It is reported that human activities have contributed to a 45% increase in the atmospheric concentration of carbon dioxide (CO_2) when compared that in the year of 1750 with early 2017[1]. Consequently, a series of environmental problems have occurred, such as global warming, sea level rise, climate change, etc. This further lead to some potentially harmful effects on ecosystems, biodiversity and human livelihoods. In 2019, the United nations (UN) issued "UN Environment's sixth Global Environment Outlook" which calls on decision makers to take immediate action to address pressing environmental issues to achieve the sustainable development goals as well as other internationally agreed environment goals, such as the Paris Agreement. Therefore, in response to that call, environmentally friendly measures, such as energy conservation, emission reduction and low carbon, have been the consensus to deal with the increasingly deteriorating environmental problems in all countries/regions.

The transportation sector includes the movement of people and goods by cars, trucks, trains, ships, airplanes, and other vehicles. Majority of greenhouse gas emissions from transportation are CO_2 emissions resulting from the combustion of petroleum-based products, like gasoline, in internal combustion engines. The largest sources of transportation-related greenhouse gas emissions include passenger cars and light-duty trucks, including sport utility vehicles, pickup trucks, and minivans. These sources account for over half of the emissions from the transportation sector. The remaining greenhouse gas emissions from the transportation sector come from other modes of transportation, including freight trucks, commercial aircraft, ships, boats, and trains, as well as pipelines and lubricants. In 2017, greenhouse gas emissions from transportation accounted for about 29 % of total U.S. greenhouse gas emissions, making it the largest contributor of U.S. greenhouse gas emissions as shown in Fig.1.1(a)[2]. It is 17% of total Japan greenhouse gas emissions issued in 2014, among which automobiles take up approximately 88% as illustrated in Fig. 1.2(b)[3]. Reduction of greenhouse gas emissions in automobiles can be of importance on the total greenhouse gas emissions.

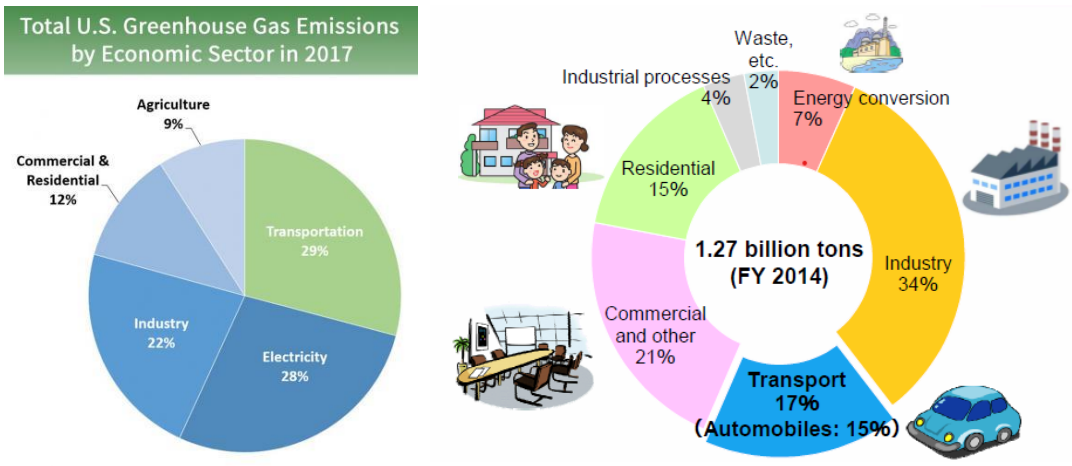

Fig. 1.1 Greenhouse gas emissions in: (a) U.S. in 2017[2)] and (b) Japan in 2014[3)].

In an effort to reduce CO_2 emissions from passenger cars, Hitachi group[4)] proposed three primary approaches: development of high-efficiency engines, "hybridization" and electrification of drive trains, and application of intelligent transport systems. Besides, in automobiles industry, other approaches are also mentioned, such as enhancing efficiency of the drive systems, and optimizing fuel economy. Electric vehicles (EVs) powered by electricity are considered a promising alternative to internal combustion engine vehicles under the purpose of energy saving and emission reduction, since EVs emit no tailpipe pollutants compared with conventional vehicles.[5)] It is said that 10% reduction in vehicle weight contribute to 6% to 8% decrease in fuel consumption, and every 100 kg weight reduction in vehicles will bring about 5g/km decrease in CO_2 emissions.[6)] Therefore, lightweight in automobiles shows great potential in automotive applications. Up to date, various of materials have been proposed to achieve the lightweight in vehicles, the predominant are aluminum alloys[7-10)], magnesium alloys[11-13)], carbon fiber composites[14,15)] and advanced high strength steels (AHSS)[16-23)]. Compared with above mentioned techniques, weight reduction is currently the most accessible and feasible way to be implemented in a short period.

1. 2 AHSS application in transportation sector

1.2.1 Advantage of AHSS application

However, challenge remains with regard to how to balance the weight reduction and passengers' safety. Because weight reduction is equivalent to strength reduction in a conventional perspective. Applications of aluminum alloys and magnesium alloys in automobiles can dramatically contribute to weight reduction in vehicles, though, their strength is not sufficient when applied to structural parts. Consequently, those light alloys are not incompetent options for structural parts taking consideration of passengers' safety. Carbon fiber reinforced composites with high strength may be a possible selection if the production cost is reduced. Structural parts of vehicles mainly refer to the constituent parts of passenger compartment which should resist any deformation or intrusions that would compromise the integrity of the structure and impinge on the space around the passengers. So, materials are selected to minimize weight, while meeting key criteria including crash performance, stiffness, and formability. AHSS seems to be the only option for structural parts materials as AHSS is characterized by high strength and high stiffness. In fact, many automotive ancillary parts, body structure, suspension and chassis components, as well as wheels, are made of AHSS. Saab Automobile AB, a manufacturer of automobiles in Sweden, was the first automaker to apply hot stamped components in commercial vehicles. Since then the world witnessed a rapid expansion of hot stamped components application in automobiles field. Accordingly, the percentage of hot stamped components body-in-white was 7% for Volvo XC90 launched 2003 and increased to 17% in 2006, 17% in for Volkswagen Passat launched in 2006, 12% for BMW5 launched in 2009, and 12% for Volkswagen Golf VII launched in 2012. And it was raised to 40% for Volvo XC90 launched in 2014. By the year of 2014, the number of hot-stamped parts dramatically increased to 250 million pieces[23)].

1.2.2 Approaches of producing AHSS

1.2.2.1 Cold stamping

Generally, there are two approaches to produce AHSS, cold stamping (CS) and hot stamping (HS). CS is faster than hot stamping because it does not need furnace heating process which preheats steel blanks to designed temperature before stamping. However, CS technique is impeded to a wider usage due to its drawbacks, such as large springback, high stamping load, low formability, short tool life and severe wear such as galling and seizure. Especially large springback and low tool life are difficult to be solved even though the cold stamping ability can reach as high as 1.5 GPa[23)] Hence, developing processes for producing high strength steel with bare springback are desirable for automobile field.

1.2.2.2 Hot stamping

HS is a newly developed technique to produce ultra-high strength steels for the application in automobile parts without any spring back. The ultra-high strength steel parts pressed by HS can have a tensile strength of as high as 1.5 GPa. Quenchable steel sheets are austenitized by heating to approximately 1203-1223 K and transformed into martensite by holding at the bottom dead center of a press for die quenching. The formed parts are hardened to a tensile strength of 1.5 GPa. Quenchability and toughness are required for the steel sheets and formed parts, respectively. In addition, treatments for preventing or removing oxidation of the heated steel sheets to 1173 K are essential for subsequent welding and painting operations. Therefore, HS owns several advantages over CS, such as

- Complex geometries
- Improved formability
- Low forming forces
- Smaller springback
- Improved hardness
- Less tool wears
- Light in weight
- High in strength[19)]

However, the current HS technique still has major disadvantages. Firstly, the high production cost is inevitably the quenchable steels must be preheated to austenite temperature leading to low energy efficiency. Secondly, the productivity is low because it is two or three shots per minute in HS process[24]. Thirdly, the oxidation of preheated steels is involved. But generally, coatings for protecting the oxidation of preheated sheets are adopted, which further increase the production cost. Finally, tool failure (high temperature wear) and lubrication between dies and steels at elevated temperature are also problematic.

1.3 Introduction of HS materials

The most commonly used materials for HS process are SKD61 which is standardized by Japanese Industrial Standards, and also called H13 in the United states, 1.2344/X40CrMoV5-1 in German, STD61 in South Korea and BH13 in Britain. The compositions of SKD61 is listed in Table 1.1. It is a hot work steel tools (HWSTs) which has been used in hot and cold work tooling applications and characterized by the following properties:

- Good resistance to abrasion at both low and high temperatures
- High level of toughness and ductility
- Uniform and high level of machinability and polishability
- Good high-temperature strength and resistance to thermal fatigue
- Excellent through-hardening properties
- Very limited distortion during hardening

Besides, SKD61 steels are strengthened by the molybdenum and vanadium by forming carbides precipitations. High temperature resistance is attributed to the high chromium content in compositions. Due to the combination of excellent properties listed above, SKD61 is used not only in HS die tools, but also widely used in other hot work applications, such as extrusion tools, forging dies tools, pressure casting tools and hot shear knives tools.

Table 1.1 Chemical compositions of SKD61 (wt%)[25].

C	Si	Mn	P	S	Cr	Mo	V	Fe
0.398	0.968	0.406	0.018	0.008	5.145	1.252	0.920	Bal.

1.3.1 Heat treatments of SKD61

Different heat treatments must be applied to SKD61 to acquire different mechanical properties for different applications. In this study, the SKD61 is used for HS application. A serial of heat treatments, including annealing, stress relieving, preheat prior to hardening, hardening, quenching and tempering, are applied to SKD61 and listed in Fig. 1.2. On some special occasions, the wear resistance is required. Therefore, surface

hardening process, such as nitriding, is generally adopted to form a hard surface layer on SKD61. Although excellent properties of SKD61 are granted after a serial of complex heat treatments, it is not cost-effective and environment-friendly in term of developing sustainable society. Because a vast amount of capital and energy will be consumed during those complex heat treatments process. Therefore, a more cost-effective and energy-saving material for HS dies usage is essential in the future to achieve the sustainable society.

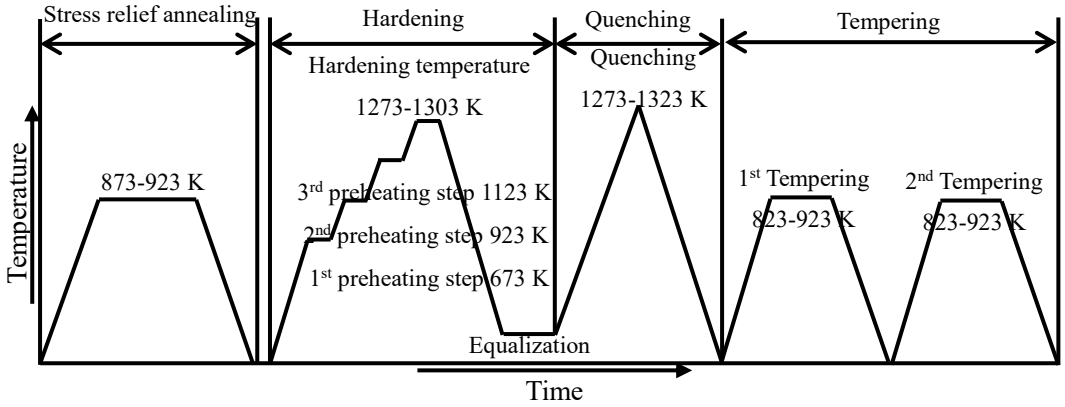

Fig. 1.2 Sketch of heat treatments of SKD61.

1.3.2 TC of HS tools

In addition, the productivity of HS process is not high, which is about two or three shots per minute[23]. That is, the cycle time for each shot takes approximate 20-30 s. The temperature variation of workpiece and time before and after stamping is shown in Fig. 1.3 The low productivity is partially due to the low TC of HS tools, since heat is transferred from workpieces to HS tools and transported to the cooling system, which takes time especially from an austenitic temperature to almost room temperature. And hence, the thermal properties of HS tools, to some extent, determine the cooling rate of workpieces, the heat transfer mechanism and temperature distribution[26]. The TC at room temperature of SKD61 heat treated as mentioned above is about 25 W/(m·K). Therefore, as expected, the production efficiency can be further improved if the TC of HS tools is raised.

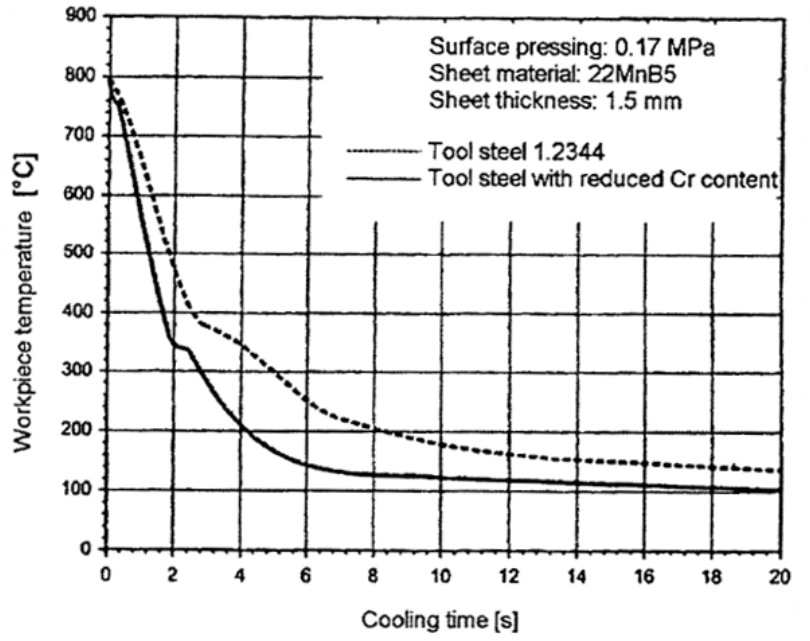

Fig. 1.3 Temperature variation of workpieces before and after HS.[36)]

1.3.3 Wear resistance of HS tools

HS tool is one type of hot work tools which undergo severe thermal shock and mechanical load during high temperature processing. Therefore, they are inevitably to suffer the extremely aggressive wear situations due to the abrasion and adhesion at high temperature service, which contributes to severe tool surface damages. In the work of J. Kohopää et al.[27)] damages occur mainly due to erosion, plastic deformation, thermal fatigue or mechanical fatigue. The tool cavity is the place where the damages are most easily to occur because, in the case of hot forming or HS, repeated large scale sliding friction occur between workpieces and tool surface when subject to applied pressure as well as relative speed. Consequently, the wear situations become a limiting factor in the service life of hot work tools, and yet, increase the maintenance cost of hot work tools.

The wear resistance is one of the most important factors which affect the service live of hot work tools. Generally, improving the hardness of materials of hot work tools is an effective way to enhance the wear resistance. Surface hardening, such as carburizing[28)], nitriding[29)], boriding and PVD coating of hard ceramics[30)], has been widely used to reinforce the surface wear resistance of materials. In addition to that,

particulates reinforced metal matrix composites are also reported to be potential in usage of wear resistance.[31,32] This is the highlight of this study which will be discussed in detail in the following section.

1.3.4 Thermal fatigue of HS tools

Thermal fatigue is the gradual deterioration process by alternate heating and cooling during which thermal stresses are produced by cyclic material expansion and contraction when temperature changes under geometric constraints. Macroscopic cracks or final fracture of materials result from cyclic thermal stresses and strains due to temperature changes, spatial temperature gradients, and high temperatures under constrained thermal deformation. Thermal fatigue may occur without mechanical loads. Thermal fatigue damages are often present as a network of fine cracks on surface layer of tools.[33] Therefore, thermal fatigue is a crucial life-limiting failure mechanism in hot work tools. In order to increase the resistance to thermal fatigue cracking, an initial tensile residual stress applied to the tool material surface may also be able to delay fatigue crack propagation.[33] Besides, it is considered low thermal expansion and high TC are essential properties for hot work tools materials.[34]. Moreover, I.V. Angles et al.[35] also reported that doubling TC can bring an order of magnitude increase in thermal fatigue resistance for many applications.

On the purpose of improving the production efficiency and reducing the maintenance cost of hot work tools, increasing the TC and hardness of hot work tools is of great importance.

1.4 Development of new materials for HS application

1.4.1 Newly developed alloy

I.V. Angles et al.[36] developed a series of new alloys (designated as Rovalma alloy) for application of hot work tool steels. As shown in Fig. 1.4. 1, 2 and 3 represent large carbides, small carbides and matrix respectively. The basic design idea of these alloys based on that ferritic matrix is reinforced by in-situ formation of carbides by adding strong carbide-forming elements, such as Mo, W, Ti, Zr, Hf, Nb and Ta, in a fraction of up to certain amount. In addition, the amount of some other elements has to be added in order to meet other properties. Chromium provides the alloys with good oxidation resistance. Molybdenum increases the TC and reduces the thermal expansion of the alloys. Co guarantees high-temperature resistance of the alloys. Vanadium establishes fine carbide networks of the alloys. Si offers the toughness of the alloys. However, every element addition has to be tailored to an appropriate amount in case of any disadvantageous effects. For examples, over added Chromium or Vanadium will decrease the TC of the alloys. Therefore, not only does very positive aspect have to be taken into consideration, but also negative effects have to be eliminated or reduced to the minimum. As a result, I.V. Angles et al.[36] developed various alloys with TC as high as 72 W/m·K and Rockwell hardness ranging from 40 to 52 HRC. This is a great increase in TC compared with the most commonly used hot work tools steel (SKD61), while the hardness remains the same level with SKD61. The TC and Rockwell hardness of SKD61 heat treated in this study and Rovalma alloy are listed in table. However, it is difficult to further increase the hardness of the alloys without decreasing the thermal conductivity. The commonly used methods of improving the strength of alloys, such as mechanical rolling, thermomechanical rolling, martensite reinforcement and duplex phase reinforcement, will dramatically change the microstructure of alloys which, in turn, has a tremendous negative effect on thermal conductivity. In the case of practice usage, the improved TC can promote the cycle time, but it is still hypodynamic to realize the cost-down due to the unimproved hardness. The development of Rovalma alloys inspired and highlighted us with regard to how to develop a new alloy for hot work tool steels. However, challenge remains concerning how invent a new material

with both high TC and hardness for the usage of hot work tool steels.

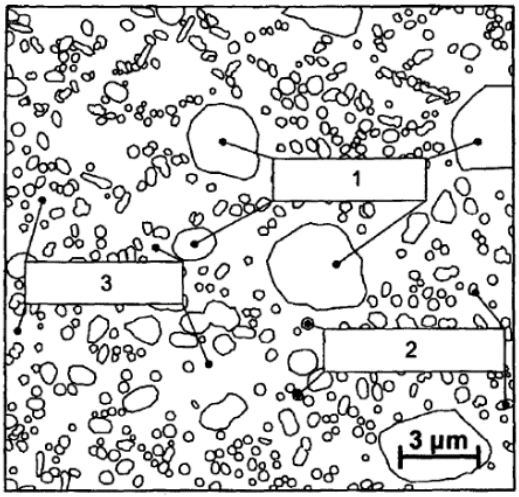

Fig. 1.4 Schematic microstructure illustration of designed alloys, and 1, 2 and 3 represent large carbides, small carbides and matrix respectively.[36)]

Table 1.2 TC and Rockwell hardness on C scale of SKD61and Rovalma alloys[36)].

Alloys	Hardness (H_RC)	TC (W/(m·K))
SKD61	50	24
Rovalma alloy	40-52	72

1.4.2 Particulates reinforced metal matrix composites

1.4.2.1 Selection of metal matrix

Fe and steels have been the most widely used and dominating materials on this planet for thousands of years, with their coverage for almost every aspect in human society. Such as infrastructure of railways, airports, roads and buildings, appliances, steel skeleton of stadiums and skyscrapers, transportations and even small components. The steel industry has been evaluated as an indicator of economic progress because of the crucial role played by steels in overall economic development. In addition, as to recycling, iron and steels are one of the most-recycled materials in the world, with a recycling rate of over 60% globally[37)]. Moreover, technically speaking, the systems of

Fe, Fe based alloys and steels have been well-developed in terms of produce, heat treatments and mechanical or thermo/mechanical processes. Different heat treatments on steels and alloys can bring about different properties. Therefore, they are not only the most widely used materials but also the most functional materials. Steels have been researched to the uttermost, seldom breakthrough can be made in recent years. But a lot of new challenges emerged, as the higher demands were put forward in new fields, in particular, wear resistance and light weight, where more excellent properties are required.

1.4.2.2 Selection of TiB_2 particulates

The selection of ceramics reinforcements is mainly based on four aspects. (a) high hardness, (b) high thermal conductivity, (c) good compatibility with matrix, and (d) cost effective. TC and hardness of matrix and ceramics of matrix and candidate ceramics are shown in Table 1.3.

Transition metal carbides are reinforcements for improving the strength of steels, however, they are high in hardness but low in thermal conductivity, which means large amount of those carbides cannot be added into matrix if high TC is expected. SiC, AlN and TiB_2 seem to be the promising candidates to reinforce Fe matrix without decreasing the thermal conductivity. Nevertheless, SiC is not chemically stable in Fe at high temperatures. J. Pelleg[38] fabricated Fe–SiC metal matrix composite HIPed at 1173 K at a pressure of 150 MPa. when the SiC content was 3% by volume. C atoms derived from the SiC dissolved into Fe inducing changes in the matrix when the MMC is exposed to high temperatures. Machida[39] also synthesized Fe-SiC composites at different temperatures holding different times. SiC reacted with Fe and formed Fe_3Si, FeSi and $FeSi_2$ at 1373 K. Results show that SiC is not chemically stable in Fe matrix at high temperature. Therefore, surface modification on SiC is a feasible method to prevent SiC from decomposing in metals[40,41]. Fe-AlN composites are seldom reported in literatures. But in Machida's work[39], Fe-30vol.%AlN composites were fabricated at 1473 K by SPS with the hardness and TC of 193 HV and 57 W/(m·K), respectively. And hence, more improvements should be adopted to further improve the properties of Fe-30vol.%AlN composites, especially in hardness.

TiB_2 ceramics has drawn enormous interest in recent years due to its superior properties including high hardness, high Young's modulus, good wear resistance, corrosion resistance, electrical/thermal conductivity and high temperature stability[42,43] The basic properties of TiB_2 are displayed in Table 1.4. Therefore, it shows great potential ， for applications such as cutting tools, wear resistant parts, armor materials and high-temperature structural components in heat exchangers and engines.

Table 1.3 TC and hardness of matrix and ceramics.[39]

	TC (W/(m·K))	Hardness (HV)
α-Fe	79	70-100
Martensite	32	500-850
Cementite	8	1340
Cr_2C_3	19	2280-2410
MoC	32	2250
WC	29	2740
TiC	17	3200
SiC	270	2200
TiB_2	100	3300
AlN	285	1050

Table 1.4 Properties of TiB_2.[42,50)]

Lattice parameter (nm)	a = 0.3028; c = 0.3228
Density (g/cm^3)	4.52
Melting point (K)	3498
Hardness (HV)	25-35
Young modulus (GPa)	560
Friction coefficient	0.9
Wear coefficient	1.7×10^{-3}
TC (W/(m·K))	60-120
Linear thermal expansion coefficient (10^{-6} K^{-1})	$5.107 + 1.997\times10^{-3}T$

The Ti–B equilibrium phase diagram is shown in Fig. 1.5. There are three equilibrium boride phases of TiB, Ti_3B_4, TiB_2 confirmed by K.E. Spear et al.[44)] TiB_2 exhibits a very narrow composition variation where at. % of B ranges from 65.5-67% in Fenish's work[45)], 65.2-66.3% in Windisch's work[46)] and 65.5–67.6t% in Thebault work[47)], respectively. The crystal structure of TiB_2 is a hexagonal AlB_2-type structure with a P6/mmm space group. The boron atoms fill the trigonal prisms that are formed by the titanium atoms, as shown in Fig. 1.6. Each boron atom has three boron neighbors in a trigonal planar arrangement, forming a two-dimensional honeycomb network with a distance of 0.175 nm.[48)]

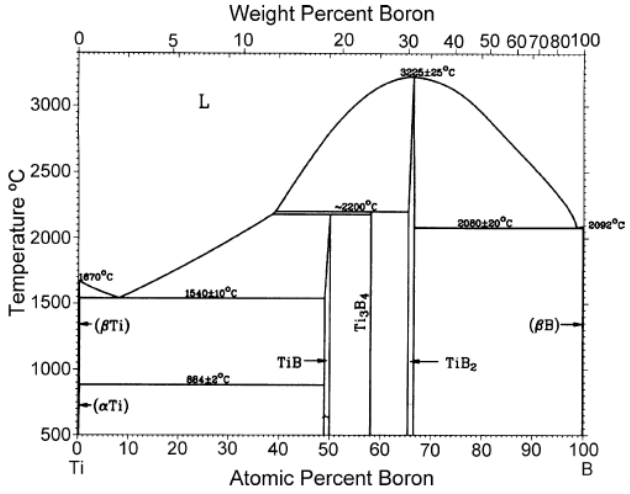

Fig. 1.5 Binary Ti–B phase diagram.[49)]

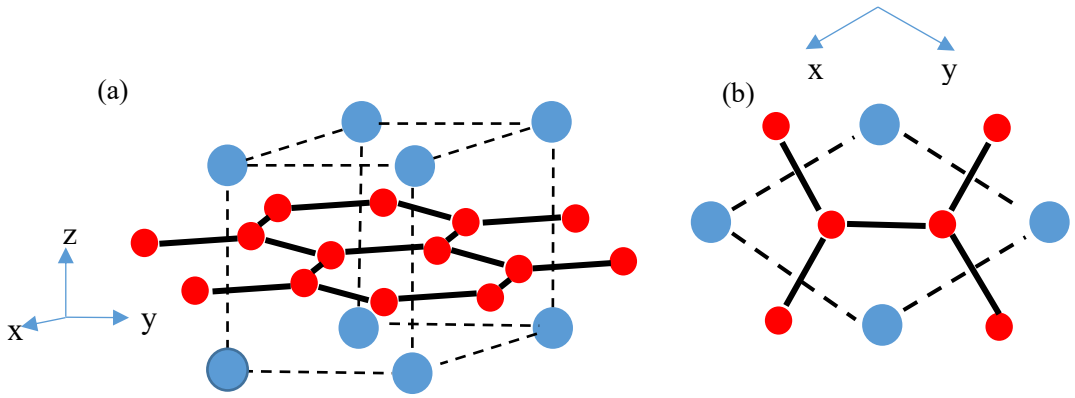

Fig. 1.6 (a) AlB_2 type structure of TiB_2 and (b) A projection along the hexagonal axis.

1.4.3 Introduction of Fe-TiB_2 composites

The charming physical and mechanical properties stemmed from ceramics reinforced metal matrix composites (MMCs) have drawn great attention for decades for the potential of a wide range of applications, such as aerospace, automotive, wear parts. The combination of the toughness and ductility from metals and strength, stiffness as well as hardness from ceramics grants MMCs greater strength in shear and compression and higher service temperature capabilities. As one of the MMCs, TiB_2 reinforced Fe matrix composites are of considerate interest to many researchers in recent years. Some characteristics of Fe-TiB_2 composites were investigated as listed below.

1.4.3.1 Wettability between Fe and TiB_2

The interface formed between the matrix and the ceramics reinforcements is of tremendous importance since it determines the strength, load transfer, and crack resistance of MMCs during deformation. Therefore, it has been widely recognized that in the effort to enhance the interfacial bonding, it is essential to promote the wetting, control chemical interactions between the matrix and the ceramics reinforcement. As for Fe-TiB_2 systems, the wettability between Fe and TiB_2 were conducted by some studies. The wettability between molten metal and ceramics can be acquired by measuring the contact angle θ which is defined by Young's equation 1.1.

$$\gamma_{sg} = \gamma_{lg} \cdot \cos\theta + \gamma_{sl} \quad (1.1)$$

Where γ_{sg}, γ_{lg} and γ_{sl} are the interracial energies between solid and gas, liquid and

gas, and solid and liquid phases, respectively.

In1970's, an extensive work was conducted with regard to wetting of metals to of Group IV–VI metal diborides XB_2 [51,52], and X refers to Ti, Zr, Hf. The results show that transition metals (Fe, Co, Ni) exhibit better wetting behavior than non-transition metals as shown in Table 1.5. The angles given in Table refer to the contact angle after melting, however, the contact angles decrease after a few seconds, reaching lower values (for TiB_2: $\theta = 42°$ for Fe, $\theta = 26°$ for Ni and $\theta = 18°$ for Co in argon atmosphere) due to interfacial reactions/dissolution and then to the change in composition of the solid–liquid interface. Therefore, Fe can well wet TiB_2, and the wettability can be further improved when small amount of Ni or Cr are added into Fe.

Table 1.5 Contact angles of different metals on TiB_2, ZrB_2 and HfB_2.[51,52]

Borides	Metals	Contact angle	Temp. ^oC	Medium
TiB_2	Ag	126	1100	He
TiB_2	Cu	135–132	1100–1300	Ar
TiB_2	Ga	115	800	Vacuum
TiB_2	Sn	114	250	Ar
TiB_2	Ni	0	1500	Vacuum
TiB_2	Fe	62	1550	Vacuum
TiB_2	Co	20	1500-1600	Vacuum
ZrB_2	Ag	114	1100	He
ZrB_2	Ga	127	800	Vacuum
ZrB_2	Al	106–60	900–1250	Vacuum
ZrB_2	Ge	102	1000	Ar
ZrB_2	Fe	55	1550	Vacuum
ZrB_2	Ni	65	1480–1600	Vacuum
ZrB_2	Co	39	1500	Vacuum
HfB_2	In	114	300–500	Vacuum
HfB_2	Ge	140	1000–1100	Vacuum
HfB_2	Al	134–60	900–1250	Vacuum
HfB_2	Fe	100	1550	Vacuum
HfB_2	Ni	99	1480–1600	Vacuum

1.4.3.2 Fe-TiB_2 pseudo-binary phase diagram

Fe-TiB_2 composites were first proposed in the usage of high modulus steels (HMS) in automobile components for which both stiffness and lower density are required.

Since then, a deep thermodynamic knowledge of phase equilibria in Fe-Ti-B ternary is extremely scarce, but investigations of the pseudo-binary Fe-TiB_2 system have been reported.[53-55] Pseudo-binary phase diagrams are sketched in Fig. 1.7(a), TiB_2 and Fe form a simple eutectic system at 7mol.% TiB_2 with a eutectic point of 1340 °C. It is similar but within a narrower composition range in Fig. 1.7(b) indicating a eutectic reaction of TiB_2 and Fe at approximate 7mol.% TiB_2 with a eutectic point of 1633 K. However, the eutectic temperature is revealed to be 1613 K, as displayed in Fig. 1.7(c), which is about 373 K lower compared with that in Fig. 1.7(a) and Fig. 1.7(b). It is noticeable that the thermodynamic calculations employed are prone to be inaccurate owing to oversimplification of the thermodynamics involved and to the inaccuracy of the thermodynamic data employed. All the authors depict a eutectic reaction on the monovariant line of liq./TiB_2 + Fe which represents the ternary eutectic. But Ottavi et al.[55] summarizes that a quasibinary behavior exists along the line TiB_2-Fe containing 2-3at. %Ti not along the line of TiB_2-Fe, and the eutectic temperature locates at about 1593 K. And their temperatures and compositions differ considerably depending on the authors. Therefore, the experimental data can be used as a basis for a relevant thermodynamic description of the investigated ternary system.

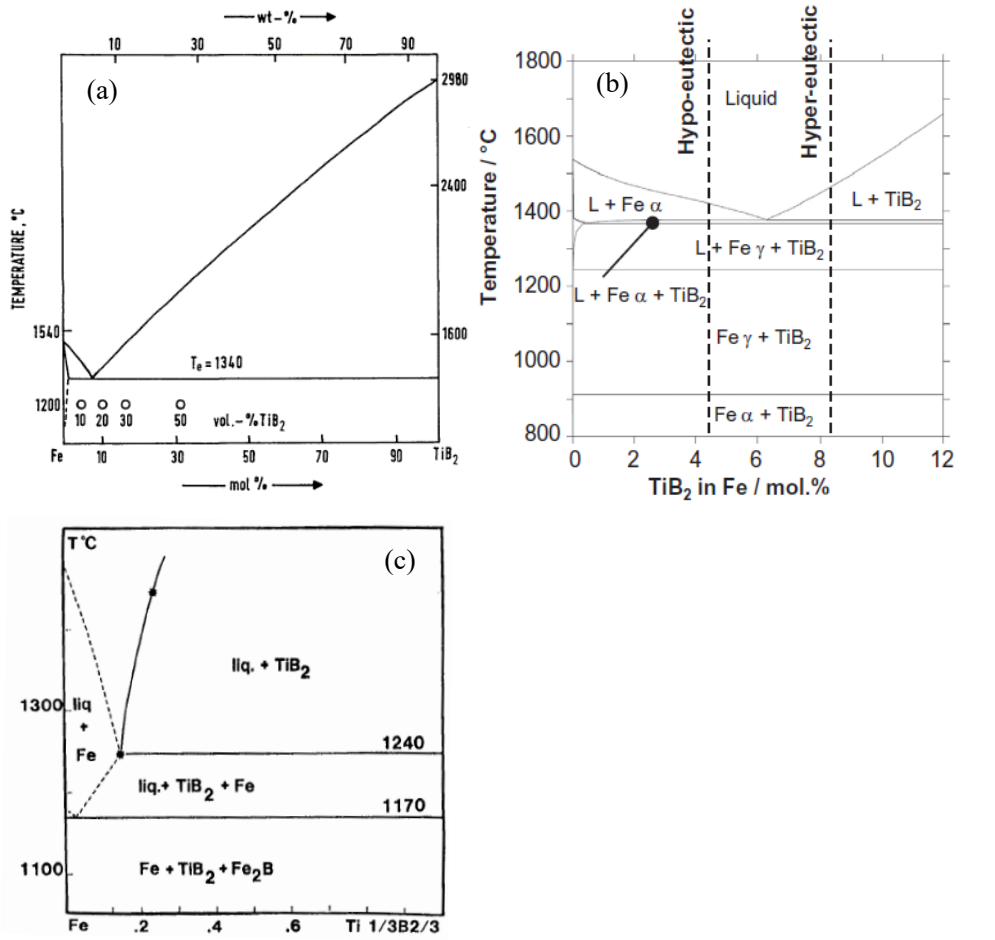

Fig. 1.7 Section of the pseudo-binary Fe–TiB_2 phase diagram in (a) B.S. Terry's work[53] (b) H. Springer's work[54] calculated with ThermoCalc and (c) L. Ottavi's work[55].

1.4.3.3 Interface cohesion between Fe and TiB_2

X.Y. Sun et al[56] reported that as the cohesive energy and cohesive strength of the interface increases, the failure mechanisms of interpenetrating phase composites vary from the interface damage to the failure of the weak phase. S. Lartigue-Korinek et al[57]. reported that Fe-TiB_2 composites has been successfully hot rolled and the very limited final damage is attributed to a strong interfacial cohesion and to the occurrence of a significant plastic deformation inside the TiB_2 particles. Interfaces between Fe and TiB_2 particles are mainly parallel to dense planes of the diboride, with a preferential growth of prismatic planes $\{1\ 0\ \bar{1}\ 0\}$ as shown in Fig. 1.8(a). L. Cha et al[58] also reported the preferred interface planes for diboride particles are prismatic planes and the basal plane. Interfacial misfit dislocations occur at interfaces parallel to the prismatic planes, and no intermediate phase such as oxides or non-stoichiometric borides has been revealed as

shown in Fig. 1.8(b).[59] These results strongly support the good interfacial cohesion assumed for this novel steel-based composite displaying enhanced mechanical behavior.

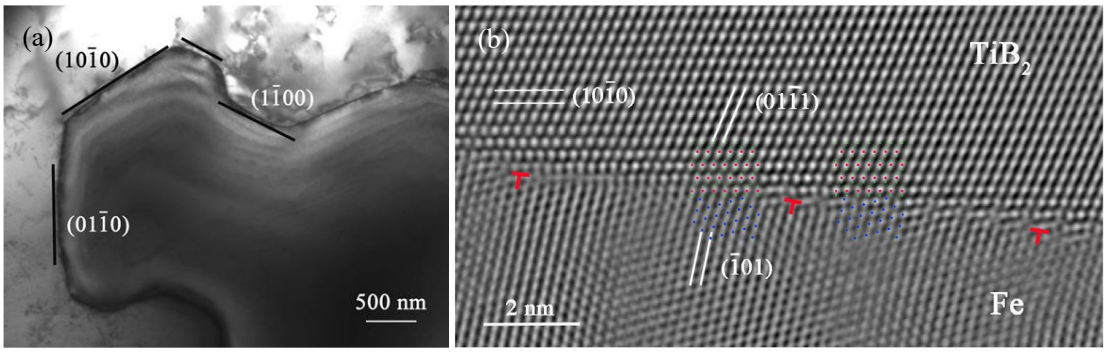

Fig. 1.8 Interfacial cohesion between Fe and TiB_2: (a) TEM image[58] and (b) HRTEM image[59].

1.4.3.4 Mechanical, wear and fatigue properties of Fe-TiB_2 composites.

A good interfacial cohesion between Fe and TiB_2 has been confirmed as introduced above. It is widely recognized that a good interfacial cohesion between matrix and reinforcement has a positive effect on mechanical and wear properties of composites. S. Lartigue-Korinek et al.[57] fabricated Fe-13vol.%TiB_2 composites by eutectic solidification. Ultimate tensile strength (UTS) of 500 MPa and elongation of 23% of hot-rolled Fe-13vol.%TiB_2 composites were attained under a tensile test. Z. Hadjem-Hamouche et al.[59] reported that the TiB_2-reinforced steel matrix composites by in situ precipitation of the TiB_2 particles during eutectic solidification. The total volume fraction of TiB_2 was measured to be about 14% using image analysis on SEM images. A great improvement in specific stiffness (>20%), and good strength/ductility trade-off were obtained. Besides, UTS of 510 MPa and elongation of 17% of hot-rolled Fe-14vol.%TiB_2 composites were obtained under a tensile test. The UTS of the hot-rolled Fe-14vol.%TiB_2 composites was 1.7 folds higher than that of reference steels. M. Ziemnicka-Sylwester et al.[60] reported that the TiB_2-based 35vol.% Fe–matrix cermets were fabricated by the Self-propagating High-temperature Synthesis method. The bending strength and compressive strength were 350 MPa and 1050 MPa, respectively. D.H. Bacon et al.[61] studied the fatigue and fracture mechanisms of steel-based metal

matrix composite (MMC) fabricated by hot isostatic pressing. The composite was comprised of a 316L austenitic matrix reinforced with 25 wt.% TiB_2. A UTS of 1100 MPa which was 1.4 folds than that of 316L steels and a fracture toughness of 29.6 $MPa\sqrt{m}$ were obtained for this material. H. Zhang et al.[62] investigated novel pathways to improve the mechanical properties of liquid metallurgy produced Fe-TiB_2 based high modulus steels (HMS) by controlled solidification kinetics. A UTS of 500 MPa and elongation of 26% were obtained. H. Springer et al.[63] presented a new class of nano-structured steel-TiB_2 composites with about 15 vol.% TiB_2 synthesized in-situ by bulk metallurgical spray-forming. An excellent UTS of almost 900 MPa and elongation of 23% were obtained. This promotes high stiffness, high strength and yet ductile materials. In a word, the mechanically properties of TiB_2 reinforced Fe or steel matrix composites can be significantly improved compared with that of the unreinforced matrix.

C.C. Degnan et al.[64] investigated dry reciprocating sliding wear behavior of steel matrix composites reinforced by TiB_2 particulates. The unreinforced reference steel was investigated at room temperature against a white cast iron counterface. Fe–TiB_2 composites exhibited wear rates three folds greater than that of the unreinforced alloy. The improved wear resistance is due to the load bearing capability of the TiB_2 and its ability to reduce metal to metal contact during sliding. S.C. Tjong et al.[65] studied the dry sliding wear behavior of 20 vol.% TiB_2 reinforced AISI 304 stainless steel by hot isostatic pressing by means of the pin-on-disc technique. The delamination type of adhesive wear is considered responsible for high wear loss of AISI 304 stainless steel. however, hard TiB particles serve as barriers for dislocation motion, contributing to further hardening of subsurface region. In addition, it is believed that the reinforcing particles are aligned along the sliding direction and redistributed over the top surface region of composites. Therefore, the wear resistance can be improved by adding TiB_2 particulates.

1.5 Introduction of spark sintering

Spark sintering is a newly developed sintering technique compared with the conventional sintering techniques, such as hot pressing (HP), hot isostatic pressing (HIP). The main feature of spark sintering differing from the conventional ones is that the sintering process is assisted by a low voltage, pulsed direct current (DC) which directly passes through the graphite die, as well as the powders. And hence, it is also termed as field assisted sintering technique or pulsed electric current sintering. The Joule heat produced by spark sintering is internal as shown in Fig. 1.9(a), while the heat is provided from the external heating unit as shown in Fig. 1.9(b).

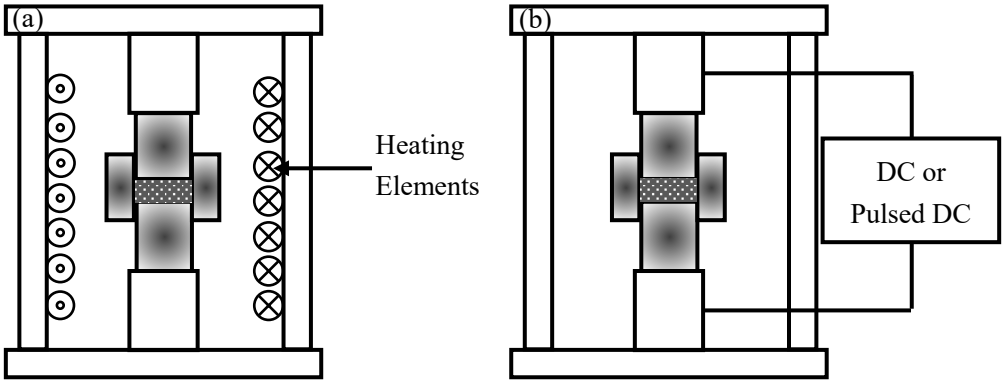

Fig. 1.9 Schematic illustrations of (a) HP and (b) SPS.

1.5.1 Historical Background

The first attempt of utilizing electric current to assist sintering dates to 1906, In 1913, a US patent invented with regard to protecting a current-assisted sintering system technique working at vacuum. In 1933, Taylor initiated the application of external electric current to assist sintering. Later, in 1944, Cramer invented a resistance sintering method by using a spot-welding machine. In 1955, Lenel adopted a spot-welding machine for the metals sintering as well. In the 1960s, Inoue proposed the concept of densifying materials by an electric discharge process and put forward that a pulsed current had a positive effect on the densification of compacts. In the late 1970s, the study the compacting of metal powders via using electric discharge compaction or electric discharge sintering was also investigated by some researchers. Up to 1990s, the first commercially available plasma activated sintering (PAS) and spark plasma

sintering (SPS) machines was developed by Sumitomo Heavy Industries Ltd.[66,67] Since then, some countries or companies started to make the similar set-ups on the principle of pulsed DC current assisting sintering.

1.5.2 Mechanism

Spark sintering is the state of art sintering technique which can fabricate a wide range of both novel and conventional materials. And hence, different kinds mechanisms have been put forward to interpret the improved and enhanced sintering abilities of spark sintering process. Up to now, the most prevailing point is the occurrence of plasma during the pulse sintering process. As it was originally named by Inoue and the inventors of spark sintering manufactures. They believed that the pulsed electric current caused the discharge and even plasma between the contact points of powder particles. However, a major disagreement still exists concerning the fundamental understanding of the mechanisms of spark sintering, specifically, with respect to the occurrence of spark plasma in the sintering process, duo to the complexity of combination of the thermal, electrical and mechanical processes occurred during spark sintering. D.M. Hulbert et al.[68] proposed an opposing view titling a discussion on the absence of plasma in spark plasma sintering. They performed the experiments by utilizing in situ atomic emission spectroscopy, direct visual observation and ultrafast in situ voltage measurements proving that no sign of plasma, sparking or arcing occurred during the spark sintering process, either during the initial or in the final stages of sintering was observed in various spark sintering conditions based on several different powders. Whereas, Z.H. Zhang et al.[70] report the proof of the occurrence of spark discharge based on the direct visual observations and characteristic microstructure analysis. In his study, it is pointed out that momentarily spark discharge was occurred on the interface between the punches and that sputtered microstructure of copper and the strip microstructure of titanium between TiB_2 particles were observed. Till now, the nature of the spark sintering mechanism is still under debate.

Despite of existing disagreement, the most widely accepted viewpoint is still the occurrence of plasma. Because existence of plasma occurrence can well explain the excellent sintering ability of spark sintering, on the other hand, it is in accordance with

the commercial publicity of spark sintering manufacturers. Therefore, it is considered that the occurrence of spark or plasma during spark sintering contribute to producing momentarily localized high temperatures of from several to ten thousand K in the gaps between the powder particles when pulsed electric current is applied, even though the controversy still exists. M. Suárez et al.[67] classified pulse sintering process into 5 steps. (I) initial stage of spark discharging by pulse energization; (II) generation of spark plasma; (III) vaporization and melting action on the particles surface; (IV) generation of spark impact of pressure, sputtering of vaporized or molten particles; (V) enhanced neck growth in the presence of spark plasma.

Another mechanism of densification in spark sintering process which covering the whole sintering process was put forward. The densification process comprises of three stages.[71] As shown in Fig. 1.10, the first stage is the neck generation stage by microscopic welding with melting and vaporization at the contact points of powder particles; in the second stage where either local plastic deformation of the contact points of powder particles or uniform plastic deformation of the entire particle occurs; in the third stage in which sintering pores are reduced or eliminated duo to creep deformation. The mechanism of densification mentioned above is also confirmed in metal-ceramic and metal-carbon composites. S.M. Kang et al.[72] studied the sintering behavior of FeB-10Fe composites. It is concluded that the plastic deformation and power law creep deformation of Fe phase contributed to the increment of densification rate of FeB-10Fe compacts before and after reaching the maximum densification rate, respectively. Z.F. Xu[73] investigated the densification mechanism of spark sintering of Al-10vol.% VGCNFs composites. It is also considered that the densification mechanism of Al-10vol.% VGCNFs composites is ascribed to plastic deformation (second stage) and creep deformation (third stage) of Al other than VGCNFs.

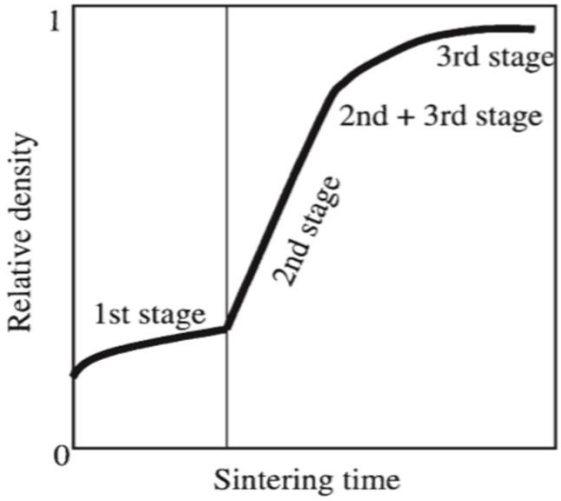

Fig. 1.10 Schematic illustration of densification process in sparking sintering for metallic powders.[71)]

1.5.3 Advantages over HP

In the powder metallurgy (PM) field, HP and HIP were the most widely used techniques to sinter compacts. However, SPS has exhibited numerous advantages over traditional ones, such as ease of operation, accurate control of sintering energy, high reproducibility, safety, reliability et.al. since its applications. Besides, there are some major merits in SPS over HP or HIP.

The heat source is derived from the application of electric current in both SPS and HP. Nevertheless, in SPS, the heating rate depends on the geometry of the sample ensemble, its thermal and electrical properties, and on the electric power supplier. As mentioned before, momentarily localized high temperature is generated due to the occurrence of spark plasma in pulse sintering. Subsequently, resistance sintering, electric current directly passes through the graphite die, as well as the powders in the case of being electrically conductive. Hence, the Joule heat is generated internally, and heating rate can be as high as 1000 K/min. On the contrary, in HP, the samples and graphite molds are heated by the radiation heat released from the wrapped heating wire convection of inert gases in the chamber. As a consequence, samples can be densified as rapid as in several minutes in SPS, as opposed to a few hours in HP. This fact results in a favorable sintering behavior with less grain growth and suppressed powder

decomposition.

The direct effect of rapid heating rate in SPS on sintering process is energy saving, which differs from the HP. A lot of energy is wasted during hours' sintering because the whole chamber is heated, and the samples absorb the heat externally. The oxide layers absorbed gases and dangled functional group can be eliminated duo to the local vaporization caused by high temperature. Due to the rapid heating rate in SPS, the grain size can be drastically restrained, and still the sample is highly densified. While it is difficult in HP process, because sintered compacts are either undersinterred or coarsening in grain size.

SPS is capable of synthesizing a wide range of both conventional and novel materials, especially materials with low sinterability, due to those advantages summarized above. W, Re, Ta, Mo, Nb, and Hf metals are a class of refractory materials possessing melting points over 2000 °C with high melting point, excellent mechanical properties, wear resistances at high temperature as well as remarkable electrical and thermal conductivity[66]. Therefore, it is suitable for them in high temperature applications. whereas, it is very difficult to consolidate them at moderate conditions due to the refractoriness of these metals and alloys. Besides, refractory metals or alloys fabricated by HP often accompanied with undesirable grain coarsening. Z.Z. Fang et al.[70] conducted that pure W powders with size of 2 μm was consolidated at 2273 K by HP accompanied by a 10-fold increase in grain size. On the contrary, O. El-Atwani et al.[74] performed that Pure W powders with an average particle size of about 1 μm were sintered to high density with almost no grain growth at a temperature below 1673 K by SPS. Hence, SPS is a viable method to sinter refractory metals and alloys.

Similar with refractory metals, transition metal carbides, nitrides and borides materials belong to a family of materials with outstanding hardness, high melting point, exceptional electrical and thermal conductivities, sample metallic structures etc.[75-79] This combination of properties makes them a promising material in various applications, such as hardmetals[80,81], wear-resistant parts[82], surface coating[83]. However, this class of materials is different to sinter because of low self-diffusion coefficient[84]. Generally, high sintering temperature is required to achieve fully densification, but grain coarsening is also inevitable. SPS is perfect solution to this problem since it can sinter

compacts to their full densification with less grain growth and suppressed powder decomposition in a short time. Similar with transition metal ceramics.

Functionally gradient materials (FGMs) are characterized by the gradual change in composition and structure over the whole volume of materials, which causes the corresponding variation in the properties of materials. Besides, they are also considered as candidates for a various industrial usage because their excellent properties.[85] Temperature gradient can be achieved by specially designed molds as shown in Fig. 1.11 The composition variation can be obtained by layered materials. Numerous layered materials have been successfully fabricated by SPS. E. Jajarmi et at.[86] Fabricated a dense and crack-free FGMs by SPS, which containing 3mol%Y_2O_3-partially stabilized ZrO_2 (3Y-PSZ) and 316L stainless steel. S.Z. Jin et. al[87] also reported fabrication of the TiB_2/(TiB_2+AlN)/AlN/(AlN+Cu)/Cu FGMs by SPS. The results show that the layered composites were highlighted by a dense microstructure, which changed gradually along a composition gradient.

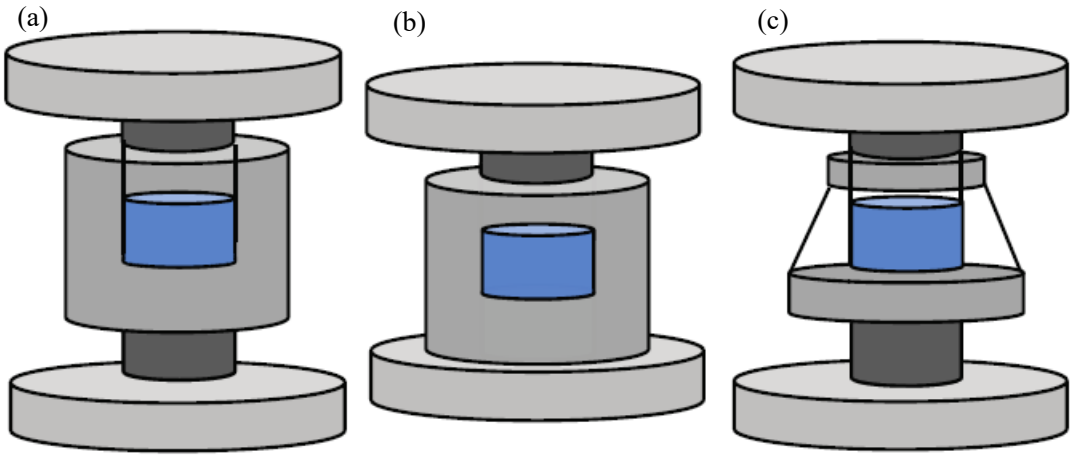

Fig. 1.11 (a) Symmetric configuration of mold, (b) and (c) asymmetric configuration of mold with asymmetric graphite die.[85]

Nano-structured materials (NSMs) have arisen a great interest in recent years due to their extraordinary physical, chemical, biological, thermal or electrical properties with enhanced performance over their bulk counterparts. And fabrication of a variety of NSMs by SPS have been widely reported.[88,89] The dominating issue of synthesizing NSMs is how to restrain the grain growth below 50 nm or even less than 10 nm. As

reported above, the ultrafast heating rate of SPS can be as high as 1000 K/min, which means spark sintering process can be completed in just a few minutes. On the contrary, it is not possible that a sintering process can be realized by HP.

In a word, spark sintering technique is capable of sintering all the materials that HP is. In addition, some materials beyond the capability of HP can also be sintered by spark sintering.

1.6 Objective and outline of the thesis

The conventionally commonly used hot stamping materials are SKD61. The current states of this materials are relatively low in wear resistance and thermal conductivity, which result in the low production proficiency and high maintenance cost. In addition, complex post heat treatments have to be applied to SkD61 to acquire specific properties before being put into practice. However, these post heat treatments are not only costly but also environmentally unfriendly. Therefore, in order to solve the problems, the idea of fabricating a new generation of materials for the usage of hot stamping has been put forward. Based on the summary above, Fe (steel)-TiB_2 composites show great potential of possessing both high TC and hardness. And thus, the objective of this thesis is to develop TiB_2 reinforced Fe (steel) matrix composites with both high TC and hardness.

In Chapter 1, the urgency of environmental protection is reviewed, and hence, in order to solve the corresponding problem, application of high strength steels on automobile industry for the purpose of weight reduction is proposed. However, the challenge arises with regard to SKD61steels used for producing high strength steels by hot stamping technique are introduced. Besides, the reasons for selecting spark sintering technique, Fe and TiB_2 as starting powders and the advantages of Fe-TiB_2 composites over other materials for hot stamping materials are described in detail.

Powder metallurgy method is selected to fabricate Fe (steel)-TiB_2 composites in this study. For the purpose of obtaining homogenously distributed TiB_2 Fe matrix composites, elaborate mixing method by ball mixing is designed and illustrated in chapter 2.

The possible reactions are identified from the literature investigation. However, in order to obtain the optimum sintering parameters of Fe-TiB_2 composites, different sintering temperatures and holding times were investigated. In addition to that, the thermal conductivity, hardness of sintered compacts and reaction mechanism between Fe and TiB_2 were researched as well in chapter 3.

From the results obtained from chapter 3, Fe is not chemically stable in pure Fe which lead to the formation of Fe_2B and TiC. And therefore, new matrix of Fe-xTi (x=5, 10) alloys were designed to prevent TiB_2 from decomposing in chapter 4. The effect of Ti addition in Fe on the fabrication of Fe_2B free TiB_2 reinforced Fe base composites.

Moreover, residual TiB_2, thermal conductivity, hardness and compression test of sintered compacts were carried out in chapter 4.

The results from above chapters were summarized in Chapter 5.

References

1) "CO_2 in the atmosphere just exceeded 415 parts per million for the first time in human history". Retrieved 31 August 2019.
2) Data from United States Environmental Protection Agency, 2017.
3) N. Oba: CO_2 Emissions Reduction in Japan's Road Transport Sector. COP22 Side Event. "Measures in Response to Global Warming Problems of the Transport Sector in Japan". 2016
4) J. Ishii, M. Osuga, T. Okada, H. Miyazaki, M. Koseki, and K. Tanikoshi: Hitachi Review. 57 (5) (2008) 185.
5) L.C. Casals, E. Martinez-Laserna, B.A. García and N. Nieto: J. Clean. Prod. 127 (2016) 425-437.
6) G. Fontaras, N.G. Zacharof and B. Ciuffo: Prog. Energ. Combust. 60 (2017) 97-131.
7) J.C. Benedyk: In Materials, design and manufacturing for lightweight vehicles. (2010) 79-113.
8) H.J. Kim, C. McMillan, G.A. Keoleian and S.J. Skerlos: J. Ind. Ecol. 14 (6) (2010) 929-946.
9) P.K. Mallick: In Materials, Design and Manufacturing for Lightweight Vehicles. (2010) 275-308.
10) L. Ye, G. Gu, X. Zhang, D. Sun, H. Jiang and P. Zhang: Mater. Sci. Eng. A. 590 (2014) 97-100.
11) W.J. Joost and P.E. Krajewski: Scr. Mater. 128 (2017)107-112.
12) M. Kiani, I. Gandikota, M. Rais-Rohani and K. Motoyama: J. Magnes. Alloy. 2 (2) (2014) 99-108.
13) B.R. Powell and P.E. Krajewski and A.A. Luo: In Materials, Design and manufacturing for lightweight vehicles. (2010) 114-173.
14) C. Liu, J. Han, X. Zhang, C. Hong and S. Du: Carbon. 59 (2013) 551-554.
15) X. Zhang, Q. Li, T.G. Holesinger, P.N. Arendt, J. Huang, P.D. Kirven and L. Zheng: Adv. Mater. 19 (23) (2007) 4198-4201.
16) N. Baluch, Z.M. Udin and C.S. Abdullah: Engineering, Technology & Applied Science Research. 4 (4) (2014) 686-689.

17) C.M. Tamarelli: Steel Market Development Institute. Michigan (2011).

18) H. So, D. Faßmann, H. Hoffmann, R. Golle and M. Schaper: J. Mater. Process. Technol. 212 (2) (2012) 437-449.

19) H. Karbasian and A.E. Tekkaya: J. Mater. Process. Technol. 210 (15) (2010) 2103-2118.

20) C. Wang, J. Chen, Z.C. Xia and F. Ren: The International Journal of Advanced Manufacturing Technology. 69 (1-4) (2013) 797-803.

21) Ö.N. Cora, A. Ağcayazı, K. Namiki, H. Sofuoğlu and M. Koc: Tribol. Int. 52 (2012) 50-60.

22) Z. Wang, P. Liu, Y. Xu, Y. Wang and Y. Zhang: Procedia Engineering. 81 (2014) 1725-1730.

23) K.I. Mori, P.F. Bariani, B.A. Behrens, A. Brosius, S. Bruschi, T. Maeno and J. Yanagimoto. CIRP Annals. 66 (2) (2017) 755-777.

24) A. Ormaetxea, A. Aramburu and I. Belategi: Improved Productivity and Energy Consumption on Press Hardening by Means of Mechanical Servo Press Technology. Proceedings of 4th International Conference on Hot Sheet Metal Forming of High-Performance Steel, Luleå. (2013) 185–190.

25) S.H. Yeh, L.H. Chiu, T.L. Chuang and C.Y. Wu: Mater. Trans. (2013) M2013019.

26) I. Valls, A. Hamasaiid and A. Padré: Journal of Physics: Conference Series. IOP Publishing. 896 (1) (2017) 012046.

27) J. Kohopää, H. Hakonen and S. Kivivuori: Wear 130 (1) (1989) 103-112.

28) B.S. Suh and W.J. Lee: Thin Solid Films 295 (1-2) (1997) 185-192.

29) S.Y. Sirin, K. Sirin and E. Kaluc: Mater. Charact. 59 (4) (2008) 351-358.

30) C.M. Suh, B.W. Hwang and R.I. Murakami: Mater. Sci. Eng. A 343 (1-2) (2003) 1-7.

31) E. Pagounis and V.K. Lindroos: Mater. Sci. Eng. A 246 (1-2) (1998) 221-234.

32) E.G. Moghaddam, N. Karimzadeh, N. Varahram and P. Davami: Mater. Sci. Eng. A 585 (2013) 422-429.

33) A. Persson and S. Hogmark and J. Bergström: Int. J. Fatigue 26 (10) (2004) 1095-1107.

34) J.R. Davis: ASM speciality handbook, tool materials. Materials Park OH: ASM

International.

35) I.V. Angles, B. Casas, N. Rodríguez and U. Paar: Metall. Ital. 11 (2010) 23-28.

36) I.V. Angles: U.S. Patent 9,689,061[P]. (2017)

37) Hartman and A.Roy: "Recycling". Encarta. Archived from the original on 2008-04-14 (2009)

38) J. Pelleg: Mater. Sci. Eng. A. 269(1-2), (1999) 225-241.

39) M. Machida: Master Thesis, 2019.

40) R. Chang, J. Zang, Y. Wang, Y. Yu, J. Lu and X. Xu: Mater. Chem. Phys. 204 (2018) 154-162.

41) F. Kretz, Z. Gácsi, J. Kovács and T. Pieczonka: Surf. Coat. Technol. 180 (2004) 575-579.

42) R. Telle, L.S. Sigl, K. Takagi, Boride-Based Hard Materials, Handbook of Ceramic Hard Materials. 2000.

43) I. Azkona, F. Castro and J.M. Sánchez: Metall. Mater. Trans. A. 36 (2) (2005) 459-466.

44) K.E. Spear, P. McDowell and F. McMahon: J. Am. Ceram. Soc. 69 (1) 1986 C-4-C-5.

45) R.G. Fenish: NRM. 138 (1964) 1

46) E. Rudy: Ternary phase equilibria in transition metal-boron-carbon-silicon systems. part 5. compendium of phase diagram data[R]. AEROJET-GENERAL CORP SACRAMENTO CA MATERIALS RESEARCH LAB. (1969)

47) J. Thebault, R. Pailler, G. Bontemps-Moley, M. Bourdeau and R. Naslain: J. Less Common Met. 47 (1976) 221–233.

48) W. Jeitschko, R.Pottgenand R.D. Hoffman: Structural chemistry of hard materials. In Handbook of Ceramic Hard Materials, ed. R. Riedel. Wiley- VCH, New York. (2000) 2-40.

49) J.L. Murray, P.K. Liao and K.E. Spear: The B−Ti (Boron-Titanium) system. Bulletin of Alloy Phase Diagrams. 7 (6) (1986) 550-555.

50) R.G. Munro: J. Res. Natl. Inst. Stand. Technol. 105 (2000) 709–720.

51) A.D. Panasyuk and A.P. Umansky: J. Less Common Metals. 117 (1-2) (1986) 335-339.

52) A. Passerone, M.L. Muolo and D. Passerone: J. Mater. Sci. 41 (16) (2006) 5088-5098.

53) B.S. Terry and O.S. Chinyamakobvu: Mater. Sci. Technol. 8 (6) (1992) 491-499.

54) H. Springer, R.A. Fernandez, M.J. Duarte, A. Kostka and D. Raabe: Acta Mater. 96 (2015) 47-56.

55) L. Ottavi, J.M. Chaix, C.H. Allibert and H. Pastor: Trans Tech Publications. 25 (1992) 543-550.

56) X.Y. Sun, G.K. Xu, J.H. Zhang and Y.J. Xu: Micro & Nano Letters. 9 (10) (2014) 697-701.

57) S. Lartigue-Korinek, M. Walls, N. Haneche, L. Cha, L. Mazerolles and F. Bonnet: Acta Mater. 98 (2015) 297-305.

58) L.M. Cha, S. Lartigue-Korinek, M. Walls and Mazerolles: Acta Mater. 60 (18) (2012) 6382-6389.

59) Z. Hadjem-Hamouche, J.P. Chevalier, Y. Cui and F. Bonnet: Steel research international. 83 (6) (2012) 538-545.

60) M. Ziemnicka-Sylwester, L. Gai and S. Miura: Mater. Des. 69 (2015) 1-11.

61) D.H. Bacon, L. Edwards, J.E. Moffatt and M.E. Fitzpatrick: Int. J. Fatigue. 48 (3) (2013) 39-47.

62) H. Zhang, H. Springer, R. Aparicio-Fernández and D. Raabe: Acta Mater. 118 (2016) 187-195.

63) H. Springer, C. Baron, A. Szczepaniak, V. Uhlenwinkel and D. Raabe: Sci. Rep. 7 (1) (2017) 2757.

64) C.C. Degnan and P.H. Shipway: Wear. 252 (9-10) (2002) 832-841.

65) S.C. Tjong and K.C. Lau: Mater. Lett. 41 (4) (1999) 153-158.

66) O. Guillon, J. Gonzalez-Julian, B. Dargatz, T. Kessel, G. Schierning, J. Räthel and M. Herrmann: Advanced Engineering Materials. 16 (7) (2014) 830-849.

67) M. Suárez, A. Fernández, J.L. Menéndez, R. Torrecillas, H. U. Kessel, J. Hennicke, R. Kirchner and T. Kessel: Sintering Applications. IntechOpen. (2013)

68) D.M. Hulbert, A. Anders, J. Andersson, E.J. Lavernia and A.K. Mukherjee: Scr. Mater. 60 (10) (2009) 835-838.

69) Z.H. Zhang, Z.F. Liu, J.F. Lu, X.B. Shen, F.C. Wang and Y.D. Wang: Scr. Mater.

81 (2014) 56-59.

70) Y. Jing, H. Yuan and Z. Lian: Materials 11 (10) (2018) 2046.

71) K. Matsugi, O. Yanagisawa and G. Sasaki: J. Jpn. Soc. Powder Powder Metallurgy, 56 (2009) 355-370.

72) S.M. Kang, Z.F. Xu, Y.B. Choi, K. Fujita, K. Matsugi and J.K Yu: Mater. Trans 57 (5) (2016) 600-607.

73) Z.F. Xu: Doctoral thesis. Hiroshima University. 2010.

74) Z.Z. Fang: Sintering of Advanced Materials, Woodhead Publishing Limited, Sawston, Cambridge. UK 2010.

75) A. Bellosi, F. Monteverde and D. Sciti: International Journal of Applied Ceramic Technology. 3 (1) (2006) 32-40.

76) T. Venkateswaran, B. Basu, G.B. Raju and D.Y. Kim: J. Eur. Ceram. Soc. 26 (13) (2006) 2431-2440.

77) H.C. Kim, I.J. Shon, J.E. Garay and Z.A. Munir: Int. J. Refract. Met. Hard Mater. 22 (6) (2004) 257-264.

78) T. Nishimura, M. Mitomo, H. Hirotsuru and M. Kawahara: J. Mater. Sci. Lett. 14 (15) (1995) 1046-1047.

79) Z.Y. Fu, J.F. Liu, H. Wang, D.H. He and Q.J. Zhang: J. Mater. Sci. 20 (9) (2004) 1097-1099.

80) A. Koutsospyros, W. Braida, C. Christodoulatos, D. Dermatas and N. Strigul: J. Hazard Mater.136 (1) (2006) 1-19.

81) Q. Zhang, N. Lin and Y. He: Int. J. Refract. Met. Hard Mater. 38 (2013) 15-25.

82) J. Kübarsepp, H. Klaasen and J. Pirso: Wear. 249 (3-4) (2001) 229-234.

83) L.M. Berger, W. Hermel, P. Vuoristo, T. Mantyla, W. Lengauer and P. Ettmayer: Thermal Spray: Practical Solutions for Engineering Problems. (1996) 89-9.

84) M. Tokita: Trans Tech Publications. 63 (2010) 322-331.

85) E. Jajarmi, L. Desogus, R. Orru, S.A. Sajjadi and G. Cao: Ceram. Int. 42 (7) (2016) 8351-8359.

86) S.Z. Jin, H.L. Zhang, J.F. Li and S.S. Jia: Trans Tech Publications. 280 (2005) 1881-1884.

87) L. Wang, J. Zhang and W. Jiang: Int. J. Refract. Met. Hard Mater. 39 (2013) 103-112.

88) P. Angerer, L.G. Yu, K.A. Khor, G. Korb and I. Zalite: J. Eur. Ceram. Soc. 25 (11) (2005) 1919-1927.

89) A. Teber, F. Schoenstein, F. Têtard, M. Abdellaoui and N. Jouini: Int. J. Refract. Met. Hard Mater. 30 (1) (2012) 64-70.

Chapter 2

Optimization of mixing parameters for Fe-TiB_2 powder mixtures

2.1 Introduction

The mixing or blending is the process of thoroughly mixing several different materials into a homogeneous mixture. This process is of great importance to many industries such as ceramics, metallurgy and composites.[1)] Because spatial distribution of reinforcements in matrix or agglomerates exert an influence on the mechanical properties of metal matrix composites. D. Zhang et al.[2-4)] investigated the effect of spatial distribution of SiC particles on the mechanical properties of Al-10vol.%SiC composites. Results show that the more homogenous spatial distribution of particles in matrix contributes to higher mechanical properties compared with the composites with strong particles clustering, as composites with a strong particles clustering are more vulnerable to delamination produced at small strain. On the other hand, agglomerates in composites influence relative viscosity[5)], cause localized nonuniform shrinkage of sintered compacts and therefore result in poor mechanical properties.[6)] As a consequence, in the case of fabricating composites, particles clustering, and agglomerates are unfavorable and need to reduce to the uttermost in order to maintain the reliable mechanically properties and reproducibility.

Most of the studies focus on reducing the particle size.[7-12)] However, to author's knowledge, studies concerning how to acquire a homogenous mixture are limited. Due to the surface energy, fine particles (≤10 μm) tend to form agglomerates with size substantially larger than that of the primary particles because of electrostatic charges between particles during storage. The mechanism of deagglomeration in the mechanical milling is generally related to an impact motion of milling media, which lead to an induced shear and impact forces to break down the powder agglomerates most pronouncedly at the collision position of the milling balls.[13)] H. Ferkel et al.[14)] milled alumina and zirconia with monosized balls by planetary ball mill (PBM) at relatively low speed of 150 rpm for no more than 0.6 ks to disintegrate strong agglomerates. Both densities of green bodies and sintered compacts from conditioned powders are improved than that from unconditioned powders. Besides, it is reported that the multimodal sizes distribution of milling balls give rise to a greater number of collisions between ball to ball as well as ball to pot during milling[12)]. Hence, Jens Fruhstorfer et al.[15)] further investigated the effect of bimodal ball size distribution on dry ball mixing

and deagglomeration of alumina and zirconia composite fine powders. The result showed that the application of bimodal distributed balls was better to use either only small or large balls. This was interpreted that the small balls caused a better macroscopic mixing, but the large balls limited reagglomeration and therefore improved microscopic dispersion. In addition, deagglomeration became less insensitive to the mixing time by introducing the bimodal distributed ball size distribution. Compared with milling, mixing is less intense because chemical reactions are barely involved in process and each constituent keep almost same no matter in morphology or in composition after process.[9] Based on the investigations mentioned above, decreasing the rotational speed as well as reducing the number of large balls to reduce the specific impact energy between balls and introducing small balls to increase the contact points between balls[11] are favorable in mixing.

However, the collision between balls lead to wear of balls and pots. The wear debris exfoliated from balls and pots contaminate or change the composition of powders or even the final sintered compacts. In mixing technology, wear debris are undesirable and to some extent, unavoidable. In order to alleviate the contamination arisen from wear debris, liquid media such as water, ethanal and acetone are generally introduced into powder mixture, since the cascading speed of balls is greatly reduced from due to the drag force of the viscous slurry[11] and thus the impact force between balls is weakened. On the other hand, liquid media weaken the inter-agglomerate bonding by diluting powders into a low viscous slurry and hence agglomerates are more easily to disintegrate. therefore, wet mixing is more efficient than dry mixing, especially in powder mixture preparation for composites.[2,16] Nevertheless, what is worth noticing is the segregation of metal and reinforcement particles caused by density-induced sedimentation rate difference may occur in metal-reinforcement particles slurry during the drying process. In order to avoid the occurrence of the powder segregation, a combination of wet/dry mixing is a promising method.

Despite the investigation of effect of ball size or bimodal ball size distribution on deagglomeration or dispersion of powders, to author's knowledge, up to now, application of trimodal ball size distribution on wet mixing in a PBM has not been reported yet. Moreover, in the case of composites comprising more than two

constitutions in initial stage, literatures with regard to how the spatial distribution of reinforcements is in matrix after sintering when the conditioned mixing parameters are applied to preparation of powder mixture for sintering are scarce. Namely, the spatial distribution of reinforcements in matrix has to be evaluated in order to confirm whether a conditioned mixing parameter is suitable or not for the investigating system. In this light, a combination of mixing parameters optimization and evaluation of spatial distribution in matrix is therefore proposed to obtain dispersion and deagglomeration result simultaneously.

In this chapter, the objective is to obtain optimal parameters for Fe-20%vol.TiB_2 composites by tailoring trimodal ball size distribution, rotational speed, and wet/dry mixing in a PBM as shown in Fig. 2.1 and by evaluating the spatial distribution of TiB_2 in Fe utilizing local number density 2-dimension average($[LND\text{-}2D]_{av}$) proposed by Sugio et al.[2-4)]

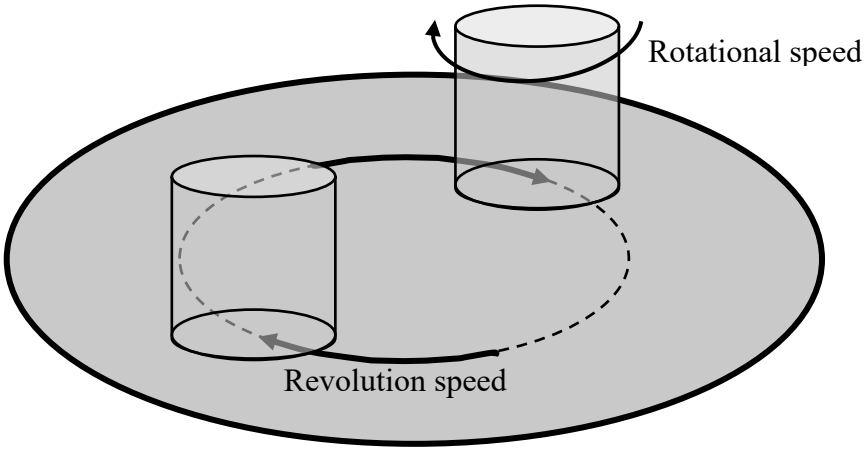

Fig. 2.1 Schematic illustration of PBM device.

2.2 Experimental procedure

2.2.1 Determination of rotational speed

The motion of the milling balls exerts great influence on the number of collisions, the ball velocity as well as the energy input to powder charge. The milling balls exhibit complex behaviors during milling process and the motion patterns can be roughly divided into three types which are cascading, cataracting and rolling as shown in Fig. 2.2. In the cascading pattern (Fig. 2.2a), the milling balls move around the bottom of the pot, while in the cataracting pattern (Fig. 2.2b), the balls undergo projectile motion from the wall and drop on the powder charge with high intensity. In the rolling or centrifuging pattern (Fig. 2.2c), balls move along the wall with almost no relative velocity.[17] The velocity of the rolling is defined as critical velocity which can be calculated by the following equation[18]:

$$Nc=42.29D^{-1/2} \quad (2.1)$$

Where Nc is the critical velocity in rotation per minute, D is the inner diameter of milling pot in meter. Apparently, the cataracting pattern is the most suitable one for milling and the velocity of cataracting pattern is approximately 60-70% of the critical velocity. The inner diameter of milling pot applied in this study is 0.07 m, so the critical velocity was calculated to be 160 rpm according to Eq. 2.1. Therefore, the rotational speed was determined to be 62.5% of the critical velocity (100 rpm) and 93.7% of the critical velocity (150 rpm) as a comparison.

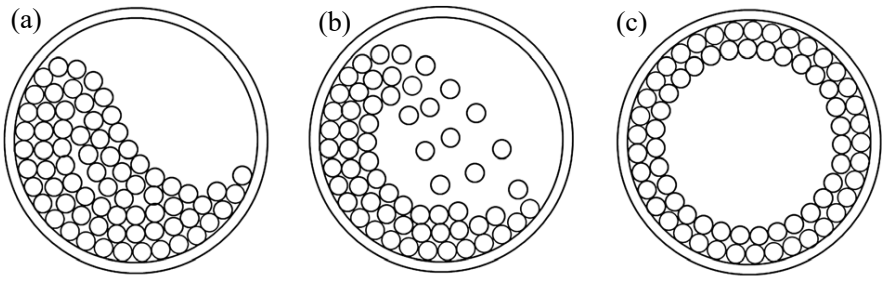

Fig. 2.2 Schematic illustration of ball motion pattern in a milling pot of a PBM (a) cascading, (b) cataracting and (c) rolling.[17]

2.2.2 Introduction of multimodal balls.

Smaller balls can reduce the kinetic energy (a negative source for milling efficiency) but increase number of contact points (a positive source). In this study, three kinds of stainless balls with successively declining diameters. Due to a lack of data for the determination of ball diameters used for PBM, the ball diameter was chosen based on bond's equation applied to tumbling mixers.

$$D_b = \sqrt{\frac{P_f \times W_i \times \sqrt{\frac{S_{gs}}{\sqrt{D}}}}{C \times V_{Cr}}} \tag{2.2}$$

Where, D_b is the top size of the grinding media in mm, P_f is size of the 80% passing in the fresh feed in μm, C is 200 for ball mills and 300 for rod mills, W_i is Work index in kWh/sht, (1 short ton = 907.2 kg), V_{Cr} is percentage of the critical speed, S_{gs} is specific gravity of feed in g/cm^3 and D is the inner diameter of in ft. In this study, P_f, C, W_i, V_{Cr}, S_{gs} and D are determined as 4 μm, 70, 200, 80 kWh/sht and 0.23 ft, respectively. Then D_b was calculated to be 8.2 mm. It is recommended that the size of large ball should be larger than the calculated one. Thus, the large ball size was selected as 9.5 mm. Thereafter, the medium and small balls were determined as 5 mm and 2 mm according to the principle of successive size reduction. The batch charge of 20vol.%TiB_2 and 80vol.% Fe was a selected as model composition to test the effects of the multimodal ball size distributions.

2.2.3 Selection of wet/dry mixing.

In this study, a combination of wet mixing and dry mixing was adopted since density-induced sedimentation rate difference occurred in Fe-TiB_2 slurry. The density of Fe and TiB_2 is 7.87 and 4.52 g/cm^3, respectively. Wet mixing of 10.8 ks was chosen because the weight of powder mixture increases dramatically from 10.8 to 14.4 ks as shown in Fig. 2.3 and dry mixing of 3.6 ks was selected because large number of wear debris will be introduced in to powder mixture if long mixing time is adopted. In addition, ethanol was chosen as dispersion medium, since Xu[16] investigated the effect of three dispersion medium of ethanol, acetone and butanol with different viscosity on the sedimentation rate of Al particle in 10vol.%VGCNFs/Al slurry and concluded that ethanol is the best dispersion media among the three media.

20vol.%TiB_2 and 80vol.% Fe of total amount of 15 g were placed in a stainless-steel jar with a volume of 250 cm^3 and then 25 mL ethanol which just submerse the balls and powders was added as a wet mixing agent. The total volume of the balls and slurry reached approximately 50% of the bottle height, which is considered effective for mixing. Hereafter, the jars were vacuumed for 0.3 ks. Stainless-steel balls with trimodal balls (combination of different ball size of 9.5, 5 and 2 mm) were used for mixing. As a rule of thumb, the weight ratio of balls to powders was 10:1 which is suitable for mixing. Wet mixing process was conducted in a PBM (Fritsch Pulverisette, Germany) at 100 rpm for 10.8 ks. Slurry of powder mixtures were dried in a fume hood and then dry mixed for 3.6 ks in a PBM.

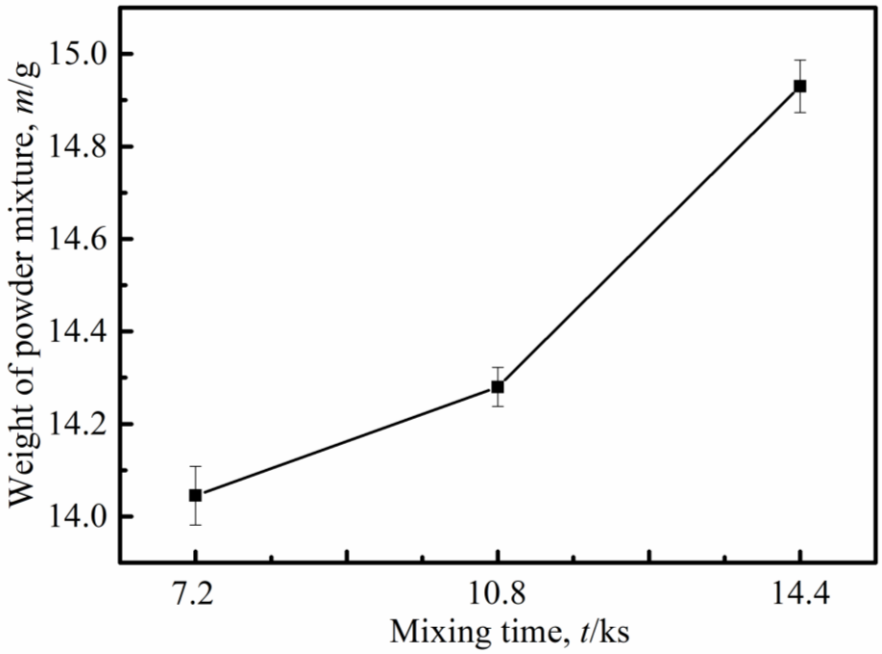

Fig. 2.3 Weight of powder mixture variation at different mixing times.

2.2.4 Introduction of LND2D

Particles are arrayed in 2-dimensionally hexagonal close packed ordering in an ideal case as Fig. 2.4(a), providing a given 2-dimensional particle number density, λ (particle numbers in unit area). A measuring circle with a gravity center (GC) of noticed particle and radius (R) are defined, so the number density in the circle is equal to the given value, including the GCs of the noticed and nearest neighbor particles. In this ideal case,

local number (LN) of all GC is equal to 7, and probability (P) and cumulative probability (CP) of LN is shown in Fig. 2.4(a'). However, in Poisson field where points are randomly distributed in 2-dimensional space as shown in Figure 2.4(b), probability of k, point number included in specified area locates at arbitrary position. Therefore, probability of GC number k, included in the measuring circle around a noticed particle is shown in Fig. 2.4(b'). If particles are arrayed in clustering state as displayed in Fig. 2.4(c)), right-shift of probability histogram of LN must occur, leading to larger LN as shown in Fig. 2.4(c'). And thus, the LN of GC in the measurement circle is considered as a proper method to evaluate spatial distribution of particulates in matrix.[2)]

In this chapter, normalizing measured LN divided by 7 of the ordering arrangements, named as [LND2D], will be adopted. The spatial distribution of TiB_2 in Fe matrix will be quantitatively evaluated by [LND2D]. At least 2000 TiB_2 particles were measured in each SEM image, and 7 SEM images were taken for each sintered compact. Average value of [LND2D] ([LND2D]av) for 7 SEM images of each sintered compact was obtained.

2.2.5 Spark sintering

Powder mixtures were loaded in a graphite die and consolidated by spark sintering (CS12567, Japan) technique. All spark sintering experiments were carried out at an applied pressure of 50 MPa and a vacuum condition ($<10^{-2}$ Pa). The die temperature other than the samples was monitored using R type thermocouple inserted into the hole of die. Samples were sintered at 1173 and 1373 K, heating rate of 100 K/min, for 0 and 0.3 ks. Finally, compacts with height of 10 mm and diameter of 10 mm were obtained.

2.2.6 Characterizations

Morphology of powders and microstructure of sintered compacts were observed by electron probe micron analyzer (EPMA, JXA-8900, JEOL, Japan). Chemical compositions of sintered compacts were characterized wavelength dispersive spectroscopy (WDS) equipped on EPMA. Vickers hardness was obtained by Vickers hardness tester (MHT-1, Japan) at a load of 5 kg and a dwelling time of 10 s. Thermal conductivities (λ) of sintered compacts were calculated by steady state method. Spatial distribution was evaluated by [LND-2D].

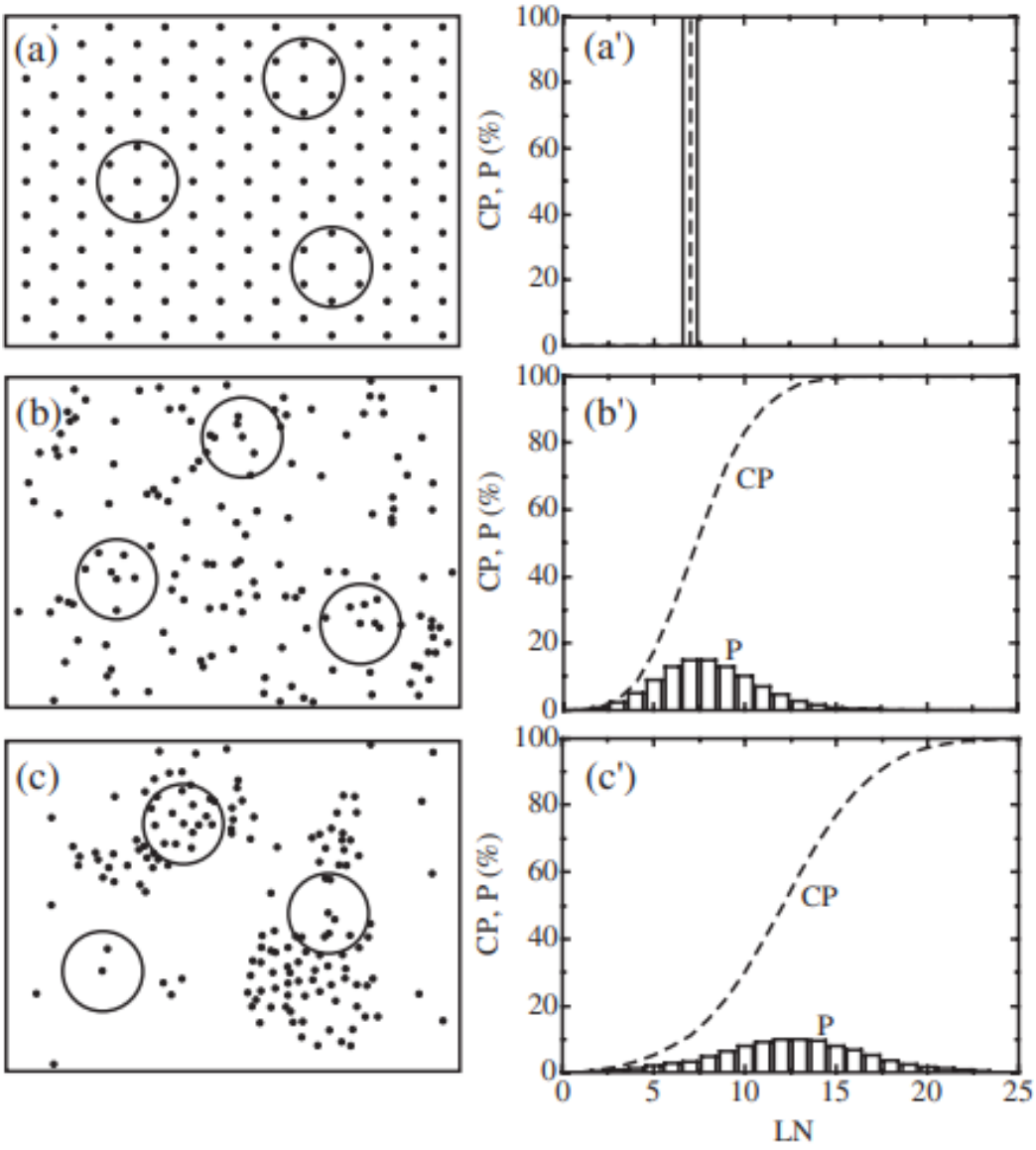

Fig. 2.4 2-dimensional arrangement types, (a) hexagonal closest ordering, (b) random and (c) clustering arrangement of the gravity center of particles; and probability (P) and cumulative probability (CP) distribution of local number (LN) in the measuring circle, (a')-(c').[2)]

2.3 Results and discussion

2.3.1 Criterion of evaluating homogeneity

The criterion of evaluating if a certain combination is feasible or not based on four points. First, a good combination of different size balls is considered to have a positive effect on slurry because of the sufficient impacts and frictions. Namely, the occurrence of sedimentation of powder mixtures after transferring to the plate indicates failure of mixing. Apparently, these cases will be eliminated. Second, weight change before and after wet mixing. The loss of total starting powders after mixing is inevitably. The occurrence of weight increase can be mainly ascribed to the introduction of wears debris from the collision between balls and between balls and inner wall of milling pot. Therefore, combinations of overweight after wet mixing will be screened out. The third point will be taken into consideration, if the aforementioned two cases do not occur. The error bar of Vickers hardness is another evaluation criterion. The smaller the error bar is, the more homogenous the microstructure of compact is. Fourth, direct microstructure evaluation by utilizing [LND-2D] which is capable of analyzing the distribution of reinforcements in matrix. An optimized combination of different size balls can be obtained based on the four points.

2.3.2 Morphologies of powders

Morphologies of starting powers are shown in Fig. 2.5. The given size of as-received pure Fe particles is 3~5 μm as shown in Fig. 2.5(a). The inset placed in the upper right corner is the magnified image corresponding to the marked area in Fig. 2.5(a), demonstrating that as-received Fe particles are mainly spherical, and some are with small satellites as marked in the inset. TiB_2 agglomerates are indicated in Fig. 2.5(b), and As-received TiB_2 particles basically presented as prismatic particles, such as a hexagonal shape as shown in the inset corresponding to the marked area in Fig. 2.5(b). Large hexagonal TiB_2 particles with size of about 2~3 μm corresponded to well-grown TiB_2. In contrast, some kinds of small TiB_2 were prismatic particles with size of approximate 500 nm.

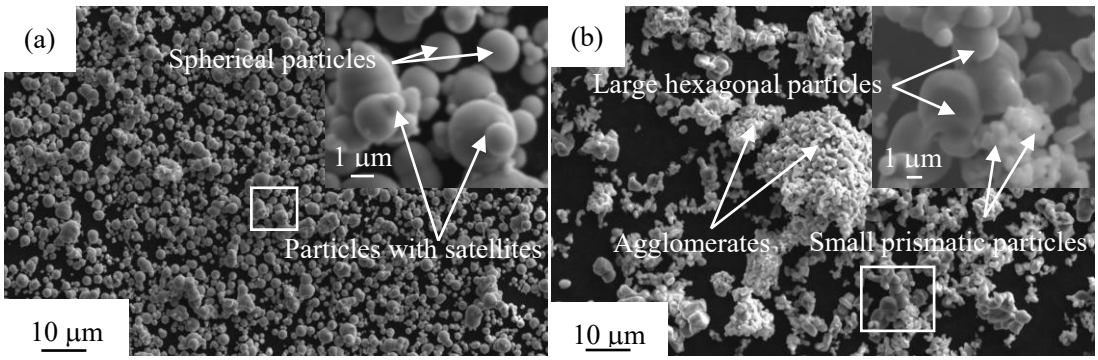

Fig. 2.5 SEM images of starting powder: (a) as-received Fe and (b) as-received TiB_2.

In this chapter, eight experiments were conducted to investigate the optimized multimodal ball size distributions, as shown in Table 2.1. Three kinds of balls with diameters of 9.5, 5, 2 mm were selected as mixing balls based on section 2.2.2. The size of three kinds of balls is reduced successively. Besides, the large size ball (9.5 mm), medium size ball (5 mm), and small size ball (2 mm) were denoted as L, M and S balls, respectively. From No. 1-8, L balls are decreasing while M or S balls are increasing. In addition, No. 1-8 were conducted at rotational speed of 100 rpm which is 62.5% of the critical velocity as introduced above.

No. 1-3 were unqualified because there were sedimentations left on the bottom of milling pots shown in Fig. 2.6(a)(b)(c), which indicated the interactions between balls and powders were insufficient caused by insufficient ball contacts provided by M or S balls. Besides the wear debris of stainless balls, which present as irregular shape, were introduced and thus indicated by white arrows as shown in Fig. 2.6(d)(e)(f). In contrast, there were slight sedimentations left on the bottom of milling pots in No. 4-6 as shown in Fig. 2.7(a)(b)(c). Moreover, the wear debris were also observed as displayed in Fig. 2.7(d)(e)(f), since introduction of wear debris into powder mixtures is inevitable during ball mixing process. With the decrease of L balls and the increase of M or S balls, which correspond to No. 7 and 8, the images of milling pots and SEM images are shown in Fig. 2.8. The inhomogeneous sedimentation of No. 7 and 8 were observed as shown in Fig. 2.8(a)(b). This is attributed to the lack of L balls which are responsible for preventing reagglomeration of powder mixtures as described above. The wear debris were indicated in Fig. 2.8(c)(d). Although slight sedimentation was observed in No. 6, it was seemingly to be more homogeneous than the others. Besides, this slight

sedimentation was partially attributed to the residual slurry.

Table 2.1 Combination of different balls.

No.	Ball size (mm)			Rotational speed (rpm)
	9.5	5	2	
1	150 g			
2	130 g	20 g		
3	130 g		20 g	100
4	120 g	--	30 g	
5	100 g	25 g	25 g	
6	75 g	50 g	25 g	
7	50 g	75 g	25 g	
8	25 g	100 g	25 g	

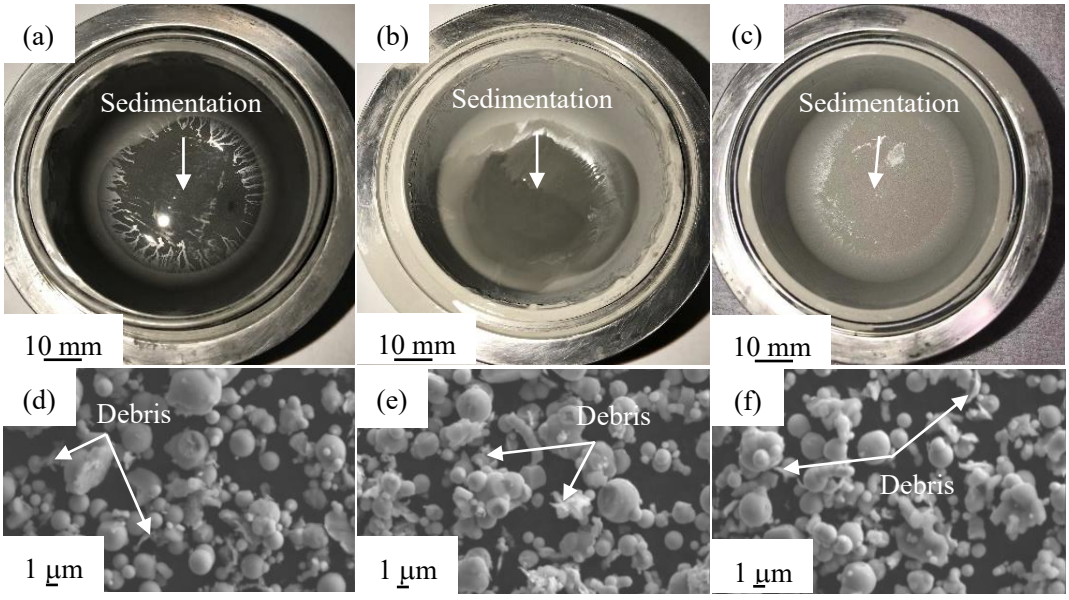

Fig. 2.6 Images of sedimentations in (a)(b)(c) and SEM images of debris in (d)(e)(f) after wet mixing corresponding to No. 1-3.

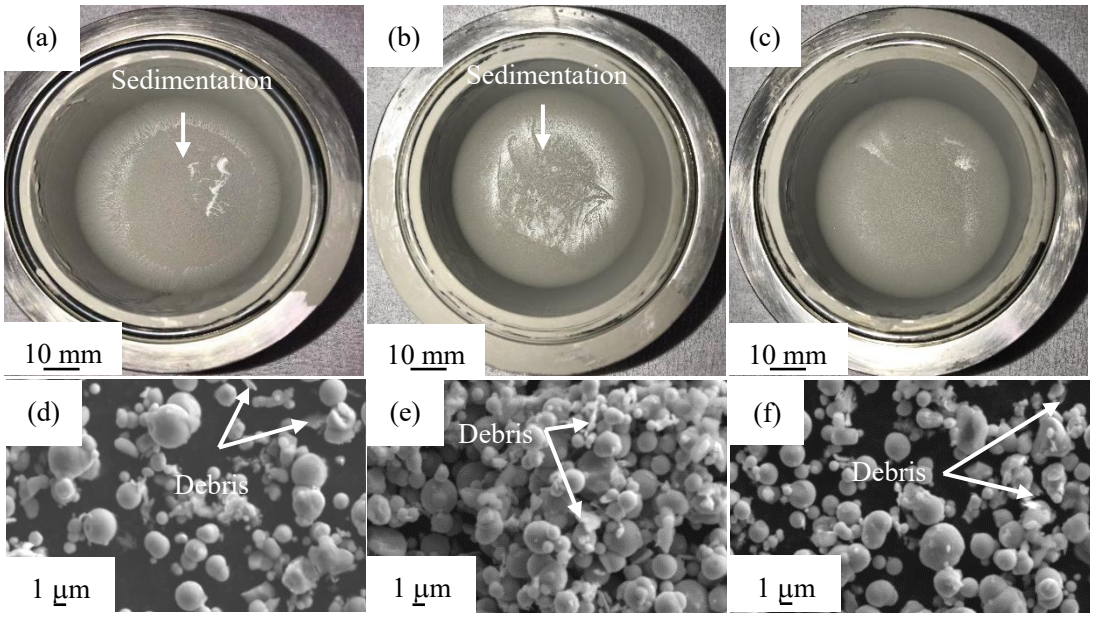

Fig. 2.7 Images of sedimentations in (a)(b)(c) and SEM images of debris in (d)(e)(f) after wet mixing corresponding to No. 4-6.

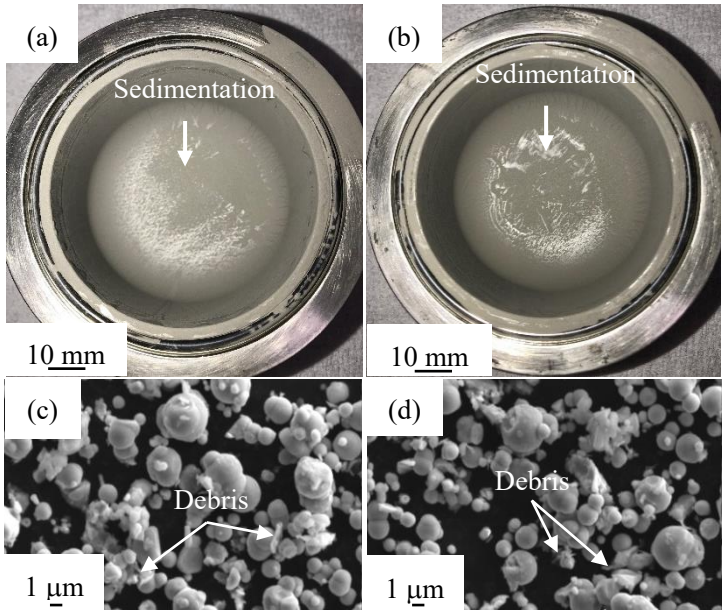

Fig. 2.8 Images of sedimentations in (a)(b) and SEM images of debris in (c)(d) after wet mixing corresponding to No. 7 and 8.

2.3.3 Evaluation of microstructures and $[LND\text{-}2D]_{av}$

Whether there is occurrence of sedimentation on the bottom of milling pots or not is a qualitative criterion to evaluate the mixing effect. In order to quantitatively evaluate the mixing effect, $[LND\text{-}2D]_{av}$ was introduced to evaluate the spatial distribution of TiB_2 in Fe matrix in this study. The powder mixtures of No. 4-8 were obtained by mono-wet mixing and combination of wet/dry mixing, respectively, and then were spark sintered. In order to fully evaluate the spatial distribution of TiB_2 in Fe matrix, the sintering temperature was chosen to be 1173 K which is below the decomposition temperature of TiB_2 in Fe. The SEM images of Fe-20vol.%TiB_2 compacts sintered at 1173 K for 0 s corresponding to No. 4-8 are shown in Fig. 2.9. Fig. 2.9(a)-(e) and (f)-(j) correspond to mono-wet mixing and wet/dry mixing, respectively. The TiB_2 particles clustering were marked by white circles in all images. From Fig. 2.9(a)-(e), that is, with the decrease of L balls and the increase of M or S balls, the TiB_2 particles clustering was relieved first then became deteriorative. Fig. 2.9(c)(d), which corresponded to No. 6 and 7, showed better spatial distribution of TiB_2 in Fe matrix than the others. Besides, the TiB_2 particles clustering was obviously relieved when the wet/dry mixing was applied as shown in Fig. 2.9(f)-(j).

The SEM images of Fe-20vol.%TiB_2 were processed, and $[LND\text{-}2D]_{av}$ of each compacts were obtained as shown in Fig. 2.10. From No. 4 to No. 8, the trend of $[LND\text{-}2D]_{av}$ curves decreased first and then increased, showing the minimum at No. 6. That is to say, the spatial distribution of TiB_2 in Fe matrix of No. 6 was more homogenous than that of the others. When the powder mixtures were subject to wet/dry mixing as shown in the dashed curve, the TiB_2 particles clustering was less deteriorated compared with those applied to mono-wet mixing. Besides, what is worth noticing is that over-added M or S balls did not improve the mixing efficiency, which corresponded to the case of No. 8 as shown in Fig. 2.9(e)(j), since over-added M or S balls initiated numerous but weak contacts which are difficult to break or deagglomerate the agglomerates and to prevent reagglomeration. The variation of $[LND\text{-}2D]_{av}$ curves coincided well with the microstructures shown in Fig. 2.9.

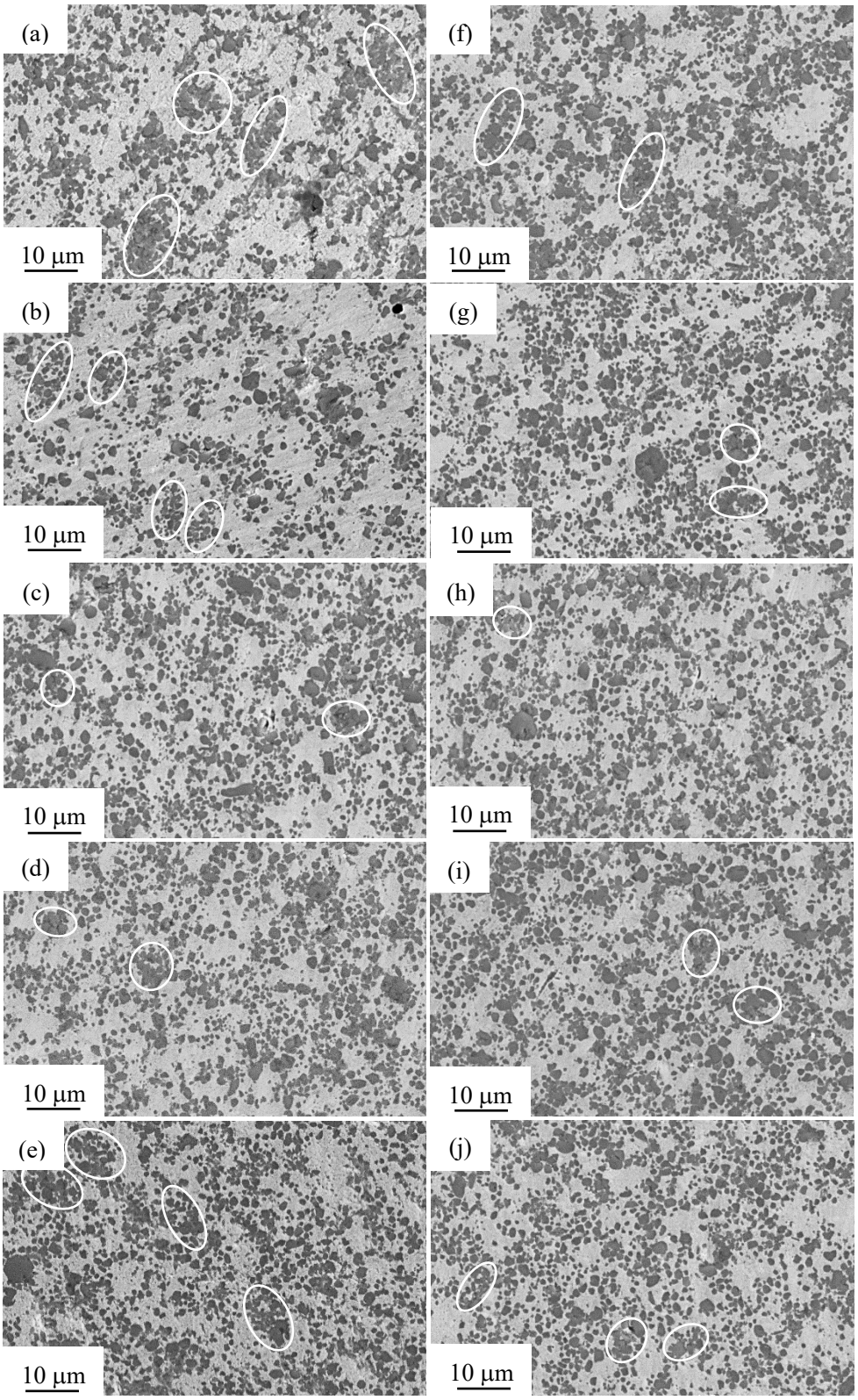

Fig. 2.9 SEM images of Fe-20vol.% TiB_2 compacts sintered at 1173 K for 0 s corresponding to No. 4-8, and (a)-(e) obtained from mono-wet mixing and (f)-(j) obtained from wet/dry mixing.

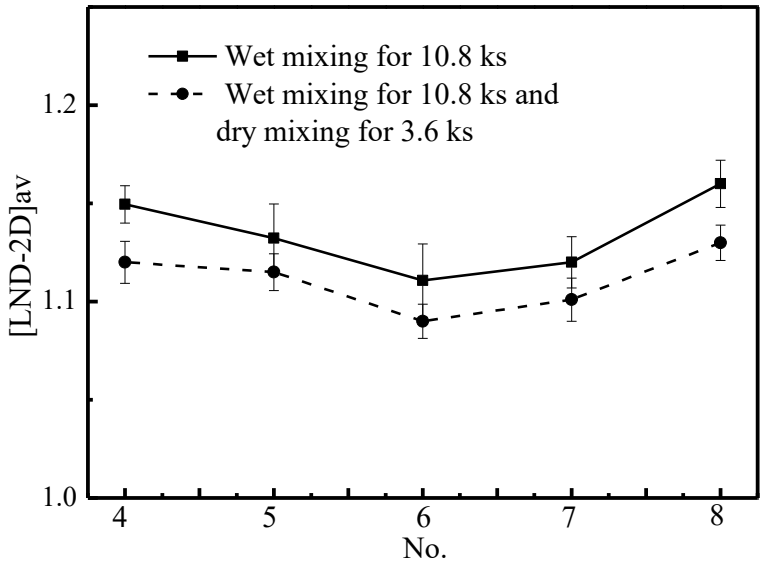

Fig. 2.10 $[LN2D]_{av}$ of Fe-20%TiB_2 compacts sintered at 1173 for 0 s corresponding to No. 4-8.

2.3.4 Evaluation of error bar of Vickers hardness

Based on the data obtained from above, No. 5-7 were screened out to be further tested in terms of comparing the error bar of Vickers hardness of each compact. Considering the objective of fabricating Fe-TiB_2 composites with both high TC and hardness, the powder mixtures of No. 5-7 mixed by wet/dry mixing were sintered at 1373 K for 0.3 ks. The microstructures of sintered compacts are shown in Fig. 2.11. The decomposition of TiB_2 occurred at 1373 K as shown in Fig. Fig. 2.11(a)(b)(c). TC and Vickers hardness of compact were obtained as shown in Fig. 2.12. The values of Vickers hardness and TC of three compacts were at the same scale, however, the error bar of Vickers hardness in No. 6 showed the lowest of 5, while it was 13 for No. 5 and 7 for No. 7. This indicted that No. 6 exhibited the most homogenous microstructure among No. 5-7.

It was concluded that decreasing L balls and increasing M or S balls moderately can improved spatial distribution as proved by the microstructures, $[LND-2D]_{av}$ and error bar of Vickers hardness. However, the spatial distribution could also be weakened if the L balls were over-reduced. As a consequence, the ratio of each ball should be maintained at a reasonable range, where L balls provide sufficient energy for the deagglomeration, and M and S balls supply numerous microprocesses leading to an excellent distribution of TiB_2 in Fe.

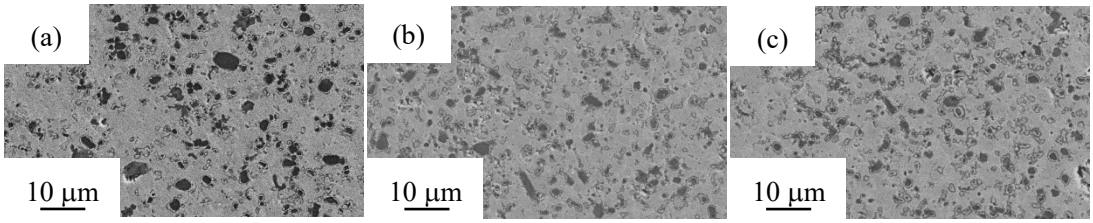

Fig. 2.11 SEM images of Fe-20vol.% TiB_2 compacts sintered at 1373 K for 0.3 ks corresponding to No. 5-7.

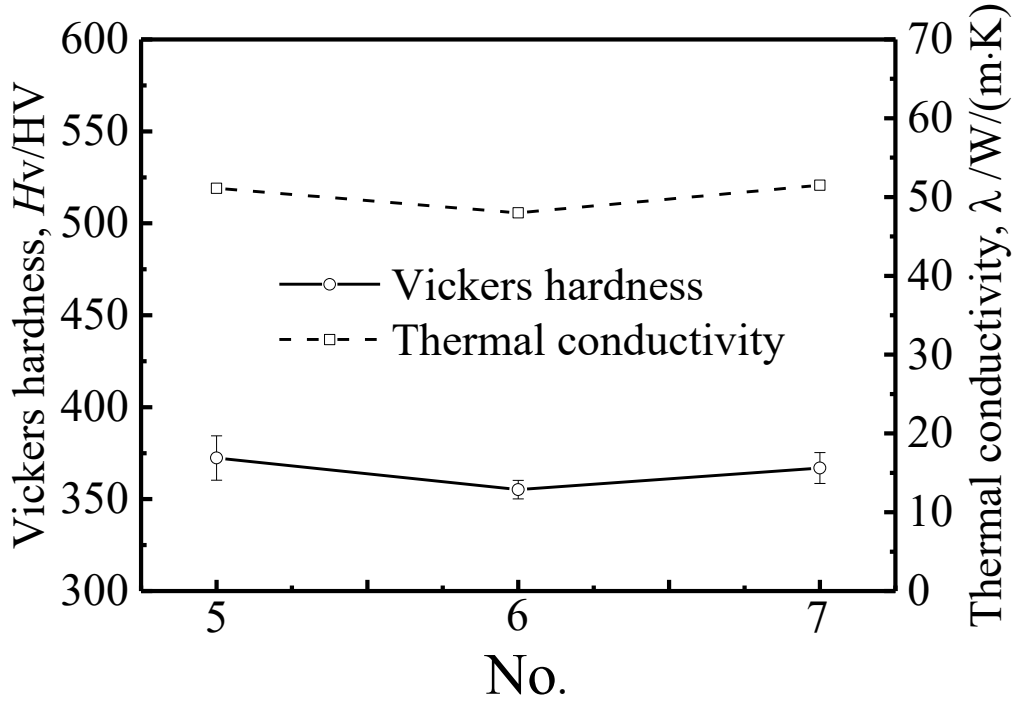

Fig. 2.12 Vickers hardness and TC of Fe-20%TiB_2 compacts corresponding to No. 5-7.

2.3.5 Comparison between different rotational speed

The rotational speed was also investigated in this chapter. According to the abovementioned experiments, No. 6 and 7 were selected and applied to 150 rpm, which were referred as No. 9 and 10. To further explore the effect of rotational speed on the homogeneity of sintered compacts, the SEM images of powder mixtures after wet mixing were obtained as shown in Fig. 2.13. The weight increased dramatically after wet mixing, which meant the wear debris were extensively introduced into powder mixtures as indicated in SEM images in Fig. In addition, the TC and Vickers hardness were measured and displayed in Fig. 2.14. Especially, the TC of No. 9 and 10 was much

lower than that of No. 6 and 7. This could be attributed to the introduction of large number of wear debris as proved by weight increase after wet mixing and SEM images. Besides, the error bars of No. 9 and 10 were larger than that of No. 6 and 7. As introduced in section 2.2.1, rotation of 150 rpm which is 93.7% of the critical velocity will produce the ball motion pattern close the rolling, and therefore lead to less interactions between balls and slurry as well as compromised mixing. And thus, No. 9 and 10 were not suitable for mixing.

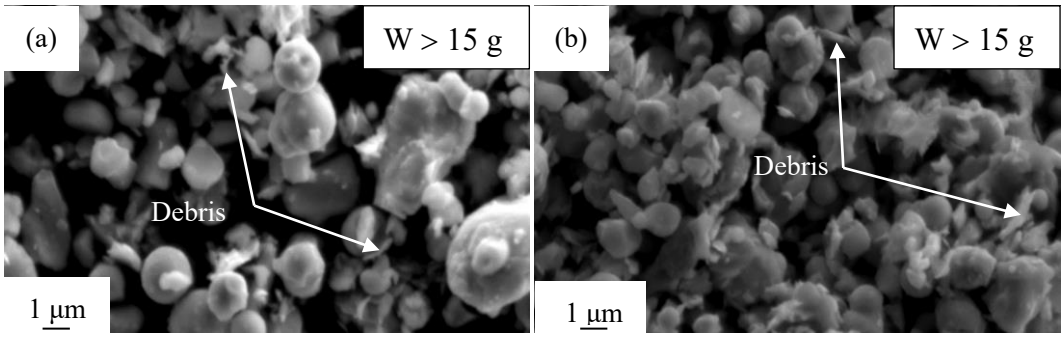

Fig. 2.13 SEM images of power mixtures of No. 9 and 10.

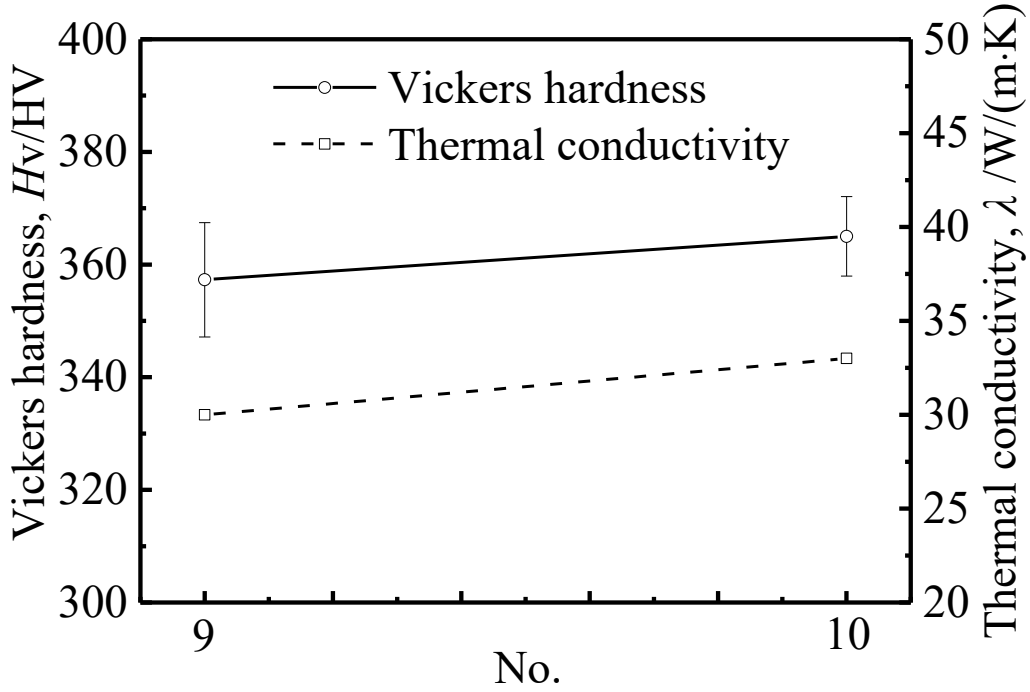

Fig. 2.14 Vickers hardness and TC of Fe-20%TiB_2 compacts corresponding to No. 9 and 10.

2.4 Summary

(1) Wet/dry mixing provided better spatial distribution than mono-wet mixing.

(2) Decreasing L balls and increasing M or S balls moderately could improve spatial distribution, as $[LDN\text{-}2D]_{av}$ and error bar was decreased. However, the spatial distribution could also be weakened if the L balls were over-reduced, as over-added M or S balls provide numerous but weak contacts which are difficult to break or deagglomerate particles. Therefore, No. 6 was determined as the optimized mixing parameter for Fe-TiB_2 powder mixtures among the designed group.

(3) Increasing the rotational speed to 150 rpm deteriorated the spatial distribution by involving wear debris into powder mixtures and compromising interactions between balls and slurry.

Reference

1) J.J. McCarthy, T. Shinbrot, G. Metcalfe, J.E. Wolf and J.M. Ottino: AIChE Journal 42 (12) (1996) 3351-3363.
2) D. Zhang, K. Sugio, K. Sakai, H. Fukushima and O. Yanagisawa:Mater. Trans. 48 (2) (2007) 171-177.
3) D. Zhang, K. Sugio, K. Sakai, H. Fukushima and O. Yanagisawa: Mater. Trans. 49 (3) (2008) 661-670.
4) D. Zhang, K. Sugio, K. Sakai, H. Fukushima and O. Yanagisawa: Mater. Trans. 49 (3) (2008) 671-680.
5) J.H. Song and J.R.G. Evans: J. Mater. Sci. Lett. 13 (22) (1994) 1642-1644.
6) F.F. Lange: J. Am. Ceram. Soc.72 (1) (1989) 3–15.
7) F.L. Zhang, C.Y. Wang and M. Zhu: Scr. Mater. 49 (11) (2003) 1123-1128.
8) F.L. Zhang, M. Zhu and C.Y. Wang: Int. J. Refract. Hard Met. 26 (4) (2008) 329-333.
9) M. Chmielewski, D. Kaliński, K. Pietrzak and W. Włosiński: Arch. Metall. Mater. 55 (2) (2010) 579-585.
10) C. Suryanarayana, E. Ivanov and V.V. Boldyrev: Mater. Sci. Eng. A 304 (2001) 151-158.
11) H. Shin, S. Lee, H.S. Jung and J.B. Kim: Ceram. Int. 39 (8) (2013) 8963-8968.
12) S.M. Salili, A. Ataie and Z. Sadighi: In AIP Conference Proceedings 1400 (1) (2011) 127-130.
13) C.N. Chen, Y.L. Chen and W.J. Tseng: J. Mater. Process. Tech. 190 (1-3) (2007) 61-64.
14) H. Ferkel, R.J. Hellmig: Nanostruct. Mater. 11 (5) (1999) 617–622.
15) J. Fruhstorfer, S. Schafföner and C.G. Aneziris: Ceram. Int. 40 (9) (2014) 15293-15302.
16) Z.F. Xu: Doctoral thesis. Hiroshima University. 2010.
17) C.F. Burmeister and A. Kwade: Chem. Soc. Rev. 42 (18) (2013) 7660-7667.
18) F.A.L. Dullien, Porous Media, Fluid Transport and Pore Structure, 2nded., Academic Press Inc., New York,1992.

Chapter 3

Fabrication of Fe-30vol.%TiB_2 composites with both high TC and hardness

3.1 Introduction

TiB_2 is now considered as a promising reinforcements candidate for steels because of its high microhardness, excellent Young's modules[1)] and good transverse rupture strength[2)]. In addition, TiB_2 is relatively stable in liquid Fe[3-5)] and the solubility of Fe in TiB_2 is lower than 4%[6)]. Besides, liquid Fe can well wet TiB_2[7,8)]. More importantly, Fe-TiB_2 composites fabricated by powder metallurgy (PM) and casting both show good interfacial cohesion between the Fe matrix and TiB_2 reinforcements[9-13)]. Of most reported Fe-TiB_2 composites, they are expected to apply to high modulus steels[6,11,14-24)] and wear-resistance parts[25-30)]. However, limited literatures reported about the application on hot work tools (HWTs).[31)]

In fields of HWTs, both good wear resistance and high TC are necessary, since improving wear resistance can prolong the service time of HWTs and increasing TC can bring an order of magnitude increase in thermal fatigue resistance[32)] and accelerate heat transfer from workpieces to cooling system. And thus, the higher production efficiency can be expected because the cycle time of forming is reduced. Moreover, TiB_2 is endowed with high TC of 96 W/(m·K)[33)], while it is also reported of 65-120 W/(m·K)[1)]. Therefore, TiB_2 reinforced Fe matrix composites are considered attractive materials for the usage not only in high modules steels and wear-resistance parts but also in HWTs due to the improved wear resistance and thermal conductivity.

In Fe-TiB_2 system, Fe_2B and TiC are commonly observed resultants resulted from the reaction occurring between Fe and TiB_2. The reaction mechanism remains unclear. Impurities of C and O involved from starting powders are considered responsible for the decomposition of TiB_2 in Fe, since impurities can consume Ti by formation of TiC or TiO_2, which lead to the excess B. Then B atoms react with Fe, giving rise to the formation of Fe_2B[34)]. However, in the absence of C and O, formation of Fe_2B is still reported in literatures[28,35)]. The reaction mechanism of Fe and TiB_2 is of great importance with regard to the synthesis of Fe-TiB_2 composites, and hence it will be discussed in this study. In most cases, formation of Fe_2B is undesirable because it may deteriorate toughness of materials, however, wear resistance of composites can be enhanced significantly[36,37)]. As for the formation of TiC, this is also, to some extent, beneficial to reinforce the matrix by TiC-TiB_2 dual phase[38,39)]. As orientation

relationship (OR) exists both in Fe-TiC ($(101)_{Fe}$ // $(1\bar{1}1)_{TiC}$)[6,11] and TiC-TiB_2 ($\{111\}_{TiC}$ // $(0001)_{TiB_2}$)[40], which can contribute to a good interfacial cohesion between the interfaces.

Various synthesis routes have been put into place to fabricate Fe-TiB_2 composites [12,19,26-29]. Casting is a conventional and efficient route which can guarantee a clean interface, allow the tailoring of added elements as well as capable of casting large size ingots. However, there are two prominent issues which are clustering of TiB_2 reinforcements in Fe matrix[12] and density-induced floatation of the primary TiB_2 particles[19]. Apparently, more elaborate process should be taken into consideration in order to obtain a homogenously TiB_2-distributed Fe matrix composites by casting route. Other processes involving in in-situ chemical reactions, most of them is self-propagating high temperature synthesis which enables a clean interface and allow adjustment of fraction of reinforcements. Nevertheless, the salient issues are difficult to control the process, aggregate of reinforcements and high porosity of resultants[26-29]. The stereotyped disadvantages of PM process include the limitations to small parts and unclean interface between the matrix and the reinforcements. However, spark sintering technique, one novel method of PM, has been developed to be a high-efficiency sintering technique in recent decades. It can be applied to synthesizing a wide range of materials, such as metals[41], alloys[42], ceramics[43] and composites[44]. Due to the discharges, the particle surface is activated and purified[45-47], and a self-heating phenomenon is generated between the particles. As a result, heat-transfer and mass-transfer can be completed instantaneously. Therefore, spark sintering technique can be applied to sinter metal matrix composites quickly to the full density at a relatively low temperature. In addition, a homogenous microstructure can be obtained if a suitable mixing process is applied.

The objective of this study is to investigate the microstructures of Fe-TiB_2 composites sintered by spark sintering and to fabricate the Fe-TiB_2 composites with both high TC and hardness for the possibility of HWTs applications.

3.2 Materials and Methods

3.2.1 Materials and synthesis

As-received TiB_2 (99.9%, Pure Chemical Co., Ltd. Japan) and pure Fe (99.9%, Sanwa Metal Industry Co., Ltd. Japan) powders with size of 2~3 μm and 3~5 μm, respectively, were used as starting powders. The wet mixing process was utilized to mix the 30vol.%TiB_2 and 70vol.%Fe powders. TiB_2 and Fe powders of total amount of 15 g were placed in a stainless-steel jar with a volume of 250 cm^3 and then 25 mL ethanol was added as a wet mixing agent. Hereafter, the jars were vacuumed for 0.3 ks. Stainless-steel balls with a diameter of 2~10 mm was used for mixing. The weight ratio of balls to powders was 10:1. Mixing process was conducted in a planetary ball mill (Pulverisette-5, Fritsch, Germany) at 100 rpm for 10.8 ks. Slurry of powder mixtures were dried in a fume hood and then dry mixed for 3.6 ks. Powder mixtures were loaded in a graphite die and consolidated by spark sintering (CS12567, NSK. Ltd. Chūgoku Branch, Japan) technique. All spark sintering experiments were carried out at an applied pressure of 50 MPa and a vacuum condition ($<10^{-2}$ Pa). The die temperature was monitored using R type thermocouple inserted into the hole of die. Sintering temperature was determined at 1373 K because it was the optimized temperature based on previous work. Therefore, samples were sintered at 1373 K, heating rate of 100 K/min, and holding different times (0, 0.3, 0.6, 1.8 and 3.6 ks). Finally, compacts with height of 10 mm and diameter of 10 mm were obtained.

3.2.2 Characterizations of starting powders and sintered compacts

Morphology of powders and microstructure of sintered compacts were observed by electron probe micron analyzer (EPMA, JXA-8900, JEOL, Japan). Phase compositions of sintered compacts were characterized by X-ray diffraction (XRD, D/max-2500PC, Rigaku, Japan) with Cu Kα radiation (L=0.15418 nm, 40 kV, 100 mA). Scanning transmission electron microscope (STEM, Talos F200X, Thermo Fisher Scientific, USA), high-resolution TEM (HRTEM) and energy disperse spectroscopy (EDS) were performed at 200 kV. High angle annular dark field (HAADF) images and bright field (BF) images were taken at angle of 59-200 mrad and 9 mrad, respectively. Vickers hardness was obtained by Vickers hardness tester (FV-110, Future-Tech Corp., Japan)

at a load of 5 kg and a dwelling time of 10 s. The thermal diffusivities (α) of the samples (Φ10×1 mm) were measured at room temperature by a laser flash thermal constant measuring apparatus (Thermal conductivity-9000h, Ulvac-riko, Japan). The specific heat capacities (C_p) of the samples (Φ4×0.5 mm) were measured at room temperature by differential scanning calorimeter (STA449C, Netzsch-Gerätebau GmbH, Germany). Densities (ρ) of sintered compacts were acquired by Archimedes' principle. Thermal conductivities (λ) of sintered compacts were calculated according to the equation (1). Image analysis was adopted to roughly calculate the area fraction of each phase in sintered compacts. Different phases were dyed in different colors and then the area fraction of each phase could be calculated by image analysis.

$$\lambda=\alpha\cdot C_p\cdot\rho \tag{3.1}$$

3.3 Results and discussion

3.3.1 Effect of sintering temperatures on fabrication of Fe-TiB_2 compacts

3.3.1.1 Morphologies of starting powders and phase identification

Morphologies of starting powers are shown in Fig. 3.1. As-received pure Fe particles were spherical with size of 3~5 μm as shown in Fig. 3.1(a). As-received TiB_2 particles basically presented as prismatic particles, such as a hexagonal shape as shown in Fig. 3.1(b). Large hexagonal TiB_2 particles with size of about 2~3 μm corresponded to well-grown TiB_2. In contrast, some kinds of small TiB_2 were prismatic particles with size of approximate 500 nm. Powder mixtures of Fe–30vol.% TiB_2 after mixing was shown in Fig. 3.1(c), and the magnified image of the area marked by white square in (c) was shown in Fig. 3.1(d) in which TiB_2 and Fe were indicated according to the above described characteristics.

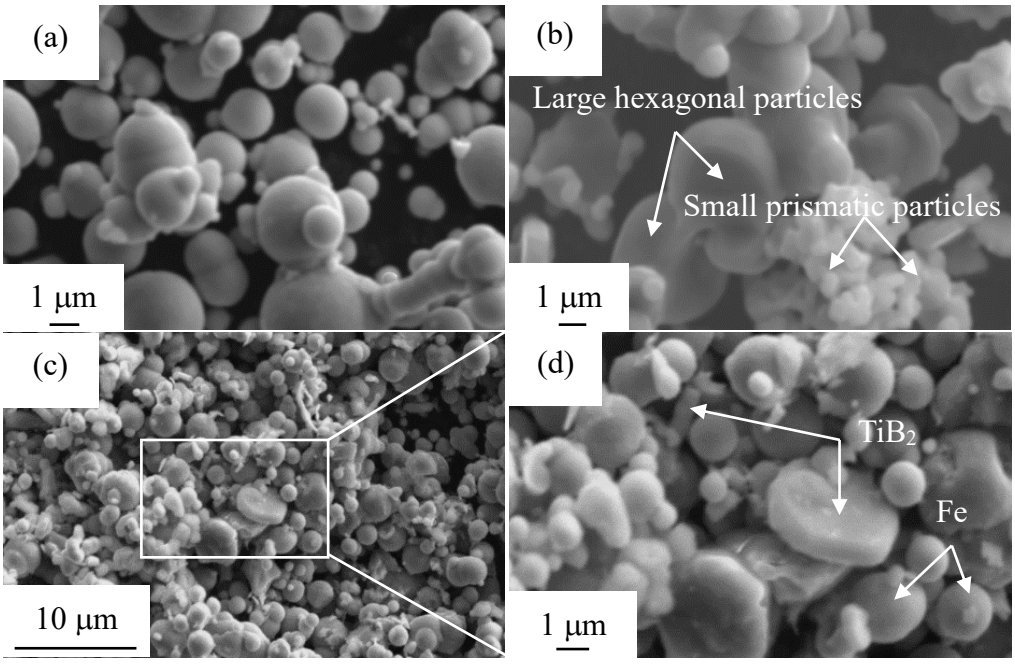

Fig. 3.1 SEM images showing as received (a) Fe and (b) TiB_2 powders, (c) powder mixtures of Fe–30vol.% TiB_2 after mixing, and (d) high magnified image corresponding to the area marked by white square in (c).

3.3.1.2 Microstructures of Fe-TiB_2 compacts

Figure. 3.2 shows the XRD patterns of Fe-30vol.% TiB_2 compacts sintered over the temperature range of 1273-1423 K for 0 s. The compact sintered at 1273 K consists of TiB_2 and α-Fe phases, while they were TiB_2, α-Fe, TiC, and Fe_2B when sintering temperature was at 1323 K and above.

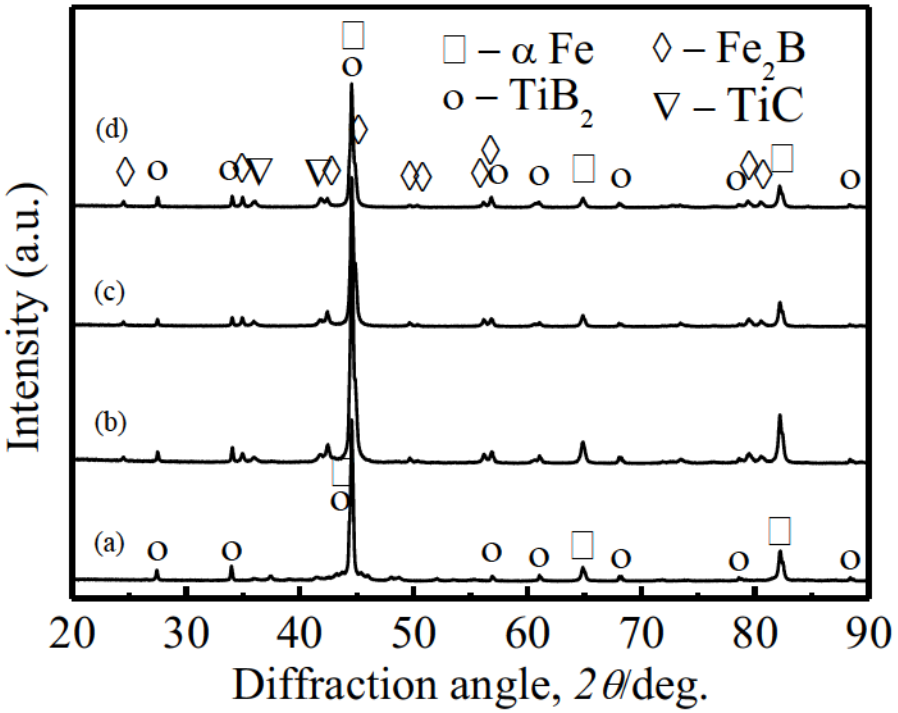

Fig. 3.2 XRD patterns of Fe-30vol.% TiB_2 compacts sintered at (a) 1273, (b) 1323, (c) 1373 and (d) 1423 K for 0 s.

The BSE image of the composite sintered at 1373 K is shown in Fig. 3.3. Point analysis was taken on this image to clarify the phases distribution in sintered composites. Results of point analysis are displayed in Table. 3.1. Points were taken on circle-like area which are about 300 nm in width, black area, gray area and light area, respectively, as marked. The four areas are confirmed as TiC, TiB_2, Fe_2B and Fe or Fe solid solution with small amount of Ti coupled with prior analysis results from XRD pattern as well as atom ratio which slightly deviate from the nominal stoichiometry due to not being calibrated with standard samples. The carbon was introduced from the graphite dies and punches during sintering process.

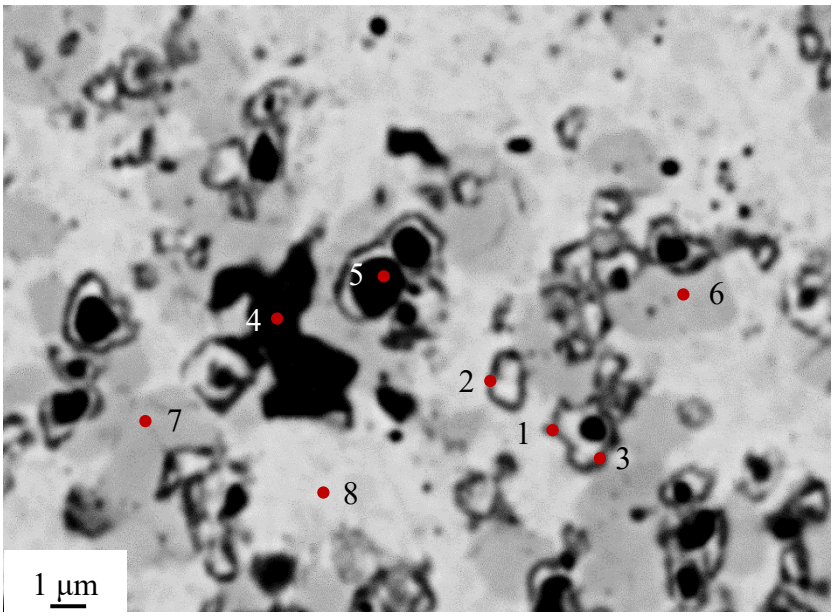

Fig. 3.3 BSE image of Fe-30vol.% TiB_2 compact sintered at 1373 K for 0 s.

Table 3.1 Point analysis of points 1 to 8 in Fig. 3.

Points	Compositions (at%)			
	Fe	Ti	B	C
1	68	18.8	1. 2.3	10.9
2	92.8	3.6	0	3.6
3	61.6	20	5.5	12.9
4	7.9	27.7	61.7	2.7
5	8.5	32.2	56.5	2.8
6	66.7	8.7	21.8	2.8
7	68.3	1.9	29.2	0.6
8	96.8	2.2	0	1

Microstructures of sintered compacts are revealed in Fig. 3.4. Fig. 3.4 (a)-(d) are SEM images of compacts sintered at different temperatures. Pores were observed between the TiB_2 particles over the whole sintering temperature range. It is ascribed to the aggregates of TiB_2 particles on one hand and insufficient sintering on the other hand. Phases distribution in sintered compacts are manifested in the corresponding BSE images as indicated in Fig. 3.4 (e)-(h). There was no observation of Fe_2B and TiC in the composite sintered at 1273 K, which coincides well with the result from XRD pattern. Decomposition of TiB_2 intensified with temperature increasing, as more Ti atoms diffused into Fe at high temperatures according to the Ti-Fe binary phase diagram. The released B atoms derived from the decomposition of TiB_2 had nowhere to go but to react with Fe, resulting in the formation of Fe_2B phase. Furthermore, the morphology of TiB_2 was observed in Fig. 3.4 (h) in compact sintered at 1423 K presented as distinctly round-cornered shape compared with that of those sintered at lower temperatures. And there was a considerable amount of TiC which, however, was only discernible in Fig. 3.4 (f)(g). Generally, TiC appeared as either circle–like or rim–core shape structure with a residual TiB_2 core. A eutectic reaction, $Fe + Fe_2B \rightarrow Fe$ (l), occurs at 1423 K. Liquid Fe can contain much more amount of C atoms than the maximum amount of 2.08 wt.% C in γ-Fe in accordance with the Fe-C binary phase diagram, accounting for the considerable formation of TiC at 1423 K.

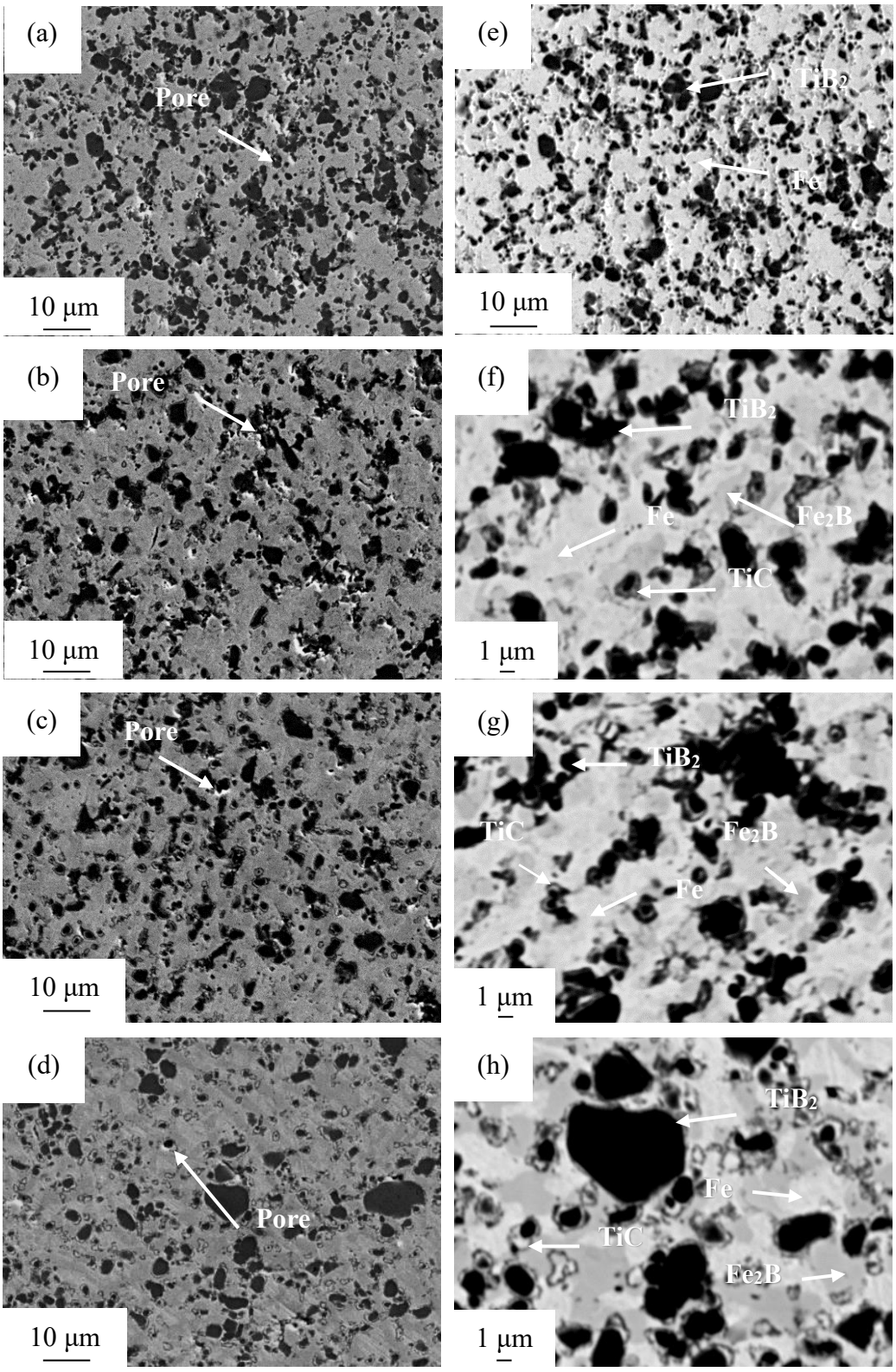

Fig. 3.4 SEM and BSE images of Fe-30vol.% TiB_2 compacts sintered over the temperature range of 1273 to 1423 K holding 0 s: (a) (e)1273 K, (b) (f)1323 K, (c) (g)1373 K, and (d) (h) 1423 K.

3.3.1.3 TC and hardness of Fe-TiB_2 compacts

Figure. 3.5 shows the density and porosity as the function of sintering temperatures. Both density and relative density increased when the temperature rose. Fig. 3.6 illustrates the Vickers hardness and TC of sintered compacts at different temperatures. With the increase of temperatures, the Vickers hardness increased due to gradually enhanced interfacial bonding between particles and the formation of Fe_2B. what was worth mentioning was that TiC precipitated and dispersed in the matrix, which is also responsible for improving the hardness of composites, especially for compact sintered at 1423 K, reaching the value of 742 HV. However, relative density of sintered composites still needs to be further improved. Nevertheless, the TC declined to the minimum at 1323 K of 38 W/(m·K) and then rose to 48 W/(m·K) at 1423 K. Defects and interface thermal resistance play important role on TC. Defects, mainly attributed to sintering pores in this case as shown in Fig. 3.4 marked by white arrow, was considered affecting the TC most, since the sintering pores decrease the mean free length of the path for electron and phonon. Phase composition of the composite sintered at 1273 K was α-Fe and TiB_2 which were both high TC phases. This might be attributed to relatively high TC of the compact sintered at 1273 K even with the highest porosity. As temperature increased, porosity was decreased, leading to the improvement of TC, while that of Fe_2B, a relatively low TC phase, was increased which gave rise to the increase of interface thermal resistance. In this case, eliminating pore was a more effective way to improve TC, which contributes to the increase of TC from 1323–1423 K. Besides, poorly bonded interface where contained some lattice distortions or compounds created by internal reactions between particles also influence TC, since the lattice distortions cause electron or phonon scattering.

The effect of sintering temperatures on microstructure, TC and Vickers hardness were investigated. However, relative density is not high enough at lower sintering temperature and liquid phase will form at high temperature. And hence, sintering temperature of 1373 K will be chosen as the optimized temperature for Fe-30vol.% TiB_2 and different holding time will be discussed in order to obtain compacts with both high TC and hardness in the following section.

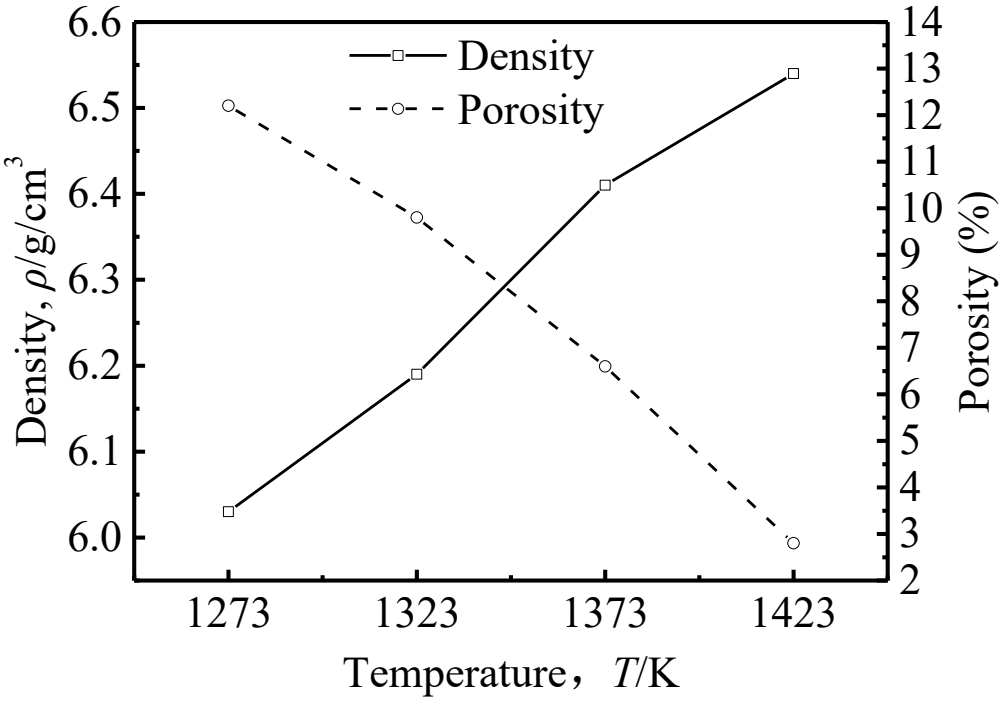

Fig. 3.5 Density and Porosity of Fe-30vol.%TiB_2 compacts sintered from 1273 to 1423 K for 0 s.

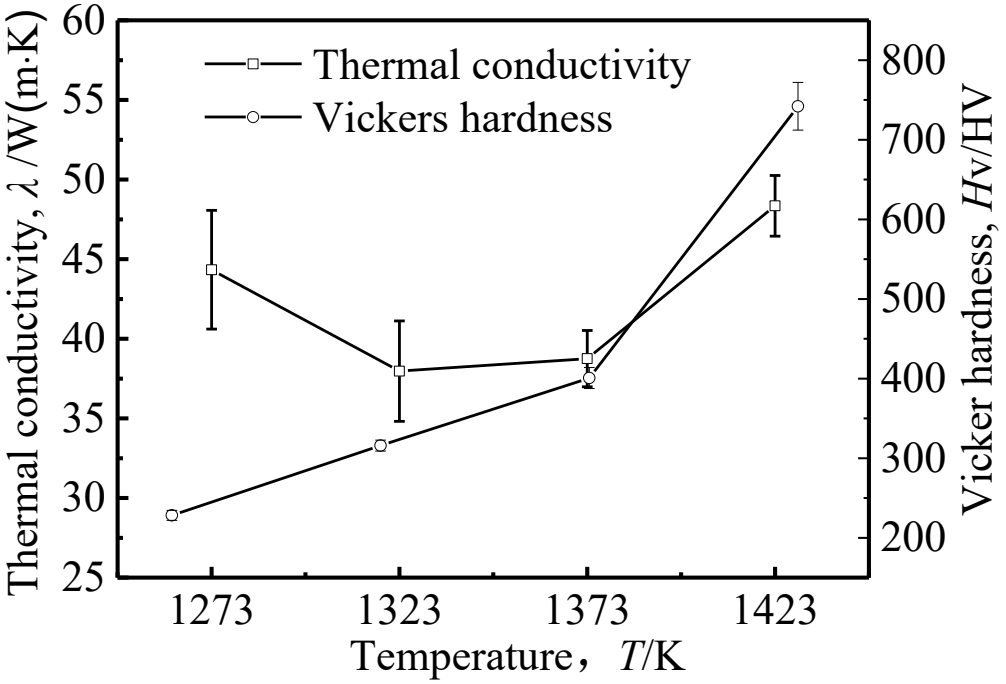

Fig. 3.6 TC and Vickers hardness of Fe-30vol.% TiB_2 compacts sintered from 1273 to 1423 K for 0 s.

3.3.2 Effect of holding time on fabrication of Fe-TiB_2 compacts

3.3.2.1 Microstructures of Fe-TiB_2 compacts

XRD patterns of Fe-30vol.% TiB_2 compacts sintered at 1373 K with different holding times are revealed in Fig. 3.7. Except the original phases of Fe and TiB_2, newly formed phases of Fe_2B and TiC were also found in all sintered compacts due to the reaction between Fe and TiB_2.

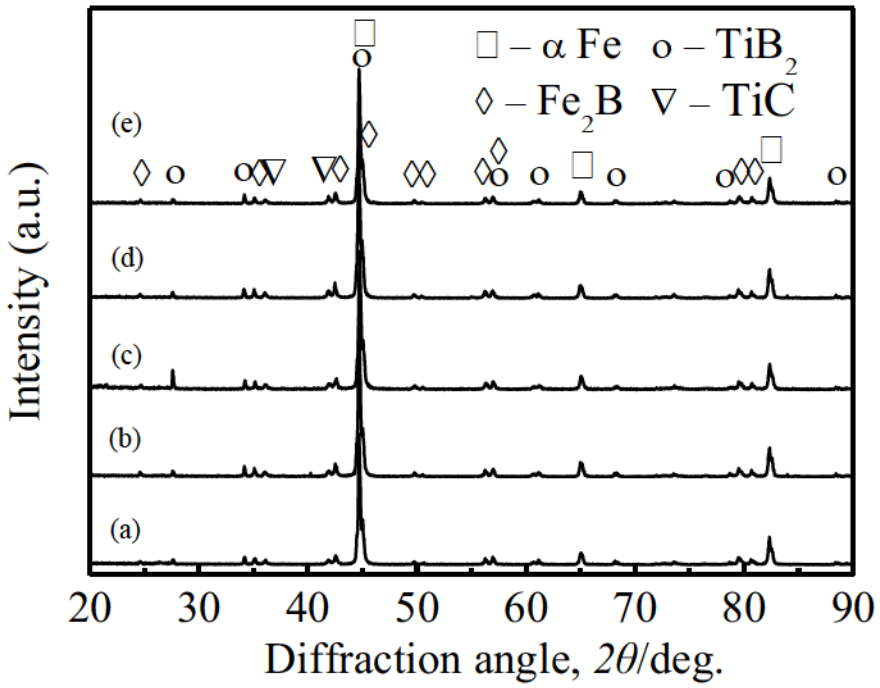

Fig. 3.7 XRD patterns of Fe-30vol.%TiB_2 compacts sintered at 1373 K for (a) 0, (b) 0.3, (c) 0.6, (d) 1.8, and (e) 3.6 ks, respectively.

The typical back scatter electron (BSE) images of compacts sintered for 0, 0.6 and 3.6 ks are shown in Fig. 3.8. According to point analysis in our previous work[49], black areas, gray areas, light areas and circle-like areas corresponded to TiB_2, Fe_2B, Fe (or Fe solid solution with about 3at. %Ti) and TiC, respectively. This result coincided well with that from XRD patterns (shown in Fig. 3.7). TiB_2 particles were basically well-dispersed in matrix. Fe_2B appeared to be irregular morphology and was distributed throughout the whole compacts. TiC particles displayed surrounding TiB_2 particle. Nevertheless, the areas between TiC circles and TiB_2 was still yet to know but will be

revealed in the subsequent STEM images. The area fraction of Fe_2B increased with extending holding time, in contrast, that of Fe decreased because of the consumption of Fe by B atoms, as it could be appreciably distinguished on BSE images. In order to quantitatively obtain the fraction of each phase, the area fraction of each phase in all sintered compacts was roughly measured by image analysis as shown in Fig. 3.9(a). With the increase of holding time, the area fractions of TiB_2 (24.4%-19.0%) and Fe (39.4%-30.0%) were decreasing while that of Fe_2B (29.6%-42.0%) and TiC (6.6%-9.0%) were increasing as the reaction deepened with the increase of holding time. As shown in Fig 3.9(b), the relative density was significantly improved from 0-0.6 ks, while it varied slightly from 0.6-3.6 ks. The improvement of relative density was mainly due to the elimination of sintering pores with the increase of holding time. The variation trend of relative density could be interpreted that holding time of 0.6 ks was effective to remove the most pores during sintering.

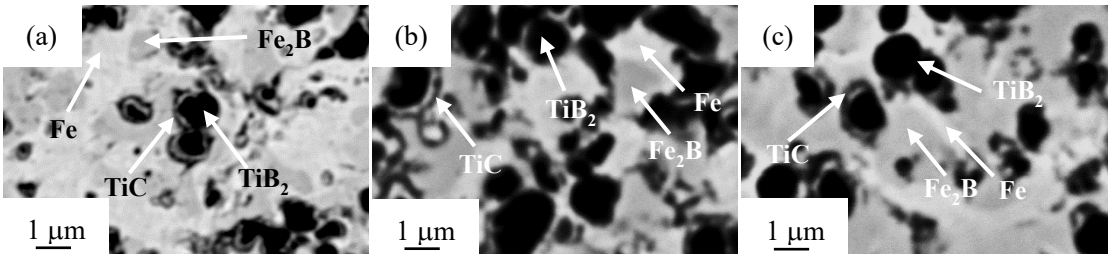

Fig. 3.8 Typical BSE images of Fe-30vol.%TiB_2 compacts sintered at 1373 K for different times: (a) 0, (b) 0.6, and (c) 3.6 ks, respectively.

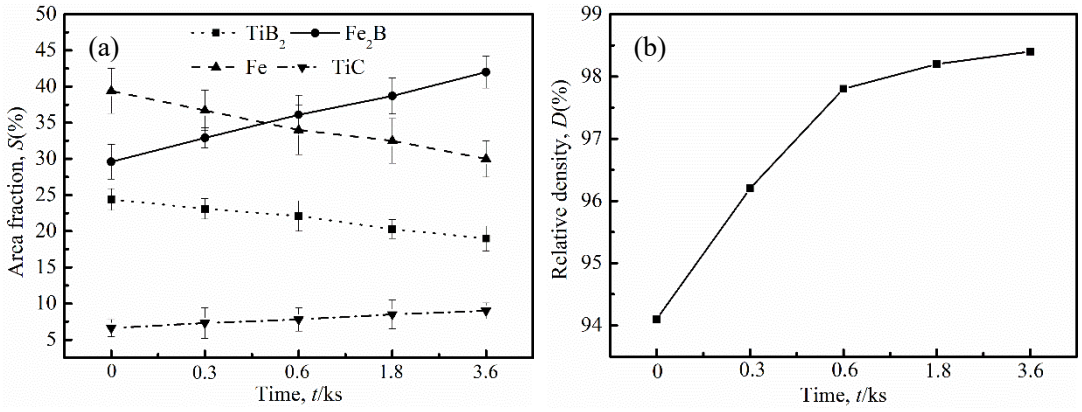

Fig. 3.9 Area fractions of each phase in (a) and relative density in (b) of Fe-30vol.%TiB_2 compacts sintered at 1373 K for 0, 0.3, 0.6, 1.8 and 3.6 ks, respectively.

HAADF images and corresponding mapping analysis images of each element provided a better observation of phases distribution. Fig. 3.10 corresponds to the compact sintered at 1373 K holding 0 ks. Fig. 3.10(a)(b) are HAADF images and Fig. 3.10 (b) is the high magnification image corresponding to the marked area in Fig. 3.10 (a). Fig. 3.10(c)(d)(e) (f) placed on the right are mapping analysis images of Fe, Ti, B and C, which corresponds to Fig. 3.10(a). Coupled with mapping analysis, TiB_2, Fe_2B, Fe and TiC were indicated in Fig. 3.10(a)(b). It was noticeable that the areas, mentioned in Fig. 3.8, connecting TiB_2 and TiC particles were proved to be Fe as marked in Fig. 3.10(b). Namely, TiB_2 was wrapped by a layer of Fe after sintering. This phenomenon will be interpreted in the following section of reaction mechanism between TiB_2 and Fe. The preferred interface planes for TiB_2 particles are prismatic $\{10\bar{1}0\}$ planes and the basal {0001} planes in Fe-TiB_2 composites fabricated by casting[11]. However, in present study, interfaces between Fe and TiB_2 (Fe/TiB_2 interface) were mainly parallel to the prismatic planes of TiB_2 as marked in Fig. 3.10(b). As shown in Fig. 3.10(b), Fe impregnated the triple junctions between Fe and TiB_2 as marked by white circles, and the interfaces of Fe and TiB_2 were well bonded as marked by dashed arrows, which both demonstrated a good cohesion of Fe/TiB_2 interface. Moreover, the good cohesion of Fe/TiB_2 interface will be further characterized at atomic level in Fig. 3.11. TiC grains precipitating along Fe grain boundaries were arrayed in circles as evidenced in Fig. 3.10(a) and it could be further confirmed by the mapping analysis as marked in Fig. 3.10(e)(f).

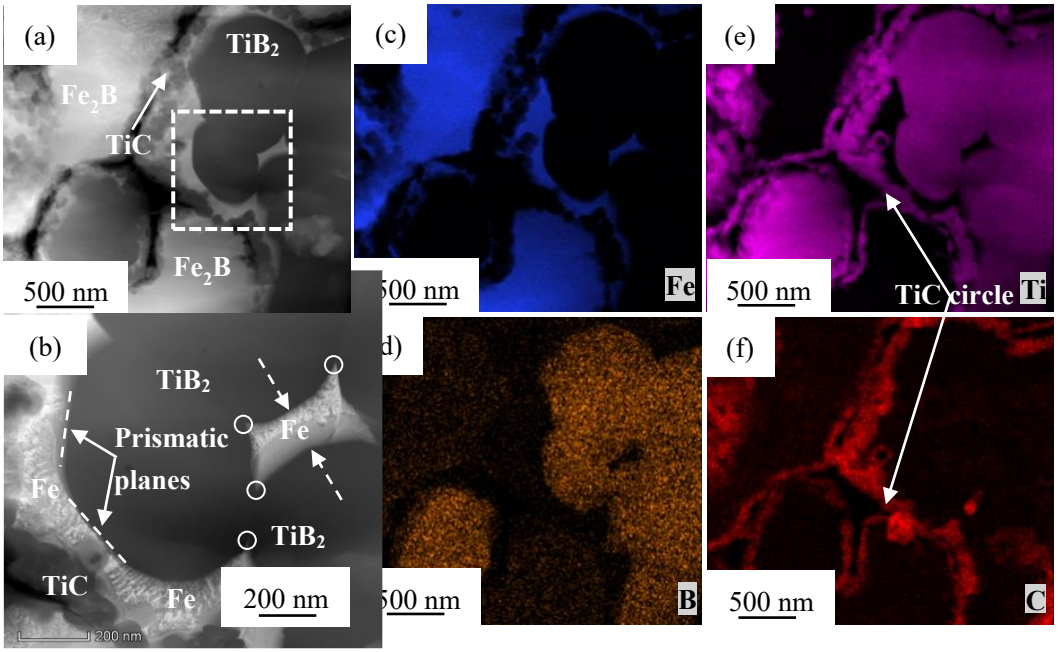

Fig. 3.10 HAADF images of Fe-30vol.%TiB_2 compacts sintered at (a) 1373 K for 0 ks and (b) the high magnification image corresponding to the area in (a) marked by dashed box; (c), (d), (e) and (f) placed on the right are mapping analysis images of Fe, Ti, B and C corresponding to (a).

In the light of work conducted by Cha[6] and Korine[11], fantastic interpretations of Fe/TiB_2 interface at an atomic level obtained by eutectic solidification are evidenced, providing a perspective of better understanding to the interfacial cohesion of Fe/TiB_2. However, little literatures report the Fe/TiB_2 interface of Fe-TiB_2 composites obtained by PM. Therefore, High-resolution characterizations at microscopic and atomic levels were conducted to characterize the Fe/TiB_2 interface in Fe-TiB_2 composites synthesized by PM. A HRTEM image taken on Fe/TiB_2 interface and a fast Fourier transform (FFT) image located in lower right corner corresponding to the marked area are shown in Fig. 3.11(a). In order to evaluate the Fe/TiB_2 interface, the FFT image was filtered and inverse fast Fourier transformed (IFFT) as exhibited in Fig. 3.11(b). Atomic columns were visible in both sides. (100) plane of Fe was parallel to $(10\bar{1}0)$ prismatic plane of TiB_2 and $(\bar{1}01)$ plane of Fe was inclined by 7° from $(01\bar{1}1)$ of TiB_2. The misfit in the interface between $(01\bar{1}1)$ plane of TiB_2 and $(\bar{1}01)$ plane of Fe was 5.9%. It should be accommodated by periodically spaced dislocations which could not be clearly evidenced due to contrast variations in interface, caused by defocus and thickness. This

OR guaranteed a good interfacial cohesion between two phases. As it could be assumed that the prismatic planes of TiB_2 are probably served as nucleation sites for α-Fe transformation from γ-Fe during cooling in term of the occurrence of the special OR[6,11]. A good interfacial cohesion of Fe/TiB_2 interface synthesized by PM method was also confirmed at an atomic level.

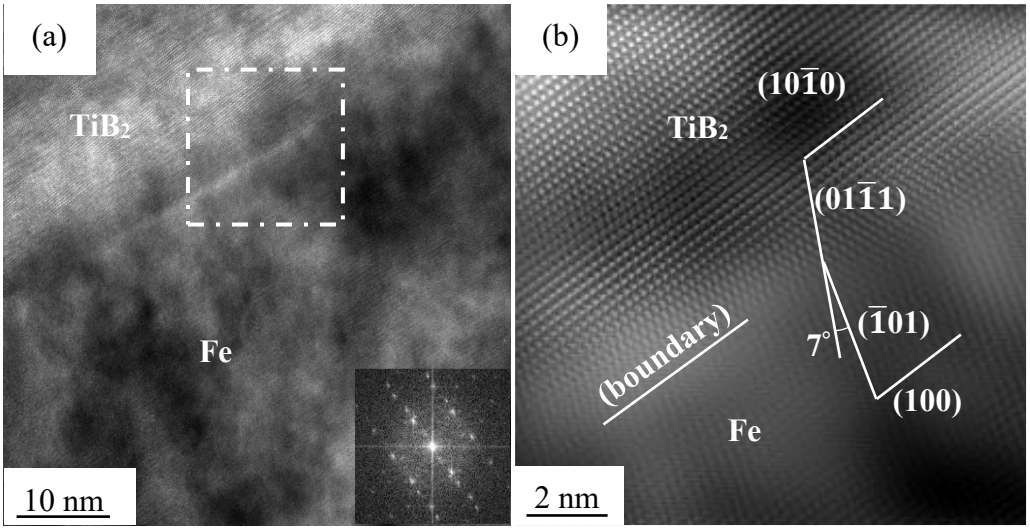

Fig. 3.11 (a) A HRTEM image of Fe/TiB_2 interface in the compact sintered at 1373 K for 0 ks, and an inset in the lower right corner is an FFT image corresponding to the area marked in dashed box, and (b) an IFFT image of Fe/TiB_2 interface corresponding to the area marked in dashed box in (a).

Figure 3.12 shows the HAADF images of compacts sintered at 0.6 and 3.6 ks. TiB_2, Fe_2B, Fe and TiC were indicated, as shown in Fig. 3.12(a)(b). Fe filled in the gap with width of approximate 50 nm between two TiB_2 particles according to the scale bar as shown in Fig. 3.12(a) and no sintering pores were observed at the Fe/TiB_2 interfaces, which demonstrated an excellent interfacial cohesion between Fe and TiB_2. The preferred interface planes for TiB_2 were prismatic planes as indicated in Fig. 3.12(a), but they were not distinguishable in Fig. 3.12(b) as marked by round-shaped TiB_2 due to the overreaction between Fe and TiB_2 when sintered for 3.6 ks.

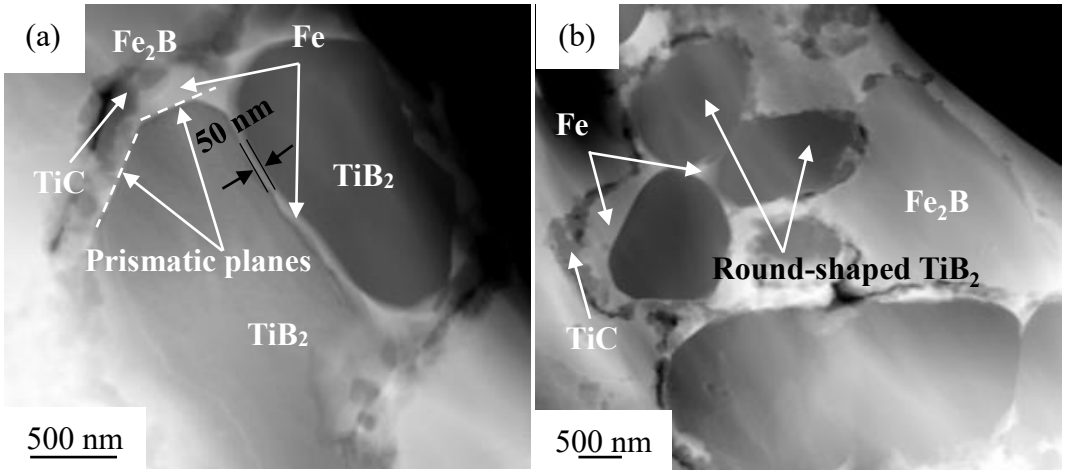

Fig. 3.12 HAADF images of Fe-30vol.%TiB_2 compacts sintered at 1373 K for (a) 0.6 and (b) 3.6 ks.

3.3.2.2 Occurrence of plastic deformation behavior in TiB_2 particles

It is seemingly surprising to be able to observe dislocations in TiB_2 particles as shown in Fig. 3.13 corresponding to the compacts sintered at 1373 K holding 0.6 ks. Not only in this work, other findings about the observation of dislocations in TiB_2 particles were also published. J.R. Ramberg et al.[50] studied the temperature deformation of polycrystalline TiB_2 at a strain rate of 5×10^{-4} s^{-1} and revealed dislocation glide was the deformation mechanism. Wang et al.[51] conducted compression test on NiAl-TiB_2 composites at various strain rates at 1140 and 1300 K and observed the high density of dislocation in TiB_2 particles. Besides, the yield stress at a strain rate of 1×10^{-4} s^{-1} was about 70 MPa for 10-20vol.%TiB_2-NiAl composites. J.D. Whittenberger et al.[52] also reported the dislocation observation within TiB_2 particles from 30vol.%TiB_2-NiAl composites synthesized by hot pressing at 1675 to 1775 K and 128 MPa. Lartigue-Korinek discovered that both basal and prismatic slip plane of TiB_2 were activated concerning the specimen subject to hot rolling at 1173 K[11]. Therefore, ceramics tend to produce dislocations at high temperature and stress. In the case of compacts sintered at 1373 K, 50 MPa, it is quite possible to be able to observe dislocations in TiB_2 particles.

It is quite common to observe dislocations in metals while this is not the case where occurs a lot in ceramics, especially at low temperature. Because ceramics are devoid of slip systems and predominated by directional bonding as opposed to that in metals,

consequently, ceramics cannot accommodate deformations properly and is prone to be fragile at low temperature. Therefore, it is worth noticing the occurrence of deformation behavior in TiB_2 particles during spark sintering. This occurrence of deformation maybe contribute to the activation of slip system of TiB_2 particles at high temperature and stress. In the work of J.R. Ramberg[50], five independent slip systems are required to accommodate a large deformation in polycrystalline. Both basal and prismatic slip systems are activated since these are the most easily activated slip systems, which have also been confirmed by Lartigue-Korinek[11]. The pyramidal slip system $\{10\bar{1}1\}\langle 11\bar{2}0\rangle$ would not take into consideration since it is generally activated only at very high stresses. $\{10\bar{1}0\}\langle 0001\rangle$, $\{0001\}\langle 10\bar{1}0\rangle$ and $\{11\bar{2}0\}\langle 1\bar{1}00\rangle$ are considered to be the remaining possible three slip systems. Moreover, the nature of the chemical bonding of TiB_2, a mixture of covalent and metallic bonding characters, is also thought responsible to a plastic deformation of TiB_2.[11] Occurrence of plastic deformation behavior in TiB_2 particles may be beneficial to the application of HWTs.

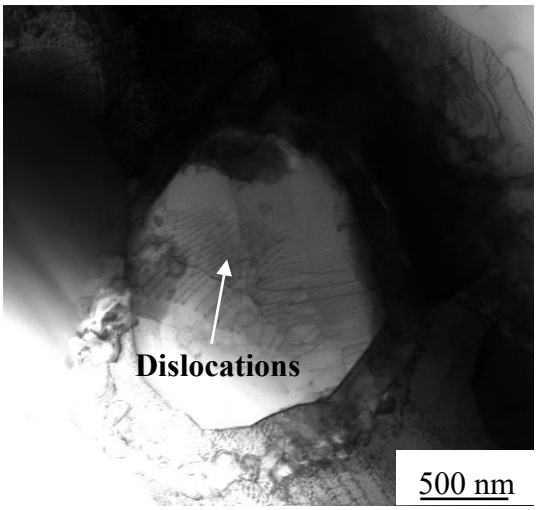

Fig. 3.13 A BFTEM image of Fe-30vol.%TiB_2 compact sintered at 1373 K for 0.6 ks.

3.3.2.3 Reaction mechanism between TiB_2 and Fe

The formation of Fe_2B and TiC is attributed to the reaction of TiB_2 and Fe. But the mechanism of reaction is still under debate. Impurities of C and O in starting powders can consume Ti and lead to the excess B which react with Fe, giving rise to the

formation of Fe_2B[34]. Whereas, in the authors' previous work[49], Fe_2B and TiC were not found in compacts sintered at 1273 K, although there was C existence. Meanwhile, both Fe_2B and TiC were verified in compacts sintered at 1323 K and above. This contradictory, to the authors' knowledge, derived from unspecified synthetic temperature. Dissolution of TiB_2 in Fe is varying at different temperatures. Since negligible TiB_2 dissolute in solid Fe when temperature is lower than 1273 K and hence, no Fe_2B and TiC are generated. On the contrary, there is about 16wt.% solubility of TiB_2 in liquid Fe at 1873 K[53]. In addition, the Gibbs free energy of reactions were calculated using the thermodynamic data[54]. TiB_2 was more energetically favorable compared with Fe_2B and TiC as shown in Fig. 3.14. But still, formation of Fe_2B is reported in Fe-Ti-B system at high temperature[55] even at the absence of C or O. This is ascribed to the heterogeneous distribution of Ti and B atoms in Fe, which will be interpreted later in terms of diffusion kinetics. Therefore, it is considered that dissolution of TiB_2 in the Fe alloys lead to the formation of Fe_2B[53]. Another reason is negligible solubility of B in either α-Fe or in γ-Fe[55], resulting in a direct reaction between Fe and B after the decomposition of TiB_2.

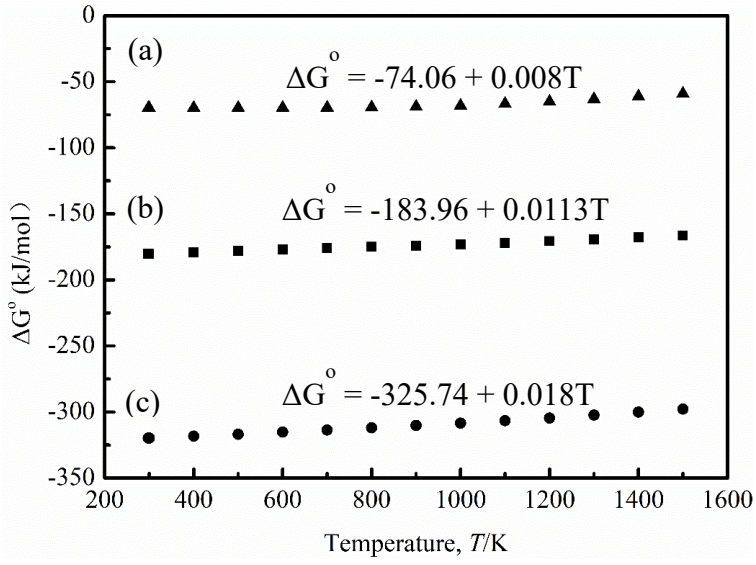

Fig. 3.14 Gibbs free energy change of reactions as a function of temperature: (a) 2Fe + B → Fe_2B, (b) Ti + C → TiC, and (c) Ti + 2B → TiB_2.

As for the distribution of Fe_2B and TiC in compacts sintered in 1373 K described aforehand in Fig. 3.8. This microstructure in Fig. 3.8 could be attributed to the different diffusion behavior of Ti and B driven by chemical potential. The diffusion mode of B atoms in Fe is mainly interstitial diffusion,[56] but it is substitutional diffusion for Ti atoms in Fe.[57] Some assumptions were made to approximately calculate the diffusion depth of Ti and B in Fe. Firstly, the diffusion model was simplified to be an infinite diffusion couple. According to Fick's second law:

$$\frac{\partial C_i}{\partial t} = D_i \frac{\partial^2 C_i(x,t)}{\partial x^2} \quad (3.2).$$

Where $C_i(x, t)$ is the i concentration at the depth x at time t and at temperature T. D_i is the effective diffusion coefficient for i phase. and D_i can be expressed as:

$$D_i = D_0 \exp\frac{-Q}{RT} \quad (3.3).$$

D_0 is a characteristic property of the metal, R is the universal gas constant, T is the absolute temperature, and Q is the diffusion activation energy. In reference to open literatures, the following equations are obtained:

$$D_B^{Fe} = 4.4 \times 10^{-8} \exp\left(-\frac{81.5\times10^3}{RT}\right) \quad (3.4)$$

$$D_{Ti}^{Fe(2wt.\%Ti)} = 0.56 \times \exp\left(-\frac{216.1\times10^3}{RT}\right) \quad (3.5).$$

If the diffusion depth was assumed as following equation.

$$x \approx \sqrt{Dt} \quad (3.\ 6).$$

According to equations (4)[58], (5)[59] and (6), approximate diffusion depth of B and Ti in Fe could be obtained if the compact was sintered at 1373 K for 0.6 ks, they were x_B = 145 μm, and x_{Ti} = 14.4 μm, respectively. Apparently, the diffusion calculations employed were subject to error owing to over simplified diffusion model and to the inaccuracy of the diffusion data employed from literatures. However, it could be concluded that diffusion depth of B was an order of magnitude higher than that of Ti in Fe. The limited dissolution of TiB_2 in Fe at 1273 K and below was due to the insufficient diffusion activation energy needed for atoms diffusion.

In the case of present work, the intrinsic modeling was radial diffusion for Ti and B in Fe. On the purpose of better interpreting the reaction mechanism between Fe and TiB_2, schematic illustrations were drawn as shown in Fig. 3.15 based on the microstructure in Fig. 3.10. The whole process was roughly divided into four stages. In

the first stage, as shown in Fig. 3.15(a), it showed TiB_2 particle was surrounded by Fe particles before the reaction occurred between Fe and TiB_2. The second stage was atom diffusing. According to our previous study[49], TiB_2 particles started to decompose in pure Fe when sintering temperature was over 1323 K. As displayed in Fig. 3.15(b), Ti atoms mainly distributed around TiB_2 particle due to limited diffusion depth, while B atoms scattered more extensively than Ti because of longer diffusion depth, as explained in the above paragraph. Moreover, the further away from TiB_2 particles, the lower concentration of Ti and B atoms were. Therefore, higher concentration of atoms was represented by larger icons. At the same time, Fe also diffused toward TiB_2, which led to a narrow interdiffusion region as indicated by two dashed circles shown Fig. 3.15(b)(c). B atoms directly reacted with Fe after diffusing through the interdiffusion region, resulting in the formation of Fe_2B, as demonstrated in Fig. 3.15(c). This is due to the solubility of B is negligible in both α-Fe and γ-Fe.[55] As time went on, Fe_2B grains grew up as shown in Fig. 3.15(d). The interdiffusion region was considered as a solid solution of Fe-Ti-C (Fe_{ss}), so Ti and C atoms probably started to precipitate at Fe grain boundaries during the γ-α transformation in the fourth stage as shown in Fig. 3.15(d). This is because interface planes between Fe and TiC such as $(1\bar{1}0)_{Fe}$ // $(0\bar{2}0)_{TiC}$ or $(101)_{Fe}$ // $(1\bar{1}1)_{TiC}$ can be envisaged as preferred orientations for the TiC precipitation,[6] on the other hand, the solubility of C in α-Fe is much smaller than that in γ-Fe. TiC other than Fe_3C precipitated from the Fe_{ss}, as the affinity between Ti and C is higher than that between Fe and C. The residual Fe comprised of two types. As shown in Fig. 3.15(d), one wrapped around TiB_2 after TiC precipitation from the Fe_{ss} as indicated by $Fe_{(1)}$; The other type was unreacted Fe as marked by $Fe_{(2)}$ which was initially far away from TiB_2. Fig. 3.15(d) is the final stage which can be proved by the microstructures of compacts as shown in Fig. 3.10 and 3.12.

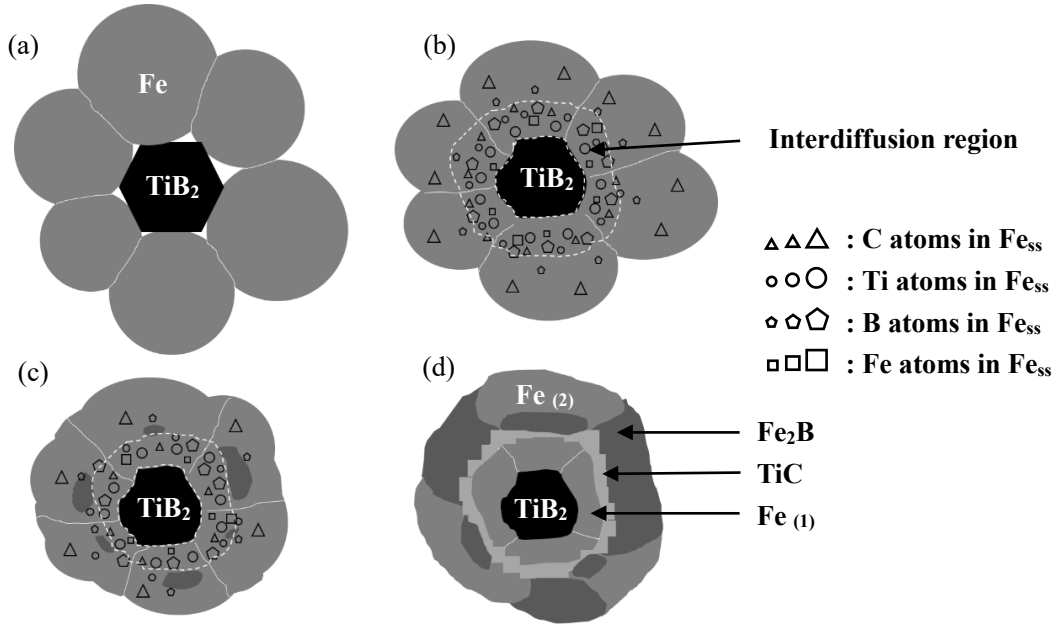

Fig. 3.15 Schematic illustrations of reaction mechanism between Fe and TiB_2: (a) the first stage, (b) second stage, (c) third stage, and (d) fourth stage; In (b) and (c), the triangles, circles, pentagons and squares represent C, Ti, B and Fe atoms in Fe_{ss}, respectively, and the larger icons represent higher concentration of atoms.

3.3.2.4 TC and hardness of Fe-TiB_2 compacts

Microstructure of materials can dramatically influence the mechanical and thermal properties such as strength, hardness, and thermal conductivity. Simultaneously, these properties can determine the applications of these materials in industrial practice. The TC and Vickers hardness of all compacts as a function of holding time was plotted in Fig. 3.16. The TC of pure Fe, TiB_2 Fe_2B and TiC are reported to be 80, 100[1], 35[60] and 21[61] W/(m·K), respectively. Therefore, the theoretical TC of sintered compacts was estimated by simple mixture rule based on the data as shown in Fig. 3.9. The variation trend of theoretical and measured curves was basically same as shown in Fig. 3.16(a). In addition, theoretical TC of sintered compacts was decreased as sintering time increased and was overall higher than the measured one because the defects excluding pores and interface thermal resistance between matrix and reinforcements were not taken into consideration in such calculation. However, defects in compacts[62] and interface thermal resistance between matrix and reinforcements[63] are two important factors influencing TC of materials. As defects and interfaces scatter electron or phonon

during heat transfer, which decrease the mean free length of the path of electron or phonon and thus lead to the decrease of thermal conductivity. Besides, in this study, newly formed phases with low TC were another main reason affecting the whole TC of composites. The TC increased first then decreased as the holding time extended, reaching the maximum at 0.6 ks. Two stages could be roughly divided to explain variation of thermal conductivity. One was the densification stage where defects were gradually diminished from 0-0.6 ks resulting in the improvement of thermal conductivity. It could also be proved by relative density variation in Fig. 3.9(b) showing that the relative density was greatly improved from 0-0.6 ks while it kept almost constant from 0.6-3.6 ks. The other stage was the formation stage of large number of phases with low thermal conductivity, giving rise to the decrease of TC from 0.6-3.6 ks. Therefore, TC of compact at 0.6 ks showed a maximal value, which was probably a trade-off between densification and growing number of phases with low thermal conductivity. Besides, the TC of each sintered compact was also higher than that of SKD61. However, with the increase of holding time, the Vickers hardness increased dramatically from 0-0.6 ks, after that, it slightly increased from 0.6-3.6 ks as displayed in Fig. 3.16(b). This was attributable to the growing number of hard phases (Fe_2B and TiC shown in Fig. 3.9(a)) and to the improved densification shown in Fig. 3.9(b). It was concluded that the compact sintered at 1373 K for 0.6 ks showed the most favorable properties among all the compacts based on relative density, TC and hardness.

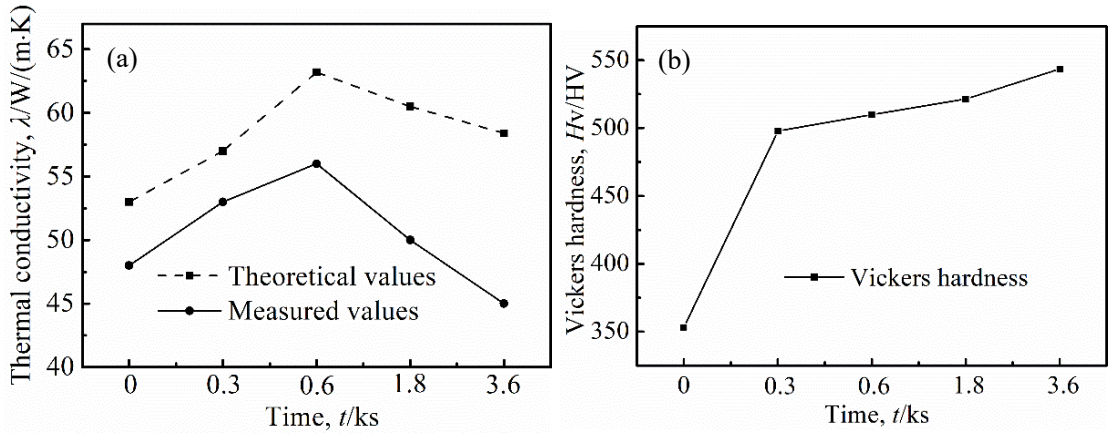

Fig. 3.16 Theoretical and measured TC in (a) and Vickers hardness in (b) of Fe-30vol.%TiB_2 compacts sintered at 1373 K for 0, 0.3, 0.6, 1.8 and 3.6 ks, respectively.

3.4. Adaption of sintering mold

As mentioned above, the C source derived from the graphite die and punches, which had a negative effect on the stability of TiB_2, and hence, a small adaption was attempted, in order to prevent the C from diffusing into compacts. The schematic illustration of adapted mold is shown in Fig. 3.17. A piece of rectangular Molybdenum (Mo) sheet with thickness of 50 um was inserted in the hole of the graphite die and two pieces of round Mo sheets with thickness of 50 um were placed on and below the compact, respectively. That is to say, the compact was encapsulated by Mo sheets. Mo was selected, because it is a refractory metal with melting point of 2896 K, expecting it can paly a role of obstructing the C diffusion into compacts. Thereafter, the compact was sintered at 1373 K for 0.6 ks.

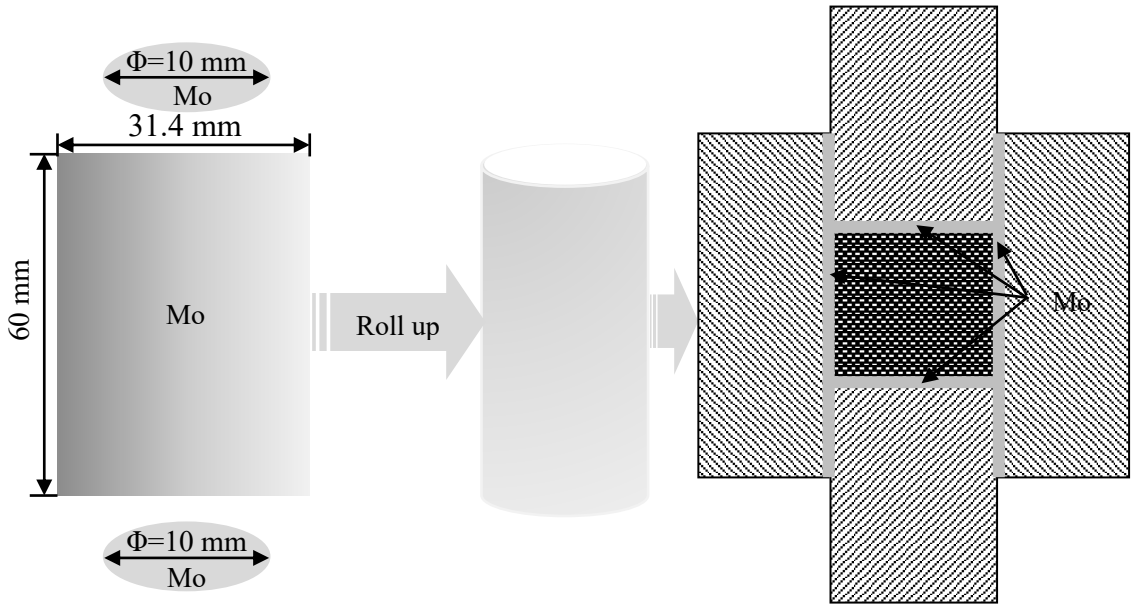

Fig. 3.17 Schematic illustration of adapted mold.

A BSE image of Fe-30vol.%TiB_2 compacts sintered at 1373 K for 0.6 ks by adapted mold, as shown in Fig. 3.18. Based on the results obtained above, the circle-like TiC was marked by white arrows in BSE images, proving that C still diffused into the compact, and hence the adaption of inserting Mo sheets was useless. Besides, the gray parts were indicated as Fe_2B. Up to now, C diffusion from dies and punches is inevitably.

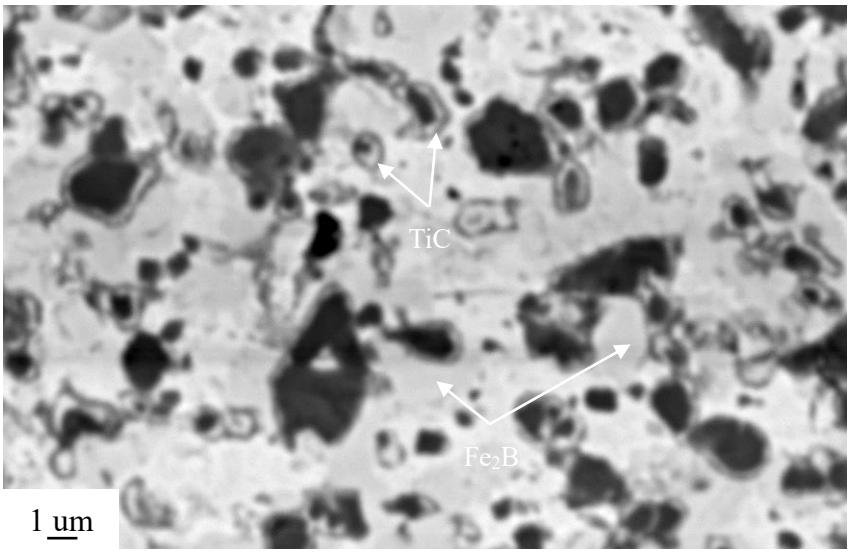

Fig. 3.18 A BSE image of Fe-30vol.%TiB_2 compacts sintered at 1373 K for 0.6 ks by adapted mold.

The formation of Fe_2B and TiC assuredly improve the hardness of the sintered compacts, especially Fe_2B which has been widely used in surface boronizing to enhance the wear resistance of steels. In the case of HWTs, both wear resistance and toughness are indispensable even though they somehow contradict to each other. Therefore, well-tailored microstructure still needs to be investigated in order to reconcile the two properties in the future. On the other hand, the stability of microstructure of composites, especially at the service temperature, is another crucial factor of fabricating materials for the usage of HWTs. For example, in HS process, the workpiece will be heated up to austenite transformation temperature and pressed by HS machine. The service temperature of HS machine is close to austenite transformation temperature. And thus, the thermal stability of microstructure of materials for HS usage is of great importance. But so far, Fe-TiB_2 composites with both high TC and hardness have been synthesized. Especially, the compact sintered at 1373 K for 0.6 ks exhibited the most favorable properties which were 133% higher in TC and comparable in Vickers hardness compared with that of SKD61, as shown in Fig. 3.19.

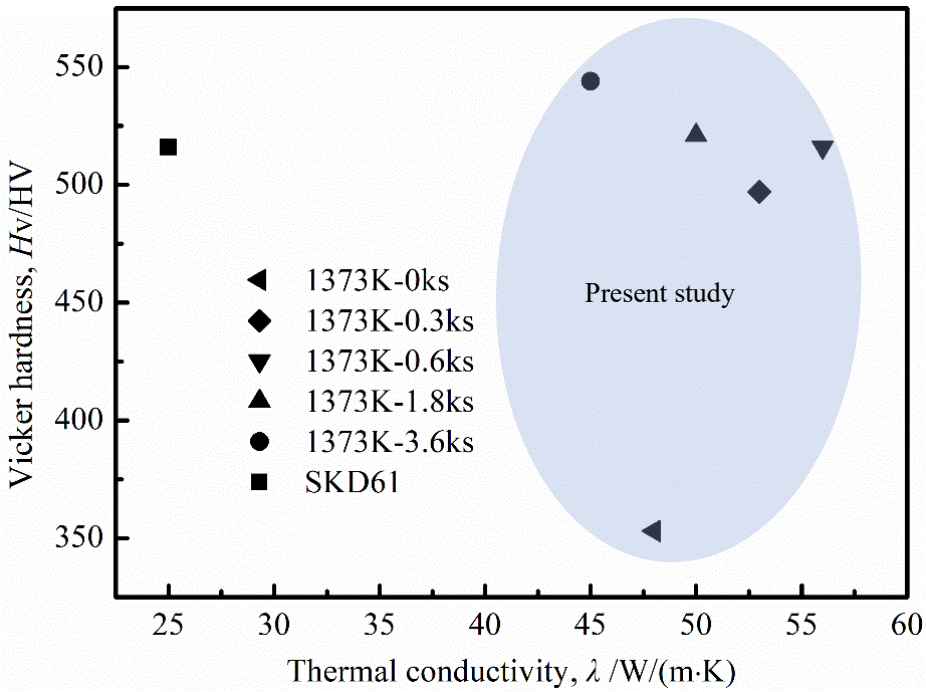

Fig. 3.19 Comparison between Fe-30vol.%TiB_2 sintered compacts in present study and SKD61 in TC and Vickers hardness.

3.5. Summary

The effect of sintering parameters, regarding sintering temperatures and holding times, on microstructures, thermal and mechanical properties were investigated in this study for Fe-30vol.%TiB_2 composites.

Increasing sintering temperatures improved the relative density which led to the densification of compacts. There were only Fe and TiB_2 phases in the compact sintered at 1273 K, however, the phase composition evolved into Fe, TiB_2, Fe_2B and TiC when sintering temperature increased up to 1323 K because of the thermal instability of TiB_2 in pure Fe at high temperatures showing the promotion of the decomposition of TiB_2. Vickers hardness and density improved with the increase of temperatures, while TC showed the minimum value at 1323 K.

For compacts sintered at different holding times, the phase composition was Fe, TiB_2, Fe_2B and TiC. With the increase of holding time, the area fractions of TiB_2 and Fe were decreased while that of Fe_2B and TiC were increased. A good Fe/TiB_2 interfacial cohesion was confirmed at atomic level, which was the occurrence of the special OR between {110} planes of Fe and $\{10\bar{1}0\}$ planes of TiB_2. Dislocation observation in TiB_2 particles proved the plastic deformation ability of TiB_2 at high temperature and stress. Reaction between Fe and TiB_2 was due to the decomposition of TiB_2 in Fe at 1373 K and different diffusion depth of B and Ti in Fe. Thereafter, B directly reacted with Fe, since the solubility of B atoms is low in either α-Fe or in γ-Fe. TiC precipitated from Fe_{ss} along Fe grains boundary as temperature dropped, which led to the residual Fe wrapping around TiB_2. With the increase of holding time, the TC increased first then decreased reaching the maximum at the holding time of 0.6 ks, which caused by a trade-off between increased densification and growing number of phases with low thermal conductivity; However, Vickers hardness was increasing which was attributable to the growing number of hard phases (Fe_2B and TiC). Among all the compacts, the one sintered at 1373 K for 0.6 ks showed the excellent properties which were 133% higher in TC and comparable in Vickers hardness compared with that of SKD61. This work provides a new way to fabricate a future generation of HWTs.

References

1) R. Telle, L.S. Sigl and K. Takagi: Handbook of Ceramic Hard Materials. (2000) 802-945.
2) I. Azkona, F. Castro and J.M. Sánchez: Metall. Mater. Trans. A 36 (2) (2005) 459-466.
3) L. He, Y. Liu, J. Li and B. Li: Mater. Des. 36 (2012) 88-93.
4) A.K. Shurin and N.A. Razumova: Sov. Powder Metall. Met. Ceram. 18 (12) (1979) 903-905.
5) S.S. Ordan'yan, B.Y. Yuriditskii and I.B. Panteleev: Sov. Powder Metall. Met. Ceram. 21 (7) (1982) 595-597.
6) L.M. Cha, S. Lartigue-Korinek, M. Walls and L. Mazerolles: Acta Mater. 60 (2012) 6382-6389.
7) A.D. Panasyuk and A.P. Umansky: J. Less Common Metals 117 (1-2) (1986) 335-339.
8) A. Passerone, M.L. Muolo and D. Passerone: J. Mater. Sci. 41 (16) (2006) 5088-5098.
9) D.H. Bacon, L. Edwards, J.E. Moffatt and M.E. Fitzpatrick: Int. J. Fatigue 48 (3) (2013) 39-47.
10) Y.Z. Li and M.X. Huang: Characterization of Minerals, Metals, and Materials 2017. (2017) 453-460.
11) S. Lartigue-Korinek, M. Walls, N. Haneche, L.M. Cha, L. Mazerolles and F. Bonnet: Acta Mater. 98 (2015) 297-305.
12) M. Dammak, M. Gaspérini and D. Barbier: Mater. Sci. Eng. A 616 (2014) 123-131.
13) D.H. Bacon, L. Edwards, J.E. Moffatt and M.E. Fitzpatrick: Acta Mater. 59 (9) (2011) 3373-3383.
14) C. Baron, H. Springer and D. Raabe: Mater. Sci. Eng. A 724 (2018) 142-147.
15) A. Szczepaniak, H. Springer, R. Aparicio-Fernández, C. Baron and D. Raabe: Mater. Des. 124 (2017) 183-193.
16) H. Springer, C. Baron, A. Szczepaniak, V. Uhlenwinkel and D. Raabe: Sci. Rep. 7 (1) (2017) 2757.
17) C. Baron, H. Springer and D. Raabe: Mater. Des. 111 (2016) 185-191.

18) R. Aparicio-Fernández, H. Springer, A. Szczepaniak, H. Zhang and D. Raabe: Acta Mater. 107 (2016) 38-48.
19) H. Zhang, H. Springer and R. Aparicio-Fernández: Acta Mater. 118 (2016) 187-195.
20) C. Baron, H. Springer and D. Raabe: Mater. Des. 97 (2016) 357-363.
21) H. Springer, R.A. Fernandez, M.J. Duarte, A. Kostka and D. Raabe: Acta Mater. 96 (2015) 47-56.
22) M.X. Huang, B.B. He, X. Wang and H.L. Yi: Scr. Mater. 99 (2015) 13-16.
23) F. Bonnet, V. Daeschler and G. Petitgand: Can. Metall. Q. 53 (3) (2014) 243-252.
24) C.C. Degnan and P.H. Shipway: Metall. Mater. Trans. A 33 (9) (2002) 2973-2983.
25) S.C. Tjong and K.C. Lau: Mater. Lett. 41 (4) (1999) 153-158.
26) A. Anal, T.K. Bandyopadhyay and K. Das: J. Mater. Process. Technol. 172 (2006) 70-76.
27) Y. Wang, Z.Q. Zhang, H.Y. Wang, B.X. Ma and Q.C. Jiang: Mater. Sci. Eng. A 422 (1-2) (2006) 339-345.
28) M. Ziemnicka-Sylwester, L. Gai and S. Miura: Mater. Des. 69 (2015) 1-11.
29) C.C. Degnan and P.H. Shipway: Wear 252 (9-10) (2002) 832-841.
30) L. Gai and M. Ziemnicka-Sylwester: Int. J. Refract. Met. H. 45 (2014) 141-146.
31) A. Fedrizzi, M. Pellizzaria, M. Zadra and E. Marin: Mater. Charact. 86 (2013) 69-79.
32) I.V. Angles, B. Casas, N. Rodríguez and U. Paar: Metall. Ital. 11 (2010) 23-28.
33) R.G. Munro: J. Res. Natl. Inst. Stan. 105 (5) (2000) 709-720.
34) K. Tanaka and T. Saito: J. Phase Equilib. 20 (1999) 207-214.
35) A. Antoni-Zdziobek, M. Gospodinova, F. Bonnet and F. Hodaj: J. Alloys Compd. 657 (2016) 302-312.
36) M. Keddam and R. Chegroune: Appl. Surf. Sci. 256 (16) (2010) 5025-5030.
37) L.G. Yu, X.J. Chen, K.A. Khor and G. Sundararajan: Acta Mater. 53 (8) (2005) 2361-2368.
38) Q.C. Jiang, B.X. Ma, H.Y. Wang and Y.P. Dong: Composites Part A 37 (1) (2006) 133-138.
39) B.H. Li, Y. Liu, J. Li, H. Cao and L. He: J. Mater. Process. Tech. 210 (2010) 91-95.

40) D. Vallauri, I.C. Atías Adrián and A. Chrysanthou: J. Eur. Ceram. Soc. 28 (8) (2008) 1697-1713.

41) K. Matsugi, H. Kuramoto, O. Yanagisawa and M. Kiritani: Mater. Sci. Eng. A 354 (1-2) (2003) 234-242.

42) K. Matsugi, Y. Wang, T. Hatayama, O. Yanagisawa and M. Kiritani: Radiat. Eff. Defect. S. 157 (1-2) (2002) 233-244.

43) K. Matsugi: J. Korean Powder. Metall. Inst. 19 (2) (2012) 127-133.

44) K. Matsugi, H. Kuramoto, T. Hatayama and O. Yanagisawa: J. Mater. Process Technol. 134 (2) (2003) 225-232.

45) Y.C. Wang and Z.F. Fu: Mater. Sci. Eng. B 90 (1-2) (2002) 34-37.

46) Z.H. Zhang, Z.F. Liu, J.F. Lu, X.B. Shen, F.C. Wang and Y.D. Wang: Scr. Mater. 81 (2014) 56-59.

47) Z.F. Xu, Y.B. Choi, K. Matsugi, D.C. Li and G. Sasaki: Mater. Trans. 51 (2010) 510-515.

48) J. Chipman: Metall. Mater. Trans. B 3 (1) (1972) 55-64.

49) Y.J. Ke, K. Matsugi, Z.F. Xu, Y.B. Choi, M.Z. Wang and J.K. Yu: 2018 World Congress on Powder Metallurgy, Part 3-Sintering & Post Processing. 367-372.

50) J.R. Ramberg and W.S. Williams: J. Mater. Sci. 22 (1987) 1815-1826.

51) L. Wang and R.J. Arsenault: Mater. Sci. Eng. A 127 (1990) 91-98.

52) J.D. Whittenberger, R.K. Viswanadham, S.K. Mannan and B. Sprissler: J. Mater. Sci. 25 (1990) 35-44.

53) B.S. Terry and O.S. Chinyamakobvu: Mater. Sci. Technol. 8 (6) (1992) 491-499.

54) D.L. Ye, J.H. Hu: Practical inorganic thermodynamics manual. Metallurgical Industry Press, Beijing. 2002.

55) R. Choteborsky, M. Kolarikova and B.B. Stunova: MM Science Journal (2012) 338-340.

56) W. Wang, S. Zhang and X. He: Acta. Metall. Mater. 43 (4) (1995) 1693-1699.

57) B. Aleman, L. Gutiérrez and J.J. Urcola: Mater. Sci. Technol. 9 (8) (1993) 633-641.

58) M. Keddam: Int. J. Mater. Res. 100 (6) (2009) 901-905.

59) A.W. Bowen and G.M. Leak: Metall. Trans. 1 (10) (1970) 2767-2773.

60) R. Cutler: ASM International, Engineered Materials Handbook. 4 (1991) 787-803.

61) W.S. Williams: JOM. 50 (6) (1998) 62-66.

62) S. Raghavan, H. Wang, R.B. Dinwiddie, W.D. Porter and M.J. Mayo: Scr. Mater. 39 (8) (1998) 1119-1125.

63) C.W Nan, R. Birringer, D.R. Clarke and H. Gleiter: J. Appl. Phys. 81 (10) (1997) 6692-6699.

Chapter 4

Effect of Ti addition in Fe on the fabrication of Fe_2B free Fe base-TiB_2 composites

4.1 Introduction

Ceramic reinforced metal matrix composites (MMCs) have drawn great attention for decades since they incorporate the toughness of metals and the strength of ceramics. Of the various kinds of ceramic reinforced MMCs, Fe (steel) matrix composites are considered as promising materials since Fe (steel) is still the most widely used structural material and provides diverse mechanical properties when subjected to different treatments. In addition, alloying elements additions[1-3], thermal processing or thermo/mechanical processing[4-7], which are highly sophisticated and well established in steels design to alter the constitution and mechanical properties, can be also applied to processing Fe (steel) matrix composites. As for the reinforcing particulates, TiB_2 is one of the high-profile members, due to its excellent hardness, strength, thermal/electrical conductivity and oxidation resistance, which are superior to that of TiC. Moreover, TiB_2 is relatively stable in liquid Fe[8-10] and the solubility of Fe in TiB_2 is lower than 4%[11]. In addition, liquid Fe can wet TiB_2[12,13]. More importantly, Fe-TiB_2 composites fabricated by powder metallurgy (PM) and casting both show good interface cohesion between the matrix and TiB_2 particles[5,14-16,17]. Fracture of TiB_2 particles are inclined to occur before particles/matrices debonding[5,18]. Of most reported Fe-TiB_2 composites, they are expected to apply to high modulus steels[1-3,6,7,11,16,19-23] and wear-resistance parts[24-30], on account of the improved strength, specific modulus and wear-resistance. SKD61 has been wildly used as one of hot work tool steels (HWTs). It is characterized by good abrasion resistance at both low and high temperatures, high level of toughness and ductility, outstanding high-temperature strength and resistance to thermal fatigue.[31,32] However, the low TC of 24 W/(m·K) limits its further applications. As a result, Fe-TiB_2 composites also display great potential in the application of HWTs because of their possibility of high thermal conductivity.

However, the challenge remains with regard to the synthesis of Fe/TiB_2 composites, since Fe_2B, a brittle phase, will always get involved in composites as an undesired resultant which can deteriorate the toughness of composites[33]. In the pursuit of obtaining Fe_2B free Fe/TiB_2 composites, according to the Fe-Ti-B ternary phase diagram[33,34], over stoichiometric amount Ti (atomic ratio of Ti:B≥0.5) is added to

suppress the formation of Fe_2B. Up to date, Fe_2B free Fe/TiB_2 composites have been fabricated by different methods which was summarized in Table 4.1. Casting or eutectic solidification can not only guarantee a clean interface, but also tailor the ratio of each element. Another unparalleled advantage of casting over PM is the higher diffusion coefficient of atoms rendering a more homogeneous distribution of Ti in Fe. However, this route is still open to question due to clustering of TiB_2 particles in Fe matrix[5)] and density-induced floatation of the primary TiB_2 particles[7)], contributing to inhomogeneous microstructure of composites. In addition, the large primary TiB_2 particles are more likely to facture than the small eutectic TiB_2 particles when subjected to stress[18)]. Therefore, more elaborate processes should be taken into consideration to overcome the problems. Self-propagating high-temperature synthesis (SHS) or combustion synthesis is another way reported capable of producing Fe_2B free Fe/TiB_2 composites[24,28,29)]. One of the striking merits of SHS refers to the extreme high temperature caused by heat generated by an exothermic reaction, promoting the occurrence of mass transfer process. Nevertheless, high porosity and aggregation of the newly formed phases[25-28)] are inevitably introduced in products, which is not suitable for the underlying application for structural materials where strength is valued extremely.

PM can precisely control the volume fraction and size of reinforcements in matrix though, it is still seemingly to be the least impossible method to fabricate the Fe_2B free Fe/TiB_2 composites due to the low diffusion coefficient of atoms in solid state sintering，in despite of an extra addition of Ti powder into Fe and TiB_2 powder mixtures. In this study, (Fe-2Ti)-20vol.%TiB_2 compacts, where powder mixtures were obtained by simply mixing Fe, Ti and TiB_2 powders, were sintered at 1373 K for 0.3 ks. Ti remained almost the same state with that of the initially added one as shown in Fig. 4.1(a) marked by white circles, besides, the point analysis placed in upper right in Fig. 4.1(b) also proved that Ti atoms did not solid solute into Fe matrix. The formation of Fe_2B was observed as marked by white arrows in Fig. 4.1(b). That is, Ti is ineffective if it is just added into Fe and TiB_2 powder mixtures. In contrast, mechanically alloying (MA), a non-equilibrium processing technique, has been carried out to synthesize supersaturated solid solutions, nanocrystallines, alloys, high entropy alloys (HEA)[35,36)], etc. This offers

a new possibility to fabricate a Fe-Ti alloyed powders in which Ti atoms solid solute in Fe lattice. In recent years, alloy and HEA powders synthesized by MA have been extensively used in the fabrication of alloy (HEA)/TiB_2 composites[37-43]. Evidently, it is also feasible to use MAed (Fe-Ti) alloy powders and TiB_2 powders to fabricate (Fe-Ti)/TiB_2 composites and further realize the synthesis of Fe_2B free Fe/TiB_2 composites. Hence, monophase BCC structured Fe-Ti (percentage by atom is used unless otherwise specified) alloy powders were fabricated by MA. Moreover, it is considered that Fe-5Ti is promising as the matrix in (Fe-5Ti)/TiB_2 composites. Spark sintering was chosen to sinter (Fe-5Ti)/TiB_2 composites because it has the potential to retard grain growth, suppress the thermal decomposition and purify the surface of powders through dielectric breakdown of an oxide film by proper control of process.[44,45] Therefore, it is a highly efficient sintering technique applying to rapidly synthesizing a wide range of materials at lower temperature.[46-49] It is concluded that (Fe-5Ti)-30vol.%TiB_2 composites consolidated by spark sintering are underlying materials compared with those of SKD61 mentioned above. The optimization among used powders, process parameters and system have to be carried out for achievement of fabrication of objective composites in spark sintering.[44,45]

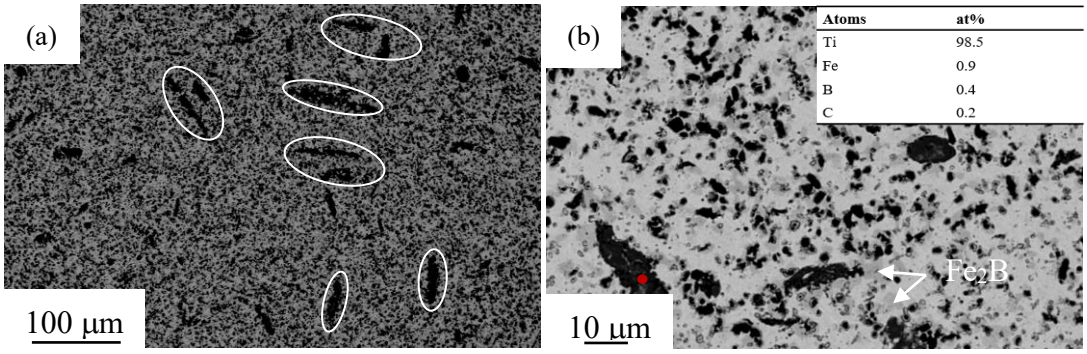

Fig. 4.1 SEM images (a) and BSE image (b) of (Fe-2Ti)-20vol.%TiB_2 compact sintered 1373 K for 0.3 ks.

Table 4.1 Summary of literatures investigation.

Author	Nominal compositions (wt%)	Fabrication Method	Reacted phase	Application	Refs
H. Spring et al.	Fe -4.76 Ti-1.78 B Fe -10.10 Ti-3.86 B	Arc-melting casting In-situ	--	HMS	21)
R. Aparicio-Fernabdez et al.	Fe -10.10 Ti-3.86 B	Arc-melting casting In-situ	--	HMS	18)
H. Zhang et al.	Fe -10.10 Ti-3.86 B	Casting	--	HMS	19)
Limei Cha et al.	12vol.%TiB_2 in cast sample with 0.04 C	Casting	TiC	HMS	30)
Sylvie Lartigue-Korinek et al.	0.04 C	Casting	TiC	HMS	11)
Mara Ziemnicka-Syiwester et al.	TiB_2-25vol.%Fe TiB_2-35vol.%Fe-6vol.%Ti	SHS	Fe_2B No Fe_2B		28)
Animesh Anal et al.	--	SHS	Fe_2B	WRPS	26)
C.C. Degnan. et al.	Fe-70 pct TiB_2 Fe-(50 pct TiB_2 + 50 pct Ti)	SHS	Fe_2B ，TiC TiC	HMS	24,29)

※ SHS: Self-propagating High-temperature Synthesis HMS: High modules steels WRPS: Wear resistance parts

In this study, in order to fabricate Fe_2B free TiB_2 reinforced Fe based composites by the spark sintering with both high TC and hardness in the application of HWTs. The effect of Ti addition in Fe matrix on fabrication of Fe_2B free TiB_2 reinforced Fe based composites was investigated. The microstructures, phase composition, TC and mechanical properties of sintered compacts were also characterized in detail.

4.2 Experimental procedure

4.2.1 Compositions, used materials and synthesis

As-received TiB_2 (99.9%, Pure Chemical Co., Ltd. Japan) pure Fe (99.9%, Sanwa Metal Industry Co., Ltd. Japan) and pure Ti (99.9%, Pure Chemical Co., Ltd. Japan) powders with size of 2~3, ~26 and ≤ 45 μm, respectively, were used as starting powder materials. The microstructural characterizations of the starting powders are shown in Fig. 4.2(a)-(c), and the insets positioned in the upper-left corner of each image correspond to the areas marked by white dashed boxes. As-received Fe powders appeared to be relatively uniform particle size; but it was different for as-received Ti exhibiting an inhomogeneous size distribution with size distribution from several to several tens micrometer; The particle size also scattered in as-received TiB_2, in addition to that, the cleavage surfaces of TiB_2 could be observed clearly, which might be due to the mechanical crush process.

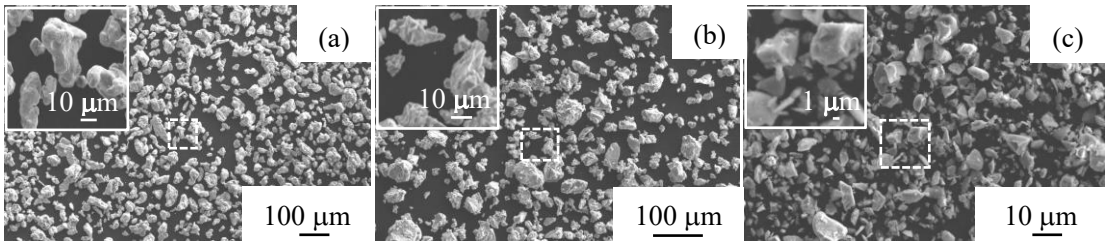

Fig. 4.2 Low and high magnification of SEM images of the starting powders: (a) as-received Fe powders, (b) as-received Ti powders and (c) as-received TiB_2 powders; the insets positioned in the upper-left corner are the high magnification images. corresponding to the areas marked in white dashed boxes in (a), (b) and (c), respectively.

Fe-5Ti monophase BCC structured Fe-xTi alloys (x=5 and 10) were chosen due to the following reasons. Firstly, the solid solubility of Ti in Fe is about 7at. % at 1373 K in equilibrium state according to Fe-Ti binary phase diagram;[50] Secondly, a quasibinary behavior exists along line TiB_2-Fe containing 2-3%Ti,[33] that is to say, TiB_2 is thermally stable in Fe-(2-3%Ti). Thirdly, the Ti addition should be higher than 2-3% to neutralize any inadvertently present C or O. And hence, pure Fe and Ti powders were mixed at an atom ratio of 9:1 and 19:1, and mechanical alloyed in a planetary ball-miller (QM-BP,

Nanjing NanDa Instrument Plant, Nanjing, China) for 108 ks at 400 rpm in an argon atmosphere. MA was paused for 1.8 ks after each 3.6 ks of running. WC vials and balls with a diameter of 2~10 mm was utilized as the milling media with a ball-to-powder mass ratio of 20:1. Ethanol served as the process control agent to avoid cold welding as well as to prevent the alloy from oxidizing.

30vol.%TiB_2 addition was selected based on previous work for achieving the target value of hardness. Hence, 30vol.%TiB_2 and 70vol.% as-alloyed Fe-xTi powders with a total amount of 15 g were placed in a stainless-steel jar with a volume of 250 cm^3, and then 25 mL ethanol was added as a wet mixing agent. Hereafter, the jars were vacuumed for 0.3 ks. Stainless-steel balls (SUS304) with a diameter of 2~10 mm was used for blending and the ball to powder mass ratio was 10:1. Mixing process was conducted in a planetary mill (Fritsch Pulverisette, Germany) at 100 rpm for 10.8 ks. Slurry of powder mixtures was dried in a fume hood and then dry mixed for 3.6 ks afterwards.

Powder mixtures were loaded in a graphite die and consolidated by spark sintering (CS12567, Japan). All spark sintering experiments were carried out at an applied pressure of 50 MPa, heating rate of 100 K/min and holding time of 0.6 ks in vacuum. Hence, (Fe-xTi)-30vol.%TiB_2 composites were obtained at 1323 and 1373 K for 0.6 ks. The die temperature was monitored using an infrared radiation thermometer focused into the hole of die. The temperature of compacts could be estimated approximately 40 K higher than that of die[48]. Compacts with height of 10 mm and diameter of 10 mm were obtained. And then compacts were ground by SiC abrasive paper and polished by diamond paste for the succedent characterizations.

4.2.2 Characterizations of starting powders and sintered compacts

Morphology of powders and microstructure of sintered compacts were observed by electron probe micron analyzer (EPMA, JXA-8900, JEOL, Japan). Phase identification of sintered compacts was characterized by X-ray diffraction (XRD, D/max-2500PC, Rigaku, Japan) with Cu Kα radiation (L=15418 nm, 40 kV, 100 mA). Transmission electron microscope (TEM, JEM-2010, JEOL, Japan) was performed to observe the interface between Fe and TiB_2. Image analysis was employed to obtain the particle size distributions of starting powders and area fraction of each phase in sintered compacts.

Vickers hardness was obtained by Vickers hardness tester (MHT-1, Japan) at a load of 5 kg and a dwelling time of 10 s. In order to observe the crack propagations, a load of 30 kg was applied to compacts by using the same hardness tester. The thermal diffusivity (α) of the samples with dimension of Φ10 × 1 mm was measured at room temperature by a laser flash thermal constant measuring apparatus (Thermal conductivity-9000h, Ulvac-riko, Japan). The specific heat capacity (Cp) of the samples with dimension of Φ4 mm×0.5 mm was also measured at room temperature by differential scanning calorimeter (DSC, STA449C, Germany). Density (ρ) of sintered compacts was acquired by Archimedes' principle. TC(λ) of sintered compacts was calculated according to the equation (1).

$$\lambda=\alpha.Cp.\rho \tag{4.1}$$

Compression test specimens are cylindrical with the dimension of Φ4 mm×6 mm. Room temperature compression tests were performed on a mechanical testing machine (Autograph DCS-R-5000, Shimadzu Corporation, Japan) at an initial strain rate of 1.7×10^{-3} s^{-1}.

4.3 Results and discussion

4.3.1 Fabrication of (Fe-10Ti)-30vol.%TiB_2 composites

4.3.1.1 XRD of MAed Fe-10Ti powders

The XRD patterns of as-alloyed Fe-10Ti powders milled at different times (0, 36, 72, 108 ks) were obtained as shown in Fig. 4.3. As-received Fe and Ti were α-Fe and hexagonal Ti. As milling time increase to 36 ks and longer, α-Fe or body centered cubic (BCC) was the main phase, and no peaks of hexagonal Ti was observed. The degradation or even vanishing of diffraction peak of Ti might be caused by, on the one hand, solid solution of Ti atoms into Fe lattice by mechanical force provided by MA, one the other hand, amorphization of Ti particles during MA process. Furthermore, as milling time increases to 72 ks, left-shift of (110) plane of Fe was observed as highlighted in the inset corresponding to the area marked by dotted rectangle, indicating that solid solution degree of Ti into Fe was deepening with prolong milling time. However, no obvious peaks shift but much broadening peaks were observed at 108 ks milling compared to that of 72 ks milling, which implied the formation of a simple solid solution of monophasic BCC phase at 108 ks milling. Peaks broadening might be ascribed to amorphization, reduction of grain size, lattice distortion brought about by MA[35,36]. However, the as-alloyed powders were inevitably contaminated by WC introduced by ball wear as peaks of WC were observed.

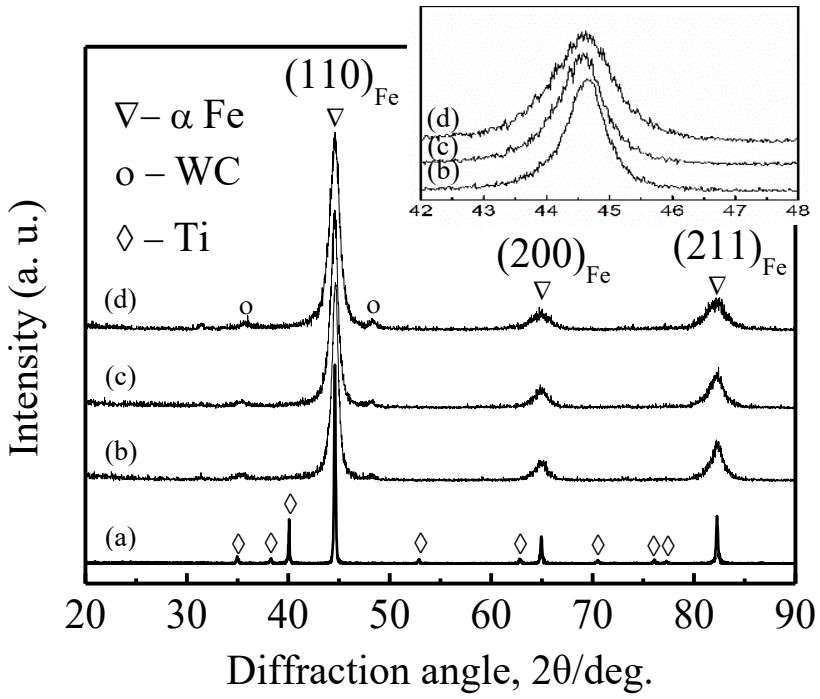

Fig. 4.3 XRD patterns of as-alloyed Fe-10Ti powders milled at different milling times: (a) 0, (b) 36, (c) 72 and (d)108 ks.

4.3.1.2 Morphologies of MAed Fe-10Ti powders

Microstructures of as-alloyed Fe-10Ti powders milled at different times were shown in Fig. 4.4. The powder particles appeared to be granular after 36 ks milling as demonstrated in Fig. 4.4(a) while most of particles transformed into severely deformed and flattened morphologies as milling time extents to 72 ks as evidenced in Fig. 4.4(b). Where after larger particles gradually broke into smaller ones, but some large particles which were likely to be agglomerates of Fe-Ti alloy were also observed after 108 ks milling as shown in Fig. 4.4(c). The evolution process of particles morphology agreed well with the fundamental process in MA, in which repeated welding and fracturing of a powder mixture in a highly energetic ball charge are involved[35]. As a result, the particle size was decreasing from 8.2 to 1.1 μm with the increase of milling time and controlled microstructure of Fe-10Ti alloy powders could be obtained.

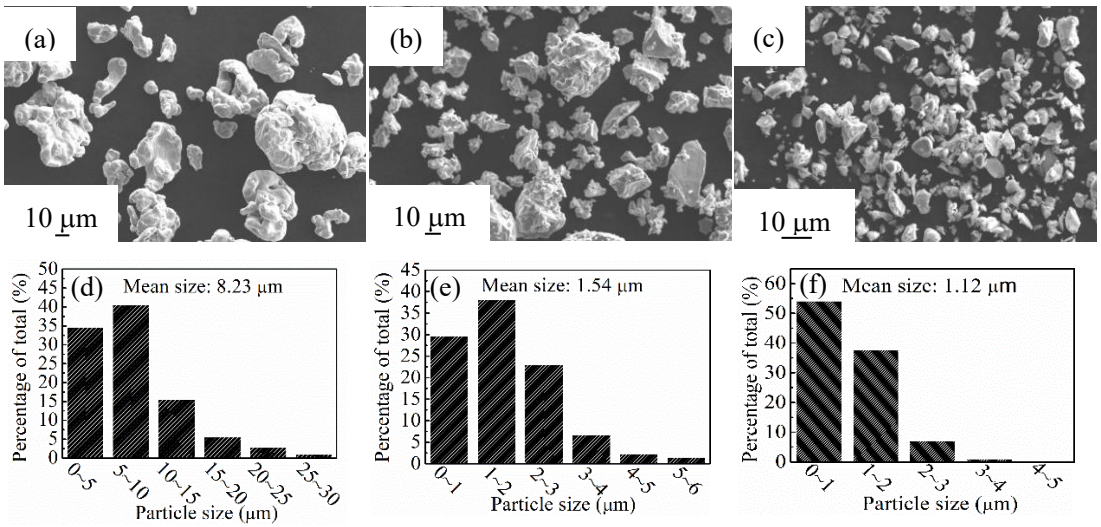

Fig. 4.4 SEM images particle size distributions of as-alloyed Fe-10Ti powders milled at different times: (a) 10 h, (b) 20 h and (c) 30 h; (d), (e) and (f) are particle size distributions graphs.

4.3.1.3 XRD of sintered (Fe-10Ti)-30vol.%TiB_2 compacts

The XRD patterns of (Fe-10Ti)-30vol.%TiB_2 compacts sintered at 1323 and 1373 K for 0.6 ks were obtained as shown in Fig. 4.5. α-Fe and TiB_2 were the main phases in both compacts. Noticeably, no peaks of TiC and Fe_2B was observed. These two phases were the most reported intermetallic in literatures while not desirable in Fe-TiB_2 system, especially the formation of the brittle Fe_2B phase since it can deteriorate the mechanically properties of composites. Consequently, this result proved that the decomposition of TiB_2 is successfully suppressed. However, the titanium oxide was also introduced as indicated, this might derive from oxide layer on as-received Ti particles or oxidation of titanium during MA process. In addition, the formation of intermetallic of Fe_2Ti was also identified in both compacts, this was ascribed to the over-added Ti into Fe matrix since the solubility of Ti in Fe is about 7% at 1373 K in equilibrium state according to Fe-Ti binary phase diagram. And hence, the excessive Ti reacted with Fe and led to the formation of Fe_2Ti.

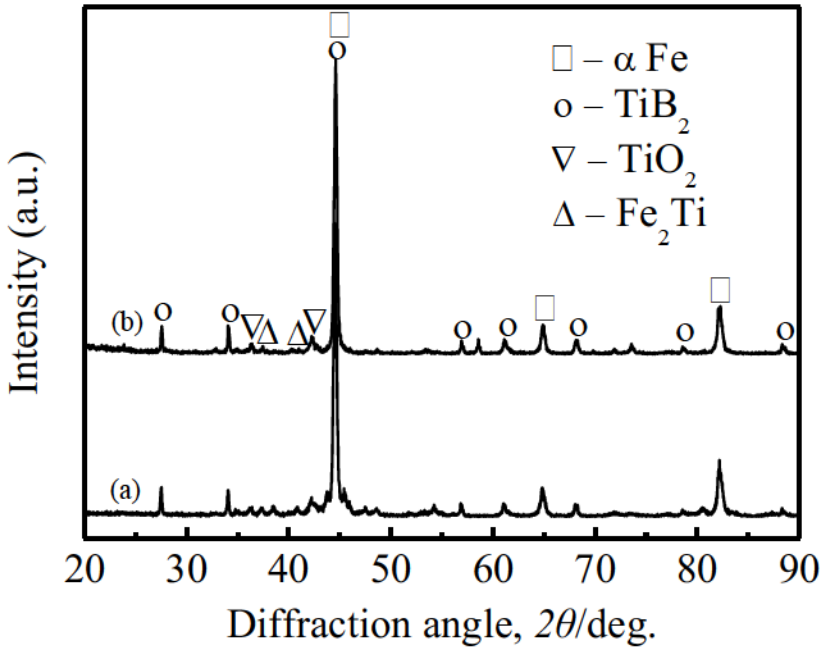

Fig. 4.5 XRD patterns of (Fe-10Ti)-30vol.%TiB_2 compacts sintered at different temperatures: (a) 1323 K and (b) 1373 K for, 0.6 ks.

4.3.1.4 Microstructures of (Fe-10Ti)-30vol.%TiB_2 compacts

The microstructural characterizations of (Fe-10Ti)-30vol.%TiB_2 compacts were shown in Fig. 4.6. The BSE images exhibited that there were mainly two phases as shown in Fig. 4.6(a)(d). The black and gray parts corresponded to TiB_2 and Fe-Ti alloy, respectively, which was in line with the result obtained from XRD. In order to calculate the fractions of each phase, the BSE images were processed by image analysis by which each phase were dyed with different colors as highlighted in Fig. 4.6(b)(e), thereafter, semi-quantitative area fraction calculation displayed in pie charts in Fig. 4.6(c)(f). The area fractions of TiB_2 in each compact were 29.1% for 1323 K and 30.1% for 1373 K, almost the same amount with initial TiB_2 addition. This result further confirmed that pre-alloyed Fe-10Ti powder was an effective binder for purpose of preventing the TiB_2 from decomposing.

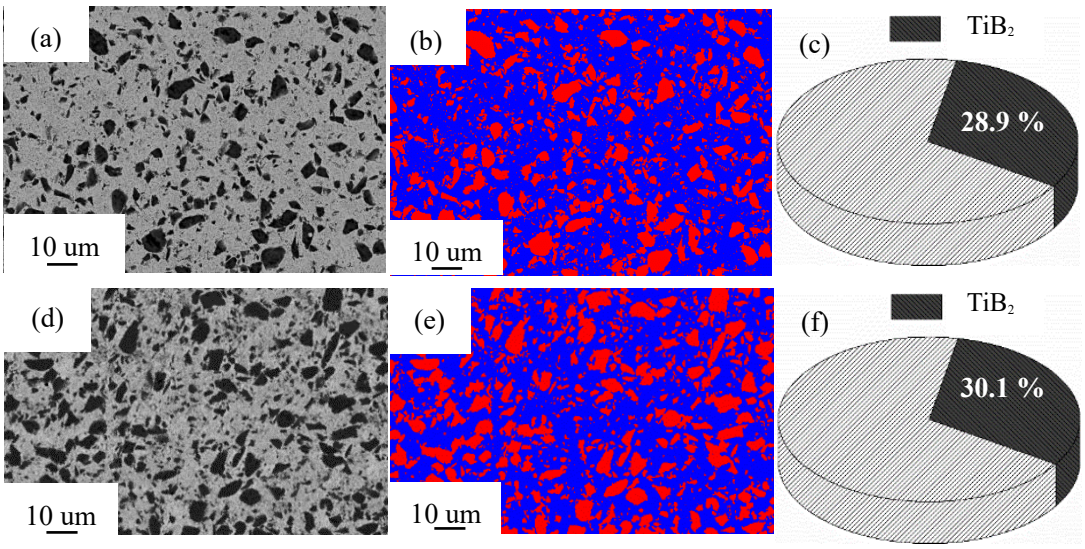

Fig. 4.6 BSE images of (Fe-10Ti)-30vol.%TiB_2 compacts sintered at: (a) 1323 K for 0.6 ks and (d) 1373 K for 0.6 ks; (b) and (e) are the corresponding images processed by image analysis; (c) and (f) are the pie charts demonstrating the area fraction of each phase.

4.3.1.5 TC and hardness of (Fe-10Ti)-30vol.%TiB_2 compacts

TC and Vickers hardness were measured in order to make a comparison with SKD61. The TC and Vickers hardness of compacts sintered at 1323 and 1373 K for 0.6 ks are 32.7 W/(m·K), 686.7 HV and 38.2 W/(m·K), 727.5 HV, respectively, as shown in Fig. 4.7, which were 36%, 33% and 58%, 41% higher than that of SKD61 (24 W/(m·K) and 516 HV). With the increase of sintering temperature, both TC and Vickers hardness were improved, this might be attributed to the lower porosity and enhanced interfacial bonding between Fe/TiB_2 of the compact sintered at 1373 K. Defects[51] and interface thermal resistance[52] are two predominant factors which influence TC of composites, as they can scatter electron or phonon during heat transfer and then decrease the mean free length of the path of electron or phonon, leading to the decrease of thermal conductivity. In this case, lattice distortion of Fe caused by Ti solid solution was the dominant defect which impaired the TC of compacts as well. Additionally, titanium oxide, confirmed by XRD in Fig. 4.5, was another unfavorable factor decreasing the thermal conductivity, on account of the low TC of titanium oxide itself and the increase of heterophase interface. Nevertheless, a higher TC of (Fe-10Ti)-30vol.%TiB_2 composite could be

expected if the formation of titanium oxide can be suppressed. Meanwhile, Fe-5Ti alloy powder will be investigated in the cause of introducing less lattice distortion of Fe but still preventing TiB_2 from decomposing.

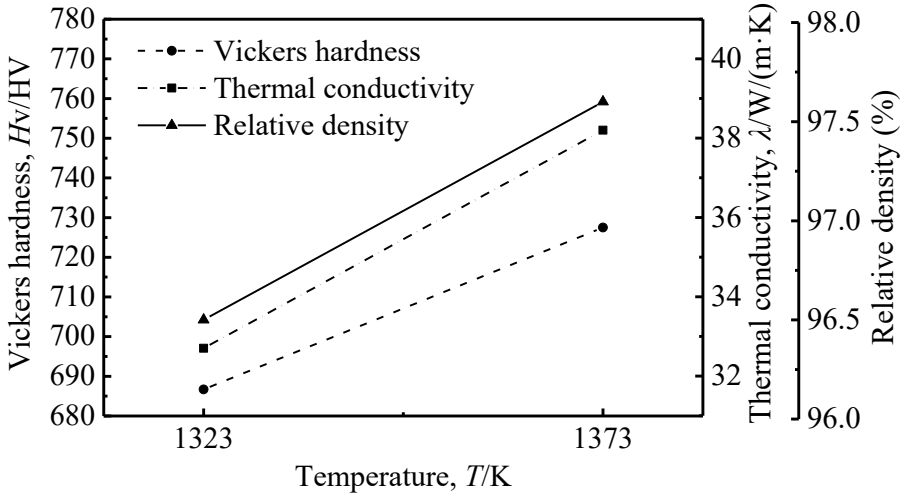

Fig. 4.7 Vickers hardness, TC and relative density of (Fe-10Ti)-30vol.%TiB_2 compacts sintered at 1323 and 1373 K for 0.6 ks

4.3.2 Fabrication of (Fe-5Ti)-30vol.%TiB_2 composites

4.3.2.1 XRD of MAed Fe-5Ti powders

The XRD patterns of as-alloyed Fe-5Ti powders milled for different times (0, 36, 72, 108 ks, respectively) are shown in Fig. 4.8. Overall, the phase evolution process of Fe-5Ti is similar with that of Fe-10Ti. The pattern of Fe-5Ti powder mixture MAed for 0 ks explicitly revealed two phases of α-Fe and hexagonal Ti. As the milling time increased to 36 ks and longer, the phase constitution evolved into mainly α-Fe or body centered cubic (BCC) phase, and no peaks of hexagonal Ti was found as seen in Fig. 4.8(a)-(c). Moreover, with prolong the milling time to 72 ks, left-shift of (110) plane of Fe was observed as highlighted in the upper-right inset corresponding to the area marked by dotted rectangle. This indicated that solid solution degree of Ti into Fe was enhancing with prolonging the milling time. Left-shift of peaks ascribed to the increase of interplanar spacing according to Bragg equation. This was quite reasonable since smaller Fe atoms (0.172 nm) were substituted by larger Ti atoms (0.2 nm). However, no obvious peaks shift but much broadening peaks were observed at 108 ks milling

compared with that of 72 ks milling, which meant a simple solid solution of monophase structured BCC phase was also formed at 108 ks milling. As a result, alloyed powders milled at 108 ks were selected as the matrix.

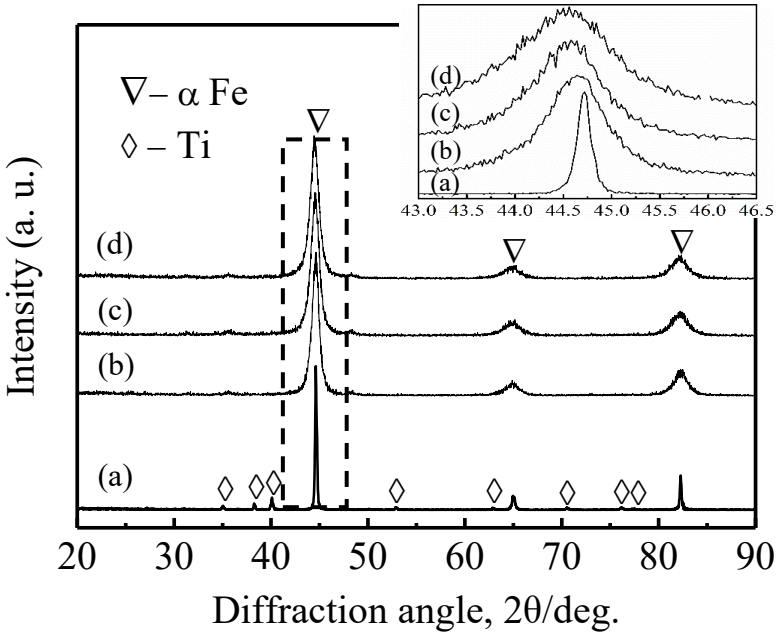

Fig. 4.8 XRD patterns of as-alloyed Fe-5Ti powders milled for (a) 108 ks, (b) 72 ks, (c) 36 ks and (d) 0 ks; the inset positioned in the upper-right corner is the magnified image corresponding to the area marked by dotted rectangle.

4.3.2.2 Morphologies of MAed Fe-5Ti powders

Morphologies of as-alloyed Fe-5Ti powders milled for different times are shown in Fig. 4.9. Generally, the morphology evolution of Fe-5Ti was similar with that of Fe-10Ti as described before. The powder particles transformed from granular when milled for 36 ks as demonstrated in Fig. 4.9(a) to severely deformed and flattened morphologies as the milling time extended to 72 ks as evidenced in Fig. 4.9(b). Finally, larger flattened particles were gradually milled into finer ones after 108 ks milling as shown in Fig. 4.9(c). In addition, the particle size distributions are illustrated in Fig. 4.9(d)-(f) and the mean particle size reduced from 7.74 μm to 1.07 μm with the increase of milling time. Consequently, controlled microstructure and size of monophase BCC structured Fe-5Ti alloy powders could be obtained by MA.

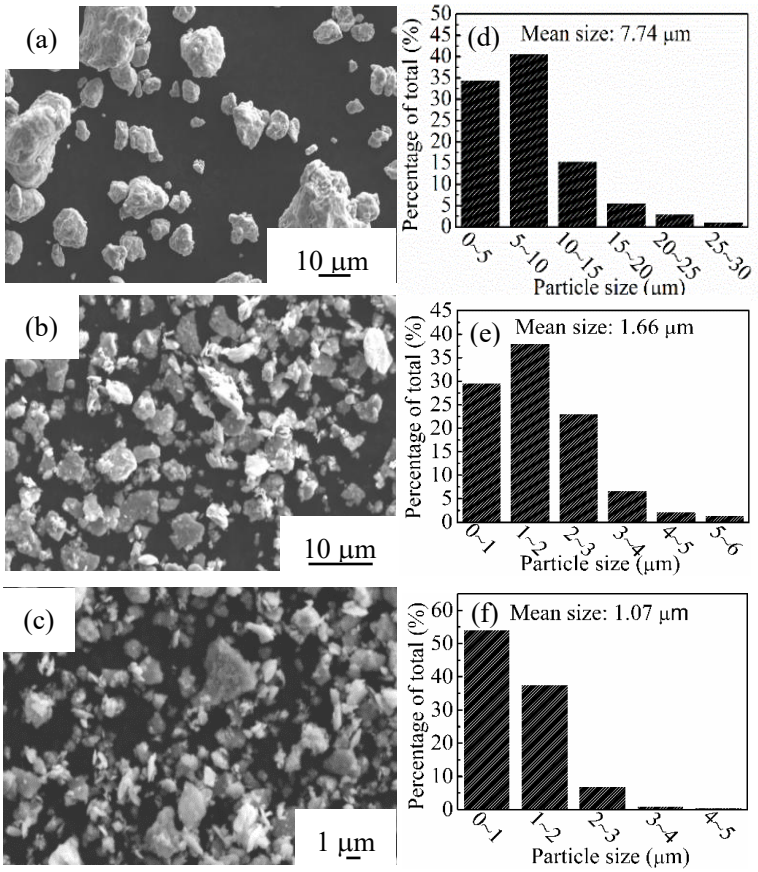

Fig. 4.9 SEM images of as-alloyed Fe-5Ti powders milled for different times: (a) 36 ks, (b) 72 ks and (c) 108 ks; (d), (e) and (f) are particle size distributions corresponding to (a), (b) and (c), respectively.

4.3.2.3 XRD of (Fe-5Ti)-30vol.%TiB_2 compacts

The XRD patterns of (Fe-5Ti)-30vol.%TiB_2 compacts sintered at 1323 and 1373 K for 0.6 ks are shown in Fig. 4.10. The main phase constitutions of both compacts were α-Fe and TiB_2 phases. The peaks shift of Fe of sintered compacts was also observed duo to some Ti solubility in Fe when compared with reference cards. The peaks of α-Fe in sintered compacts were shifted toward to low angle compared with that of pure Fe and located between peaks of pure Fe (PDF#89-7194) and that of Fe-3.6Ti alloy (PDF#65-7743). In contrast, the peaks of TiB_2 were not shifted regardless of sintering temperature. This result was consistent with the introduction that 2-3at. %Ti solubility in Fe is essential for the thermal stability of TiB_2 in Fe at high temperature.[33] Noticeably, no peaks of TiC and Fe_2B was observed in the XRD patterns. These two phases were the most reported intermetallic in literatures[11,16,24,28,29] while not desirable

in Fe-TiB_2 system, as they will deteriorate the mechanically properties of composites, especially the existence of the brittle Fe_2B phase as mentioned in introduction. Besides, no peaks of Fe_2B also proved that the decomposition of TiB_2 was suppressed, and thus, the thermal stability of TiB_2 in the Fe-5Ti alloy was achieved successfully. It might be possibly interpreted that the introduction of Ti into Fe balanced the chemical potential of Ti atom in both sides of TiB_2 and Fe-5Ti alloy. The crystallization of Fe-5Ti also occurred during sintering process as the diffraction peaks became narrower and sharper, compared the XRD pattern in Fig. 4.10 with that in Fig. 4.8. However, TiO_2 with minor amount was observed as well in XRD pattern in both compacts as indicated in Fig. 4.10.

Compared with the (Fe-10Ti)-30vol.%TiB_2 compacts, no intermetallic (Fe_2Ti) were indicated in (Fe-5Ti)-30vol.%TiB_2 compacts, and yet the formation of Fe_2B were successfully suppressed. Therefore, Fe-5Ti is more suitable than Fe-10Ti to be a new matrix. Because over-added Ti into Fe matrix cause the formation of intermetallic which apparently are not desirable on one hand, on the other hand, Ti solid solution introduce the lattice distortion in Fe, which decrease the TC of matrix.

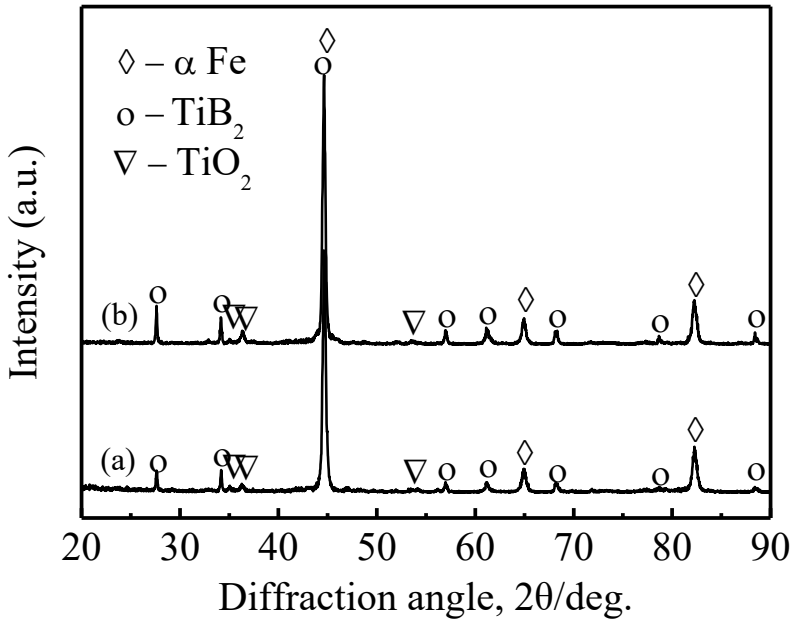

Fig. 4.10 XRD patterns of (Fe-5Ti)-30vol.%TiB_2 compacts sintered at (a)1323 and (b) 1373 K for 0.6 ks.

4.3.2.4 Microstructures of (Fe-5Ti)-30vol.%TiB_2 compacts

The microstructural characterizations of (Fe-5Ti)-30vol.%TiB_2 compacts are shown in Fig. 4.11. TiB_2 (black areas) and Fe-5Ti alloy (gray areas) were indicated in Fig. 4.11 (a)(b). TiB_2 particles were homogenously distributed in matrix in both compacts due to well-designed mixing process introduced in section mentioned above. The sintering pores were indicated in the upper-left insets corresponding to the areas marked by white boxes and more sintering pores were observed in Fig. 4.11(a) than that in Fig. 4.11(b). The defects which were described in later text corresponded to the sintering pores. TiO_2 was not indicated in SEM images, because the size of TiO_2 was of several hundred nanometers, which was difficult to be observed in the SEM images. Thereafter, the area fractions of TiB_2 in both compacts were predicted to be 29.3% for 1323 K and 31.4% for 1373 K by image analysis, almost the same amount with initial TiB_2 addition. This result indicated that TiB_2 was barely decomposed after sintering. And thus, Fe-5Ti alloyed powders are an effective matrix for the purpose of preventing the TiB_2 from decomposing and the fabrication of Fe_2B free Fe/TiB_2 composites by PM is feasible.

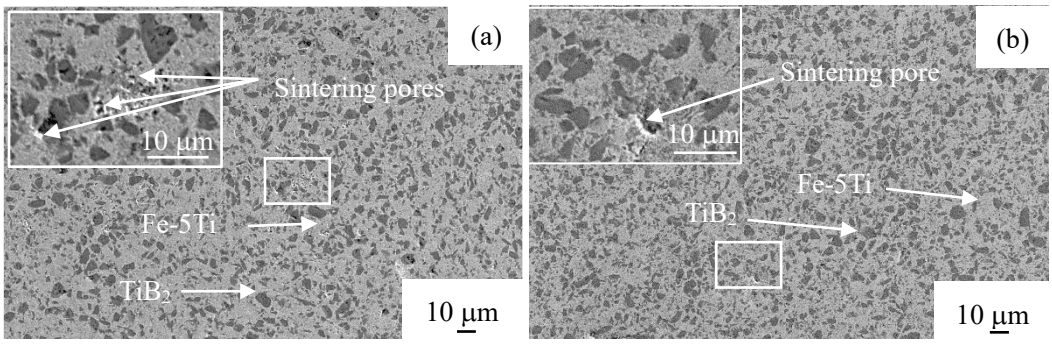

Fig. 4.11 SEM images of (Fe-5Ti)-30vol.%TiB_2 compacts sintered at (a) 1323 and (b) 1373 K for 0.6 ks; pores are indicated in the upper-left insets corresponding to the marked areas by white boxes in (a)(b).

Elemental mapping analysis of Fe, Ti and B elements in (Fe-5Ti)-30vol.%TiB_2 sintered compacts are displayed in Figs. 4.12 and 4.13. The Ti and B distributed in highly overlapping regions which were right corresponding to the TiB_2 areas as illustrated in Fig. 4.12 and the same situation was observed in Fig. 4.13, suggesting that

TiB_2 particles were barely decomposed and well preserved after sintering at 1323 and 1373 K for 0.6 ks, which was consistent with the results from XRD patterns. The color change from the center to edge via TiB_2 phase might be caused by the insufficient spatial resolution of WDS, although the phase had homogeneous concentration of Ti and B. Inhomogeneity of the Fe and Ti distribution in Fe-5Ti matrix in Figs. 4.12 and 4.13 was caused by MA process. Because one of the noticeable features of MA process is that as-alloyed powders are macroscopically uniform but microscopically uneven.

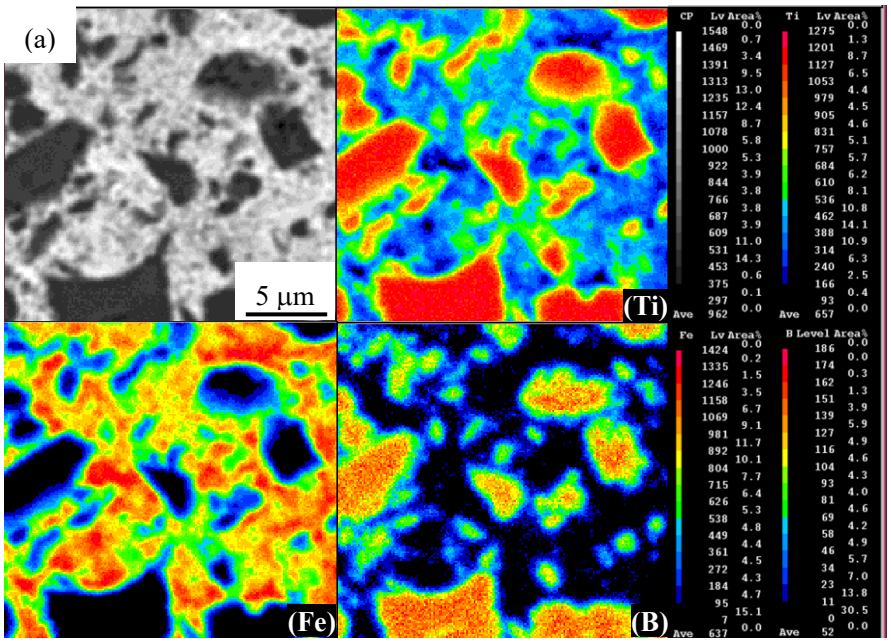

Fig. 4.12 Elemental mapping analysis of Fe, Ti and B elements in (Fe-5Ti)-30vol.%TiB_2 compacts sintered at 1323 K for 0.6 ks: (a) BSE image of the compact, (b), (c) and (d) are the element distribution of Ti, Fe, and B, respectively.

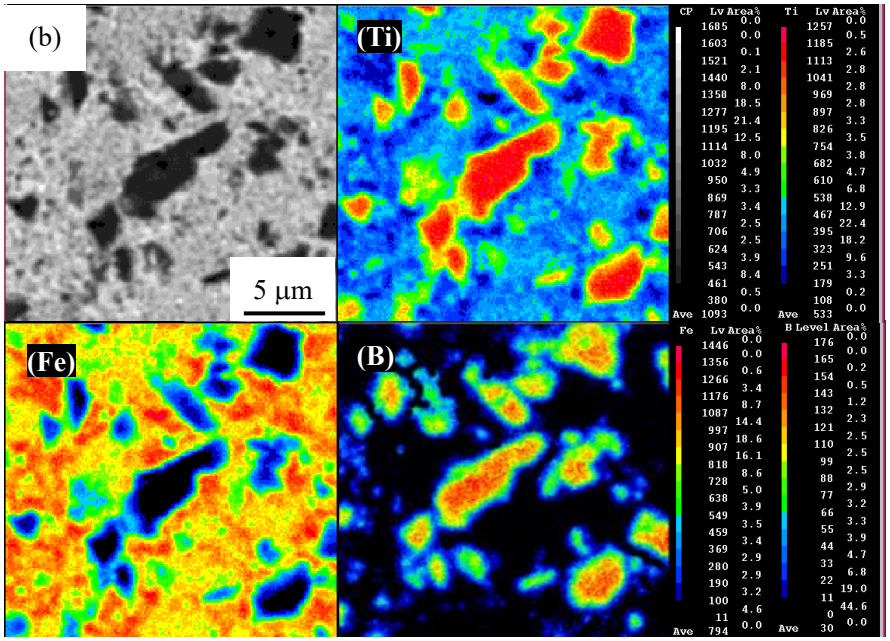

Fig. 4.13 Elemental mapping analysis of Fe, Ti and B elements in (Fe-5Ti)-30vol.%TiB_2 compacts sintered at 1373 K for 0.6 ks: (a) BSE image of the compact and (b), (c) and (d) are the element distribution of Ti, Fe, and B, respectively.

TEM observations of Fe/TiB_2 interface cohesion of compacts sintered at 1323 and 1373 K for 0.6 ks are demonstrated in Fig. 4.14. The compact sintered at 1373 K for 0.6 ks showed better interface cohesion as marked by dashed white arrows in Fig. 4.14(b), in contrast, the compact sintered at 1323 K for 0.6 ks showed the insufficient interface cohesion as indicated by solid white arrow in Fig. 4.14(a) accompanying a few defects. This might be ascribed to that higher temperature can enhance the interface bonding of (Fe-5Ti)/TiB_2. There were no reaction layers between the interface of Fe-5Ti and TiB_2, which was in line with the result that TiB_2 was barely decomposed as seen in Figs. 4.12 and 4.13. Apparently, these TEM images are not enough to interpret the interface bonding condition between TiB_2 and Fe-5Ti. However, it is believed that the interface between TiB_2 and Fe-5Ti will enhance with the increase of sintering temperature. Therefore, for a better and further understanding of the interface bonding conditions at different sintering temperatures, fracture modes in compression tests and crack propagations in hardness tests from the macroscopic perspective were discussed in the following text.

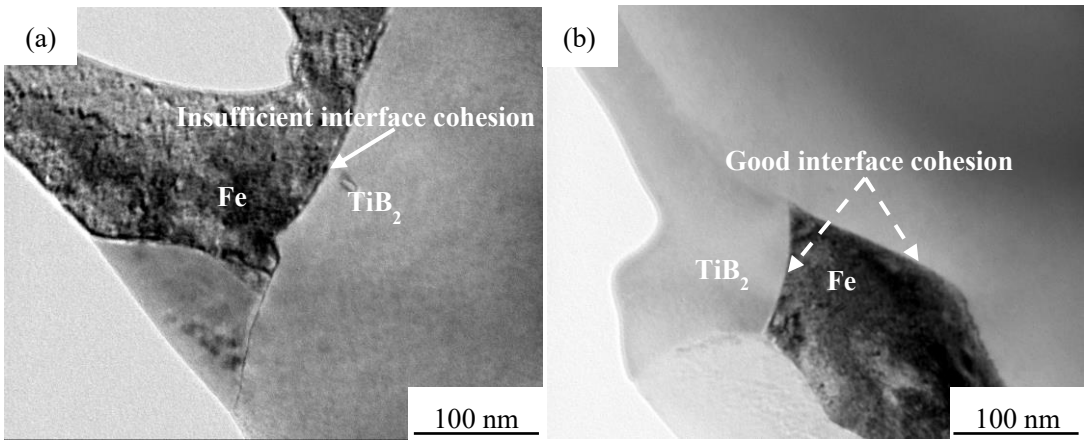

Fig. 4.14 TEM images of (Fe-5Ti)-30vol.%TiB_2 compacts sintered at (a) 1323 and (b) 1373 K for 0.6 ks.

4.3.2.5 TC and hardness of (Fe-5Ti)-30vol.%TiB_2 compacts

As shown in Fig. 4.15, the TC and Vickers hardness of compacts sintered at 1323 and 1373 K for 0.6 ks were 48.0 W/(m·K), 684.7 HV and 53.5 W/(m·K), 716.2 HV, respectively. With the increase of sintering temperature, both TC and Vickers hardness were improved owing to the lower porosity as shown in Fig. 4.15 and enhanced interface bonding between Fe-5Ti/TiB_2 and less sintering pores in the compact sintered at 1373 K as shown in Fig. 4.14(b). Defects[51] and interface thermal resistance[52] are two predominant factors which influence TC of composites, as they can scatter electron or phonon during heat transfer and then decrease the mean free length of the path of electron or phonon, leading to the decrease of thermal conductivity. In this case, in addition to lattice distortion and interface thermal resistance, TiO_2, confirmed by XRD in Fig. 4.10, was another unfavorable factor decreasing the thermal conductivity, on account of the low TC of TiO_2 itself and the increase of heterophase interface. The TC of Fe and Ti were measured to be 80.0 and 24.5 and that of TiB_2 was reported to be about 100.0 W/(m·K)[53]. Therefore, the theoretical TC of fully-dense (Fe-5Ti)-30vol.%TiB_2 was estimated to be 84.0 W/(m·K), based on the rule of mixtures. Apparently, the TC of both sintered compacts was lower than the theoretical value. This could be attributed to the defects such as pores and lattice distortion in the sintered compacts and the formation of TiO_2 with low TC as explained above. In addition to that, interface thermal resistance was not taken into consideration in the calculation of

the theoretical value. As consequence, the experimental values of both sintered compacts were inferior to the theoretical value. Nevertheless, a higher TC of (Fe-5Ti)-30vol.%TiB_2 composite can be expected if the TiO_2 is further suppressed in sintered compacts.

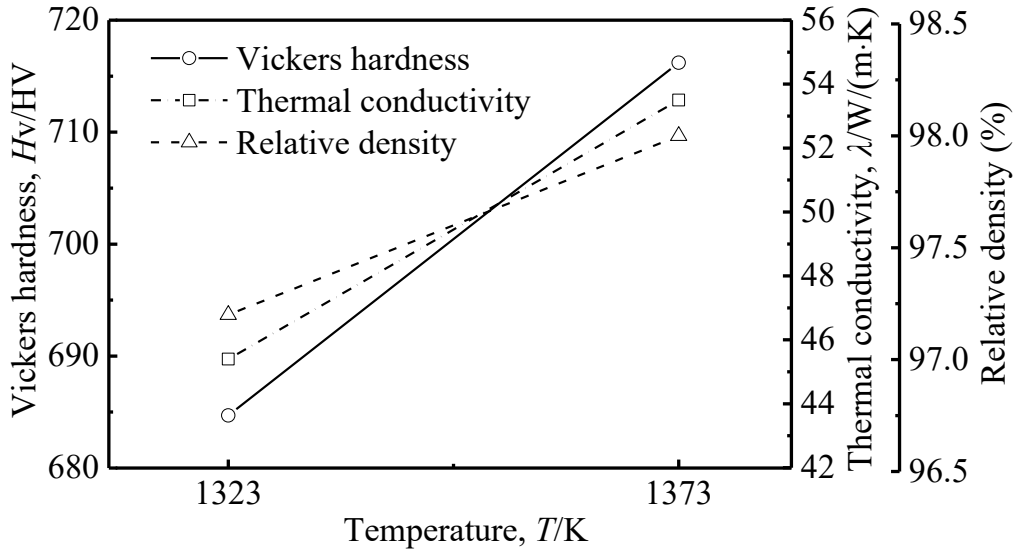

Fig. 4.15 Vickers hardness, TC and relative density of (Fe-5Ti)-30vol.%TiB_2 compacts sintered at 1323 and 1373 K for 0.6 ks.

4.3.2.6 Compression tests of (Fe-5Ti)-30vol.%TiB_2 compacts

Figure 4.16 shows the typical compressive stress-strain curves at room temperature for the sintered (Fe-5Ti)-30vol.%TiB_2 compacts sintered at 1323 and 1373 K for 0.6 ks. The compression strength of the compact sintered at 1373 K was higher than that of the compact sintered at 1323 K, which were 1698 and 2591 MPa, respectively. This was due to the better interface bonding and higher densification at 1373 K as shown in Figs. 4.14 and 4.15. Both compacts were fractured before remarkably plastic deformation. The same fracture mode was also reported in Fe-15Cr-8Al-20Mn/30vol.%TiB_2 composites sintered at 1373 K for 0.6 ks[38]. The fracture modes of two sintered compacts were different, which resulted in the difference of compression strength. As shown in Fig. 4.17(a)(b), the fracture modes were a mixture of TiB_2 cleavage marked by solid red arrows and interface debonding indicated by dashed yellow arrows for both compacts. Whereas, the difference lied in the interface debonding dominated the

fracture behavior in Fig. 4.17(a), on the contrary, TiB_2 cleavage governed the fracture behavior in Fig. 4.17(b). Under the external stress, fracture of TiB_2 particles are prone to occur before particles/matrices debonding due to the good interface cohesion between Fe/TiB_2 interface[5,18]. Hence, it could be interpreted that dominance of interface debonding occurrence for the compact sintered at lower temperature was attributed to the insufficient interface bonding. It is reported the existence of TiO_2 can improve the mechanical properties of composites[54,55]. It applies to this study as well. The TiO_2, mainly derived from MA process, partially accounted for the improvement of hardness and compression strength of composites as TiO_2 played as a strengthening hard phase. The hardness values were 3400 HV[53] and 150 HV in TiB_2 and Fe-5Ti phases, respectively. In contrast, the Vickers hardness of TiO_2 is reported to be 1610 HV[56]. Therefore, TiO_2 also affected the mechanical properties. Despite of the positive effect of the TiO_2 on the mechanical properties of composites, it is still an undesirable phase, because added Ti is consumed by the formation of TiO_2 and it is low in thermal conductivity. According to the reference[57], the strengthening mechanism can mainly be ascribed to the following aspects. Firstly, the load transfer from the soft and compliant matrix to the stiff ceramics under an applied external load, contributes to the strengthening of the base material. Secondly, the particles can play a fundamental role in grain size refinement in metal matrices of composites since they could serve as pinning points, impeding grain growth. It was considered that above factors correspond to the strengthening reasons for (Fe-5Ti)-30vol.%TiB_2 composites. Besides, in the case of present work, solution strengthening or Ti atom solid solution into Fe was another reason responsible for strengthening of matrix.

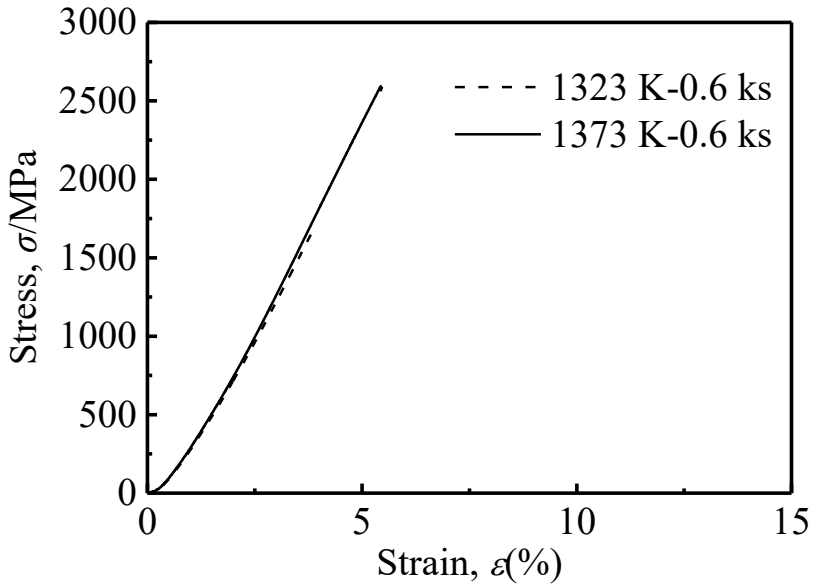

Fig. 4.16 Compressive stress–strain curves of (Fe-5Ti)-30vol.%TiB_2 compacts sintered at 1323 and 1373 K for 0.6 ks.

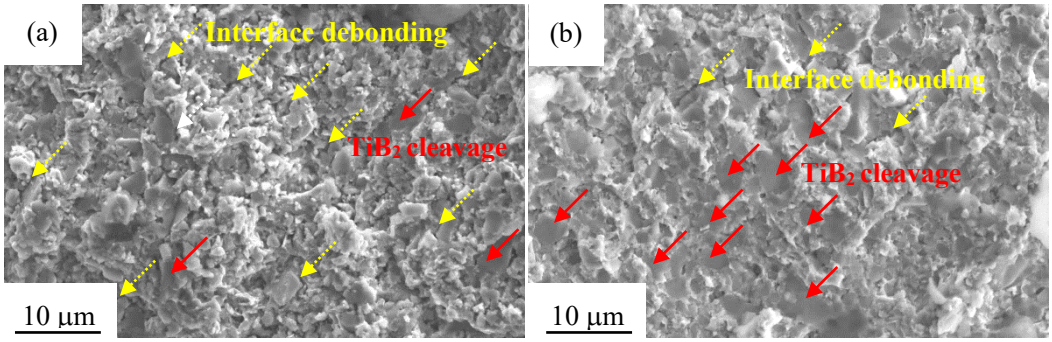

Fig. 4.17 Fracture surface images of (Fe-5Ti)-30vol.%TiB_2 compacts: (a) 1323 K, (b) 1373 K for 0.6 ks; dashed yellow and solid red white arrows refer to interface bonding and TiB_2 cleavage, respectively.

4.3.2.7 Crack propagation of (Fe-5Ti)-30vol.%TiB_2 compacts

There was no crack occurrence in the indented compacts when the applied load was 5 kg. And thus, a load of 30 kg was applied to sintered compacts in order to observe the crack propagations. Fig. 4.18 shows the principal crack propagation images of compacts sintered at different temperatures. The crack mainly propagated along the interface of (Fe-5Ti)/TiB_2 as proved by the interface debonding in Fig. 4.18(a), but it extended primarily through the TiB_2 particles as demonstrated by TiB_2 breakage in Fig.

4.18(b). The result indicated the interface strength of the compact sintered at 1373 K was stronger than that of the compact sintered at 1323 K. Coupled with the result obtained from the fracture modes, the difference in crack propagations in the HV indented compacts confirms that higher sintering temperature guarantees a better (Fe-5Ti)/TiB_2 interface bonding.

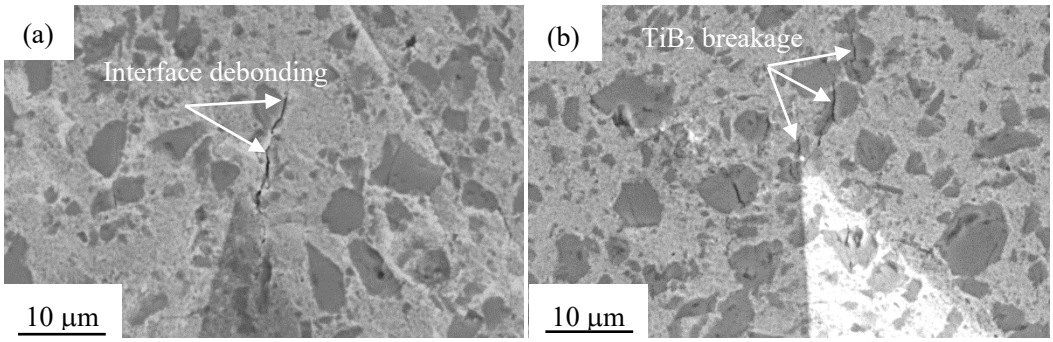

Fig. 4.18 Crack propagation images of (Fe-5Ti)-30vol.%TiB_2 compacts sintered at: (a) 1323 K, (b) 1373 K for 0.6 ks; and interface debonding in (a) and TiB_2 breakage in (b) are marked by white arrows

4.3.2.8 Comparison with SKD61

For comparison, the mechanical and thermal properties of compacts sintered in this work and the alloy from other published literature[58] were listed in Table 4.2. The Vickers hardness and TC of SKD61 quenched and tempered were measured to be 516.0 HV and 24.0 W/(m·K) in this study, respectively. Relatively high TC of 40CrMnMo7 alloy[58] (Fe-0.37C-1.7Cr-1.4Mn-0.21Si-0.16Mo) for high-pressure die casting as one of HWTs was revealed in Table 4.2, but its hardness was not given. Meanwhile, the (Fe-5Ti)-30vol.%TiB_2 compacts sintered in this work exhibited either higher or comparable values in both Vickers hardness and TC compared with other alloys. More specifically, the Vickers hardness and TC of (Fe-5Ti)-30vol.%TiB_2 compact sintered at 1373 K for 0.6 ks were the highest among all listed items. The TC and Vickers hardness of the two compacts sintered at 1323 and 1373 K for 0.6 ks were 2.0, 1.3 and 2.2, 1.4 folds than those of SKD61. And hence, in terms of TC and Vickers hardness, Fe_2B free (Fe-5Ti)-30vol.%TiB_2 composites with improvement of hardness and TC were fabricated

successfully by PM. SKD61 is a martensite matrix with a proper grain size and uniform carbides precipitation distribution in it.[59] A series of heat treatments have to be applied in order to acquire desirable properties, such as annealing, stress relieving, preheat prior to hardening, hardening, quenching and tempering. Those complex processes are not cost effective and energy saving in the pursuit of sustainable society. In contrast, the synthesis of (Fe-5Ti)-30vol.%TiB_2 compacts with improvement of TC and Vickers hardness can be achieved by simplex spark sintering process which leads to cost effective and relative energy saving, compared with those complex manufacturing treatments of SKD61. That is to say, (Fe-5Ti)-30vol.%TiB_2 compacts are very promising in the application of HWTs in the future.

Table 4.2 Vickers hardness and TC of (Fe-5Ti)-30vol.%TiB_2 compacts and other alloys measured at room temperature.

Materials	Vickers hardness (HV)	TC (W/(m·K))	Refs
(Fe-10Ti)/30TiB_2-1323K	686.7	32.7	This study
(Fe-10Ti)/30TiB_2-1373K	727.5	38.2	This study
(Fe-5Ti)/30TiB_2-1323K	684.7	48.0	This study
(Fe-5Ti)/30TiB_2-1373K	717.5	53.5	This study
SKD61	516.0	24.0	This study
40CrMnMo7	--	45.0	55)

According to the data published in Iron and Steel Division, Manufacturing Industries Bureau of Japan in 2018, the production of hot work tool steels was 3323 t and the heat treatments cost was 0.615 billion JPY per ton. Therefore, the corresponding total cost for heat treatments was 2043.645 million JPY. In the case of Fe-30vol%TiB_2 composites, electricity was the only energy consumption. The electricity consumption (W) for the synthesis of 1 kg composites could be calculated based on the equation (1).[61]

$$W=50\times(1500A\times4V\times1h)/1000 \quad (1)$$

The cost (M) for the above could be acquired by equation (2).

$$M=W\times 15 \quad (2)$$

If the Fe-30vol%TiB_2 composites with same amount of 3323 t are produced, the total cost is 14953.5 billion JPY. Consequently, the cost, excluding the casting cost, on SKD61 is about 1/7 of that on Fe-30vol%TiB_2 composites. This is quite reasonable because the former one is in industry scale while the latter one is in laboratory scale. Therefore, cost-down of fabricating Fe-30vol%TiB_2 composites can be expected if it is industrialized.

In addition, the thermal conductivity of Fe-30vol%TiB_2 composites is much higher than that of SKD61. For example, the thermal conductivity of compact sintered at 1373 K for 0.6 ks is about 2.3 folds of that of SKD61 as shown in Fig. 4.19, which means the production proficiency during service can be 1.3 folds faster than of that of SKD61 when they are put into practice. Evidently, laboratory-made Fe-30vol%TiB_2 composites are not energy-saving and environmentally friendly, but they are superior in production proficiency compared to SKD61.

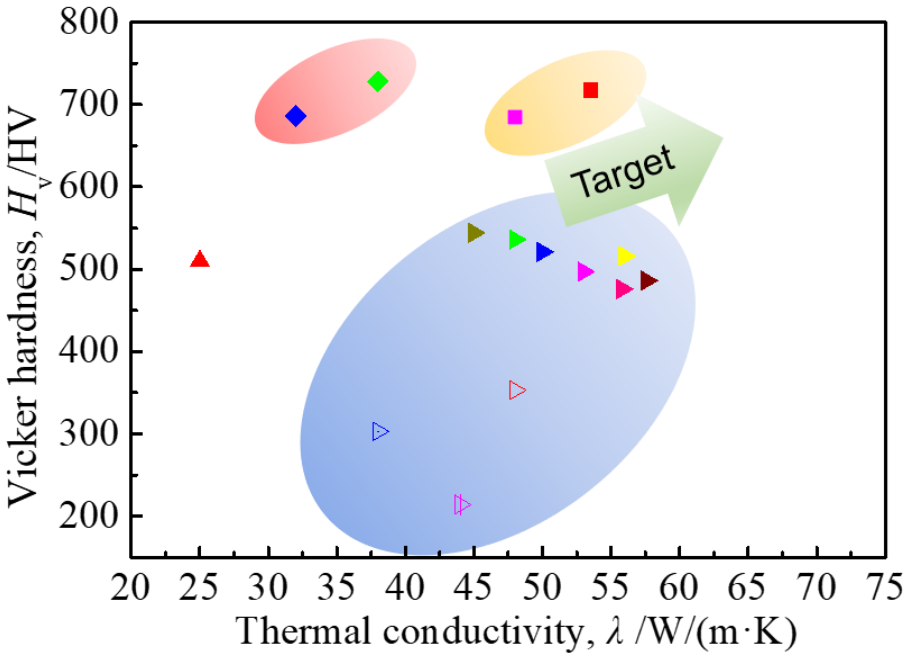

Fig. 4.19 Vickers hardness and thermal conductivity of compacts sintered at different conditions.

4.4 Research prospects

In this study, Fe base-TiB_2 composites for the usage of HS was investigated by PM. The TC and hardness, which are the focus of this study, were measured. In the case of pure Fe-TiB_2 composites, TiB_2 is not chemical stability in pure Fe at high temperature and reactions deepen as the increase of sintering temperature and holding time. But excellent interfacial cohesion of Fe and TiB_2 was characterized in Fe-TiB_2 composites fabricated by PM. As mentioned above, the service temperature of HS is close austinite transformation temperature which will cause changes in phase kinds and amount (microstructure instability) in pure Fe-TiB_2 composites, leading to disqualification in reproducibility and accuracy during HS process. Thus, in order to acquire composites with stable microstructures, Fe-Ti alloy was designed to replace the pure Fe. Results show that the decomposition of TiB_2 is suppressed by using Fe-5Ti and Fe-10Ti matrix, and more importantly, the microstructure stability is achieved. There are two purposes for Fe-Ti alloy. On the one hand, to suppress the decomposition of TiB_2, on the other hand, to expand the α-Fe area, as BCC structured Fe can be maintained even over the phase transformation temperature of α Fe-γ Fe if some Ti solid solute in Fe. (Fe-5Ti)-30vol.%TiB_2 compact sintered at 1373 K for 0.6 ks not only shows the improved TC and hardness, but also qualifies in microstructure instability at over service temperature.

However, (Fe-5Ti)-30vol.%TiB_2 composites is far from being perfect, since there are still some places which can be improved. First, the Ti addition can be reduced to 3at.% if there are less C diffusing into the compact. Less Ti addition in Fe means higher TC of matrix. Second, Fe-Ti alloy powders were fabricated by MA where some impurities which can contaminate the powders and final compacts were inevitably introduced. The higher TC can be expected if there less impurities involved. In order to deal with the impurities, Fe-Ti alloy fabricated by atomization method will be recommended. Last, as for the sintering parameters, the sintering temperature can be increased, since the eutectic reaction of Fe-3at.% Ti and TiB_2 is 1593 K.[33)] In addition, the holding time can be also extended. The TC of Fe base-TiB_2 composites could be further improved if the above measures are taken in consideration.

4.5 Summary

Monophasic BCC structured Fe-10Ti alloy powder had been successfully fabricated by MA and was used as the matrix for a substitution for pure iron. No Fe_2B phase was found in both compacts sintered at 1323 and 1373 K for 0.6 ks, proving TiB_2 was barely decomposed during the sintering process, and thus, thermal and chemical stability of TiB_2 in Fe are achieved. The TC and Vickers hardness of compacts sintered at 1323, 1373 K for 0.6 ks were 32.7 W/(m·K), 686.7 HV and 38.2 W/(m·K), 727.5 HV, respectively, which were 1.36, 1.33 and 1.59, 1.41 folds t of SKD61. Compact sintered at higher temperature showed higher mechanically properties and better TC due to the improved densification and interfacial bonding between Fe/TiB_2.

Monophase BCC structured Fe-5Ti alloy powders had been successfully fabricated by MA and were used as the matrix for a substitution for pure Fe. Their compacts consisted of α-Fe and TiB_2 with almost 30vol.%, which meant no-decomposition of TiB_2. Their results agreed with the achievement of thermal stability of TiB_2 in Fe-5Ti during spark sintering synthesis, which might be possibly interpreted that the introduction of Ti into Fe balanced the chemical potential of Ti atom in both sides of TiB_2 and Fe-5Ti alloy. The TC and Vickers hardness of compacts sintered at 1323 and1373 K for 0.6 ks were 48.0 W/(m·K), 684.7 HV and 53.5 W/(m·K), 717.5 HV, respectively, which were 2.0, 1.3 and 2.2, 1.4 folds of SKD61. Besides, the compression strength of two compacts at 1323 and 1373 K were measured to be 1698 and 2591 MPa, respectively. The compact sintered at higher temperature showed better mechanical properties and higher TC due to the improvement of densification, interface bonding between (Fe-5Ti)/TiB_2 and less defects. This work provides a new method for fabricating Fe_2B free Fe-TiB_2 composites by PM with both improvement of TC and hardness.

References

1) C. Baron, H. Springer and D. Raabe: Mater. Des. 111 (2016) 185-191.
2) R. Aparicio-Fernández, H. Springer, A. Szczepaniak, H. Zhang and D. Raabe: Acta Mater. 107 (2016) 38-48.
3) A. Szczepaniak, H. Springer, R. Aparicio-Fernández, C. Baron and D. Raabe: Mater. Des. 124 (2017) 183-193.
4) L. He, Y. Liu, J. Li and B.H. Li: Mater. Des. 36 (2012) 88-93.
5) M. Dammak, M. Gaspérini and D. Barbier: Mater. Sci. Eng. A 616 (2014) 123-131.
6) H. Springer, C. Baron, A. Szczepaniak, V. Uhlenwinkel and D. Raabe: Sci. Rep. 7 (1) (2017) 2757.
7) H. Zhang, H. Springer and R. Aparicio-Fernández: Acta Mater. 118 (2016) 187-195.
8) P. Villars, A. Prince and H. Okamoto: ASM International 5 (1995) 5644-5645.
9) A.K. Shurin and N.A. Razumova: Sov. Powder Metall. Met. Ceram. 18 (12) (1979) 903–905.
10) S.S. Ordan'yan, B.Y. Yuriditskii and I.B. Panteleev: Sov. Powder. Metall. Met. Ceram. 21 (7) (1982) 595–597.
11) L.M. Cha, S. Lartigue-Korinek, M. Walls and L. Mazerolles: Acta Mater. 60 (2012) 6382–6389.
12) A.D. Panasyuk and A.P. Umansky: J. Less Common Metals 117 (1-2) (1986) 335-339.
13) A. Passerone, M.L. Muolo and D. Passerone: J. Mater. Sci. 41 (16) (2006) 5088-5098.
14) D.H. Bacon, L. Edwards, J.E. Moffatt and M.E. Fitzpatrick: Int. J. Fatigue 48 (3) (2013) 39-47.
15) Y.Z. Li and M.X. Huang: Characterization of Minerals, Metals, and Materials (2017) 453-460.
16) S. Lartigue-Korinek, M. Walls, N. Haneche, L.M. Cha, L. Mazerolles and F. Bonnet: Acta Mater. 98 (2015) 297-305.

17) D.H. Bacon, L. Edwards, J.E. Moffatt and M.E. Fitzpatrick: Acta Mater. 59 (9) (2011) 3373-3383.
18) Z. Hadjem-Hamouche, J.P. Chevalier, Y.T. Cui and F. Bonnet: Steel. Res. Int. 83 (6) (2012) 538-545.
19) C. Baron, H. Springer and D. Raabe: Mater. Sci. Eng. A 724 (2018) 142-147.
20) C. Baron, H. Springer and D. Raabe: Mater. Des. 97 (2016) 357-363.
21) H. Springer, R.A. Fernandez, M.J. Duarte, A. Kostka and D. Raabe: Acta Mater. 96 (2015) 47-56.
22) M.X. Huang, B.B. He, X. Wang and H.L. Yi: Scr. Mater. 99 (2015) 13-16.
23) F. Bonnet, V. Daeschler and G. Petitgand: Can. Metall. Q. 53 (3) (2014) 243-252.
24) C.C. Degnan and P.H. Shipway: Metall. Mater. Trans. A 33 (9) (2002) 2973-2983.
25) S.C. Tjong and K.C. Lau: Mater. Lett. 41 (4) (1999) 153-158.
26) A. Anal, T.K. Bandyopadhyay and K. Das: J. Mater. Process. Technol. 172 (2006) 70–76.
27) Y. Wang, Z.Q. Zhang, H.Y. Wang, B.X. Ma and Q.C. Jiang: Mater. Sci. Eng. A 422 (1-2) (2006) 339-345.
28) M. Ziemnicka-Sylwester, L. Gai and S. Miura: Mater. Des. 69 (2015) 1-11.
29) C.C. Degnan and P.H. Shipway: Wear 252 (9-10) (2002) 832-841.
30) L. Gai and M. Ziemnicka-Sylwester: Int. J. Refract Met. Hard Mater. 45 (2014) 141-146.
31) S.H. Yeh, L.H. Chiu, T.L. Chuang and C.Y. Wu: Mater. Trans. (2013): M2013019.
32) L.H. Chiu, C.H. Wu and H. Chang: Wear 253 (7-8) (2002) 778-786.
33) L. Ottavi, J.M. Chaix, C.H. Allibert and H. Pastor: Solid State Phenom. 25-26 (1992) 543-550.
34) A. Antoni-Zdziobek, M. Gospodinova, F. Bonnet and F. Hodaj: J. Phase. Equlib. Diff. 35 (6) (2014) 701-710.
35) P.S. Gilman and J.S. Benjamin: Ann. Rev. Mater. Sci. 13 (1983) 279-300.
36) C. Suryanarayana, E. Ivanov and V.V. Boldyrev: Mater. Sci. Eng. A 304 (2001) 151-158.

37) M.G. Barandika, J.M. Sanchez, T. Rojo, R. Cortes and F. Castro: Scr. Mater. 39 (10) (1998) 1395-1400.

38) J. Liu, W.P. Chen, L. Chen, Z.B. Xia, H.Q. Xiao and Z.Q. Fu: J. Alloy. Compd. 747 (2018) 886-894.

39) W. Ji, J.Y. Zhang, W.M. Wang, H. Wang, F. Zhang, Y.C. Wang and Z.Y. Fu: J. Eur. Ceram. Soc. 35 (3) (2015) 879-886.

40) Z.Z. Fu and R. Koc: Mater. Sci. Eng. A 702 (2017) 184-188.

41) Z. Fu and R. Koc: J. Am. Ceram. Soc. 100 (7) (2017) 2803–2813.

42) Z. Fu and R. Koc: Mater. Sci. Eng. A 735 (2018) 302-309.

43) Y.L. Li, H.Y. Xu, B. Ke, Y.C. Sun, K. Yang, W. Ji, W.M. Wang and Z.Y. Fu: Ceram. Int. (2018).

44) K. Matsugi: J. Kor. Powd. Met. Inst. 19 (2012) (2) 127-133.

45) K. Matsugi, K. Tomigahara, Z.F. Xu, Y.B. Choi and G. Sasaki: J. Jpn. Soc. Powder Metallurgy 59 (2012) (9) 525-531.

46) G.Q. Xie, O. Ohashi, T. Yoshioka, M.H. Song, K. Mitsuishi, H. Yasuda, K. Furuya and T. Noda: Mater. Trans. 42 (9) (2001) 1846-1849.

47) Z.F. Xu, Y.B. Choi, K. Matsugi, D.C. Li and G. Sasaki: Mater. Trans. 51 (3) (2010) 510-515.

48) K. Matsugi, H. Kuramoto, T. Hatayama and O. Yanagisawa: J. Mater. Process. Technol. 134 (2) (2003) 225-232.

49) S.M. Kang, Z.F. Xu, Y.B. Choi, K. Fujita, K. Matsugi and J.K. Yu: Mater. Trans. 57 (5) (2016) 600-607.

50) J.L. Murray: ASM International (1987) 99–111.

51) S. Raghavan, H. Wang, R.B. Dinwiddie, W.D. Porter and M.J. Mayo: Scr. Mater. 39 (8) (1998) 1119-1125.

52) C.W. Nan, R. Birringer, D.R. Clarke and H. Gleiter: J. Appl. Phys. 81 (10) (1997) 6692-6699.

53) R. Telle, L.S. Sigl and K. Takagi: Boride-Based Hard Materials, Handbook of Ceramic Hard Materials. 2000.

54) H.A. Al-Turaif: Prog. Org. Coat. 69 (3) (2010) 241-246.

55) J.F. Li, Z.L. Xu, H. Yang, L.Y. Yu and M. Liu: Appl. Surf. Sci. 255 (9) (2009) 4725-4732.

56) D. Wojcieszak, M. Mazur, J. Indyka, A. Jurkowska, M. Kalisz, P. Domanowski, D. Kaczmarek and J. Domaradzki: Materials Science-Poland 33 (3) (2015) 660-668.

57) R. Casati and M. Vedani: Metals 4 (1) (2014) 65-83.

58) J. Wilzer, J. Küpferle, S. Weber and W. Theisen: J. Mater. Sci. 49 (14) (2014) 4833-4843.

59) Y. Meng, S. Sugiyama and J. Yanagimoto: J. Mater. Process. Tech. 212 (8) (2012) 1731-1741.

Chapter 5

Conclusions

In this research, Fe base-TiB_2 composites for the usage of Hot Stamping material were studied, achieving good hardness and thermal conductivity against SKD61. The conclusions were drawn as follows.

1) Multimodal balls and Combination of wet/dry mixing could both improve spatial distribution of TiB_2 in Fe matrix. In this study, reducing L balls and increasing M and S balls moderately improved spatial distribution of TiB_2 in Fe matrix. However, over-reducing L balls deteriorated mixing effect. Therefore, multimodal balls have to be maintained at a balanced weight ratio in mixing to obtain a better spatial distribution of TiB_2 in Fe matrix. Rotational speed of planetary ball mixing has an optimum value for Fe-TiB_2 composites. Over rotational speed deteriorated the spatial distribution and caused undesirable wear of mill, involving debris into powder mixtures.

2) Sintering temperature and holding time show an optimum point for hardness and thermal conductivity of Fe-TiB_2 composites because of trade-off between the densification and growing number of reacted phases. Increasing temperature and holding time improved relative density, hardness and interface bonding, but accelerated reaction between Fe and TiB_2 particles, which created undesirable phases of Fe_2B and TiC in compacts. And hence, thermal conductivity was compromised.

4) Fe is not chemically stable in pure Fe in high temperature. On the purpose of suppressing the decomposition of TiB_2 and formation of Fe_2B, the new matrix of Fe-xTi (x=5, 10) alloys were designed, and successfully fabricated by mechanical alloying. The (Fe-xTi)-TiB_2 composites suggested excellent hardness and thermal conductively trade-off. Meanwhile, the decomposition of TiB_2 and formation of Fe_2B were suppressed in (Fe-xTi)-TiB_2 composites.

5) Finally, the thermal conductivity and Vickers hardness (Fe-5Ti)-30vol.%TiB_2 compact sintered at 1373K for 0.6 ks were 53.5 W/(m·K), 717.5 HV, respectively,

which were 2.2 and 1.4 folds of that of SKD61.

.

Acknowledgements

First and foremost, I would like to pronounce my utmost degree of gratitude to my supervisor, Professor Kazuhiro Matsugi, for his selfless dedication to instructing and helping me not only on my research but also on my life and career. His constructive advice, rigorous working attitude, open mind and great inclusiveness always influence and orientate me when I run into intractable things.

Secondly, I would like to express my sincere acknowledgement to Assistant Professor Yongbum Choi and (Former) Assistant Professor Zhefeng Xu, who give me tremendous help on my experiments and life. The suggestion and help from Professor Keiji Yamada, associate Professor Kenjiro Sugio and Mister Hajime Suetsugu are also highly appreciated. And I also present my gratitude to Professor Wang and Professor Yu for their unconditional assistance when I carried out some experiments at Yanshan University. Besides, I am thankful to Doctor Kang and Doctor Yu who guided me a lot especially on experiments and equipment operation when I first came to Japan. In addition, I express great attitude to Mister Xilong Ma, Mister Zeze Xiao, Mister Xuan Meng, Mister Fei Gao, Mister Yan Zhan and all the labmates in Properties Control.

Thirdly, I gratefully acknowledge the support from LETS Research Group, Incubation Research Center of Hiroshima University, Y-TEC Corporation, KEYLEX Corporation, MAZDA and HATACHI METALS, Ltd.

Lastly, I am greatly indebted to my parents and elder brother who support me no matter where I am and what I am. And my great appreciation to my girlfriend who is always by my side and back up me.

Published papers in regard to this thesis

1. **Y.J. Ke**, K. Matsugi*, Z.F Xu*, Y.B. Choi, M.Z. Wang and J.K. Yu. Spark Sintering of TiB_2 Reinforced Fe Matrix Composites with Both High Thermal Conductivity and Hardness, and their Microstructural Characterizations. Materials Transactions. 2020 (61) 3: in press. (Chapter 3)

2. **Y.J. Ke**, K. Matsugi*, Z.F Xu*, Y. He, Y.B. Choi, M.Z. Wang and J.K. Yu. Synthesis of 30 vol%TiB_2 Containing Fe-5Ti Matrix Composites with High Thermal Conductivity and Hardness. Materials Transactions. 2019 (60) 12: 2516-2524. (Chapter 4)

3. **Y.J. Ke**, K. Matsugi*, Y.B. Choi. Both Effects of Powder Mixing and Spark Sintering for 30vol.%TiB_2 Strengthened Steels with Ti Macro-Alloying MMCs. The 12th Korea-Japan Joint Symposium on Composite Materials. 2019. (Chapter 2)

4. **Y.J. Ke**, K. Matsugi*, Z.F Xu, Y. He, Y.B. Choi, M.Z. Wang and J.K. Yu. Fabrication of (Fe-10Ti)-TiB_2 Composites with Both high Thermal Conductivity and Hardness by SPS. The Tenth Pacific Rim International Conference on Advanced Materials and Processing (PRICM10). 2019: 1015-1022. (Chapter 4)

5. **Y.J. Ke**, K. Matsugi*, Z.F Xu, Y.B. Choi, M.Z. Wang and J.K. Yu. Fabrication of Fe-TiB_2 Composites and their Properties. 2018 World Congress on Powder Metallurgy. 2018: 367-372 (Chapter 3)

Presentations

1. **Y.J. Ke**, K. Matsugi*, Y.B. Choi. Both Effects of Powder Mixing and Spark Sintering for 30vol.%TiB_2 Strengthened Steels with Ti Macro-Alloying MMCs. The 12th Korea-Japan Joint Symposium on Composite Materials. December 5-7, 2019, Changwon, Korea, Changwon Exhibition Convention Center.

2. **Y.J. Ke**, K. Matsugi*, Z.F Xu, Y.B. Choi, M.Z. Wang and J.K. Yu. Fabrication of Fe-TiB_2 Composites and their Properties. 2019 annual fall (165th) meeting of JIM September 11-13, 2019, Okayama, Japan, Okayama University, Tsushima Campus.

3. **Y.J. Ke**, K. Matsugi*, Z.F Xu, Y. He, Y.B. Choi, M.Z. Wang and J.K. Yu. Fabrication of (Fe-10Ti)-TiB_2 Composites with Both High Thermal Conductivity and Hardness by SPS. The Tenth Pacific Rim International Conference on Advanced Materials and Processing (PRICM10). August 18-22, 2019, Xian, China, Qujiang International Conference Center.

4. **柯雨蛟**、松木一弘、許哲峰、崔龍範。電焼結による難焼結材料の作製。広島大学若手研究者による研究シーズ発表会。平成 31 年 3 月 11 日(月)、広島県、広島市、ホテル広島ガーデンパレス。

5. **Y.J. Ke**, K. Matsugi*, Z.F Xu, Y.B. Choi, M.Z. Wang and J.K. Yu. Fabrication of Fe-TiB_2 Composites and their Properties. 2018 World Congress on Powder Metallurgy. September 16-20, 2018, Beijing, China, China National Convention Center.

6. **Y.J. Ke**, M.Z. Wang, Q. Zou, H. Tang, Y.C. Zhao, K. Matsugi, Y.B. Choi, Z.F. Xu. Fabrication of Si_3N_4 Matrix Composites with Self-lubricating Ability and their Properties. 日本鉄鋼協会・日本金属学会 中国四国支部 鉄鋼第59回・金属第57回 合同講演大会。 平成29年8月21日(月)、 高知県、 高知工科大学、 永国寺キャンパス。